SCUOLA
NORMALE
SUPERIORE

Classe di Scienze

Corso di perfezionamento in
Nanoscienze

XXXIV ciclo

High Quality Graphene For Sensing And Automotive Applications

Settore Scientifico Disciplinare FIS/03

Candidato
dr. Ayush TYAGI

Relatore

Prof. Camilla COLETTI

Supervisione interna

Prof. Fabio BELTRAM

SCUOLA
NORMALE
SUPERIORE

Anno accademico 2023/2024

SCUOLA NORMALE SUPERIORE

A dissertation presented for the degree of

Doctor of Philosophy

HIGH QUALITY GRAPHENE FOR SENSING AND AUTOMOTIVE APPLICATIONS

by

Ayush Tyagi

Supervisor: Dr. Camilla Coletti

Foreword

The work presented in this thesis is the result of my research activity at NEST laboratory of Scuola Normale Superiore in Pisa. I started working on graphene in 2019 during my PhD at NEST laboratory, focusing on the adoption of high-quality graphene for magnetic sensing, light detection and ultimately automotive applications. The PhD scholarship was sponsored by Tronchetti Provera Foundation and performed with a joint collaboration of Scuola Normale Superiore and Istituto Italiano di Tecnologia.

Abstract

Graphene, a single layer of graphite, is an extremely promising material for a wide range of future applications. It presents remarkable electrical and thermal conductivity, optical transparency, impermeability, and striking tribological properties: it is stronger than steel while retaining a high flexibility. For all these reasons, graphene has recently become a material of interest for automotive applications: an ideal candidate to realize composites with enhanced properties, e.g., improved rubbers for tires, and highly performing sensors.

In this thesis, the adoption of graphene for the realization of devices (i.e., magnetic and visible light sensors) and components (e.g., tires) in automotive industry, is studied. In the first part of the thesis, we demonstrate an approach to transfer highly-crystalline graphene originally grown on Cu foil via chemical vapor deposition (CVD) to a target substrate while maintaining a high level of cleanliness of the material. This is a relevant step which subsequently allows for the realization of high-performance devices and fundamental investigations focusing on interfacing graphene with rubbers. To this end, a specific two-step cleaning approach for obtaining ultra-clean graphene with high mobility and low residual carrier density is demonstrated. Indeed, enhancing the performance of graphene-based devices in terms of carrier density, mobility and stability is a primary factor to be considered before integrating it in different technological applications.

After developing an approach to obtain high quality CVD graphene on target substrates with technological relevance, such as SiO_2/Si, we move towards its inclusion in ambient-stable magnetic-sensing applications. Stable Hall sensors are magnetic sensors which nowadays are extensively used for proximity sensing, accurate positioning, switching, angular sensing, speed detection, and current sensing, thus being of crucial importance in automotive, aeronautics, consumer electronics, Internet of Things (IoT) and robotic applications. Here we demonstrate a facile and scalable approach to realize polymer-encapsulated graphene Hall sensors based on CVD graphene with remarkably high magnetic sensitivity and air stability. These magnetic probes are promising alternatives to current semiconductor-based Hall sensing technology.

In the following part of the thesis, we focus on the realization of graphene-based photodetectors. Graphene offers interesting properties for light sensing applications, especially for visible light detection. We demonstrated an easy, stable and scalable approach to create PMMA capped graphene based pn-junctions, which can be employed as photodetectors and in particular as visible light sensors. These graphene based pn-junctions work on the principle of photovoltaic effect where the photogenerated carriers are collected from graphene by using source-drain contacts. The fabricated pn-junction in graphene provides slow recombination of charge carriers due to the built-in potential at the junction. These pn-junction based photodetectors exhibit a responsivity of around 18 μA/W, a response time of approximately 200 ms when subjected to illumination with a 532 nm wavelength, and are expected to have improved stability over time, indicating electron-beam irradiation as an interesting technique for the large-scale fabrication of p-n junction graphene photodetectors.

Finally, the last part of the thesis focuses on investigating the interface between graphene and rubbers. Indeed, besides using graphene in sensing applications, its derivatives i.e., graphene inks, could also be adopted for developing tires in automotive industry. It is expected that the overall performance of tires including heat dissipation, conductivity, grip, wear and weight reduction, could be improved by including graphene in rubber blends. However, preliminary tests evidenced a limited electrical conductivity in graphene-enhanced tires, probably due to limitations in the dispersion of graphene-based material in rubber blends. This issue calls for the development of graphene functionalization techniques to ensure acceptable electrical discharge properties in graphene-enhanced tires. For this purpose, we have investigated the impact of rubber on CVD graphene electrical properties. Furthermore, both CVD graphene and graphene ink functionalization with eco-friendly molecules such as pyrroles and tetrazoles is investigated. By thoroughly characterizing the electrical properties of graphene interfaced with rubbers and by exploring functionalization paths to improve the electrical conductivity in graphene-enhanced rubbers blends, this study provides relevant information for the adoption of graphene in tires.

Contents

List of Abbreviation

1SC	One step cleaning
2D	Two-dimensional
2SC	Two step cleaning
AFM	Atomic force microscopy
Ar	Argon
Au	Gold
BSE	Back scattered electrons
C	Carbon
CNP	Charge neutrality point
Cr	Chromium
CSAR	Chemical Semi Amplified Resist
Cu	Copper
CVD	Chemical vapor deposition
DMA	N, N-Dimethylacetamide
DMEU	1,3-dimethyl-2-imidazolidinone
DMF	Dimethylformamide
DOS	Density of states
EBL	Electron beam lithography
FET	Field effect transistor
FF	Full fabrication
FWHM	Full width at half maximum
GBL	g-butyrolactone
GFET	Graphene field effect transistor
HB	Hall bar
hBN	Hexagonal boron nitride

NeocisBR	Cis polybutadiene
NMP	N-mthylpyrrolidine
IPA	Isopropanol
PDMS	Polydimethylsiloxane
PMMA	Polymethyl methacrylate
PPC	Polypropylene carbonate
Pt	Platinum
PVA	Polyvinyl alcohol
RIE	Reactive ion etching
RMS	Root mean square
SAXPS	Small area x-ray photoelectron spectroscopy
SE	Secondary electrons
SEM	Scanning electron microscopy
Si	Silicon
SiC	Silicon carbide
SLG	Single layer graphene
SLR	Solution-styrene butadiene
TRT	Thermal release tape
THF	Tetrahydrofuran
TMP	Trimethyl pyrrole
vdW	van der Waals
XPS	X-ray photoelectron spectroscopy

Dedicated to my grandmother and family

"If we knew what it was we were

doing, it would not be called research, would it?"

Albert Einstein

Acknowledgements

It has been a long journey that could not have been possible without the help and support of many people along the way. First, I would like to thank my supervisor, Dr. Camilla Coletti, for her constant guidance and motivation during last four years. Her affluence of knowledge and passion toward science encouraged me to relentlessly pursue my PhD research and supported me whenever I met any obstacle. In addition, she has provided me a boundless research environment to polish my skills and knowledge as a researcher by giving me the access to the iit facilities. Without her wonderful support and patience, I could not have achieved the goal to complete my research and thesis.

Special thanks go to Dr. Vaidotas Mišeikis for his valuable time for training and advising me about the CVD graphene growth, device fabrications and transferring graphene to different substrates. His inventive ideas and problem-solving skills helped me vastly to learn more about how to design and plan my research experiments and analyze the data in a concise way. Additionally, a special thanks goes to Dr. Leonardo Martini for training me about different scientific and technical instruments specifically for electrical and magnetic transport measurements. His friendly nature gave me a chance to have many fruitful technical discussions which helped me to enhance my approach towards dealing with many research problems.

Moreover, I would like to thank many excellent colleagues and research group members I met in these years: Neeraj, Stiven, Ylea, Zewdu, Sergio, Vladislav, Giulia, Domenica at NEST laboratory. It has been a privilege to work with these exceptional minds with many discussions and conversations. Furthermore, I am deeply grateful to our collaborator Dr. Damien Aureau for performing XPS measurements and sharing his expertise with us.

Special thanks to my friends at SNS, Mahdi and Omer and Vikas, Atul, Abhinav, Ujjawal and Vishul back in India and all those whose names do not appear here, for helping me either directly or indirectly in all even and odd times.

Finally, I would like to thank my family for their unconditional love, blessings and endless support at every moment in my life. This last word of acknowledgement goes to my girlfriend, Alessia for

her endless love and support. I feel so lucky to have meet someone special and who I can share my ups and downs with.

List of Publications

1. **A. Tyagi**, V. Mišeikis, L. Martini, S. Forti, N. Mishra, Z. M. Gebeyehu, M.A. Giambra, J. Zribi, M. Frégnaux, D. Aureau, M. Romagnoli, F. Beltram, C. Coletti. "Ultra-clean high-mobility graphene on technologically relevant substrates," *Nanoscale*, 2022, 14, 2167 – 2176.

2. **A. Tyagi**, L. Martini, Z. M. Gebeyehu, V. Mišeikis, C. Coletti. "Highly sensitive Hall sensors based on chemical vapour deposition graphene" *ACS Appl. Nano Mater*. 2024, 7, 16, 18329–18336.

3. **A. Tyagi**, L. Martini, Z. M. Gebeyehu, S. Pezzini, V. Mišeikis, A. Rossi, C. Coletti. "Facile Fabrication of lateral graphene PN-junction photodetector," in preparation.

Chapter 1

Introduction

This chapter introduces the two-dimensional (2D) material graphene: its chemical, structural, electrical and magnetic properties. State-of-the-art (SOA) synthetic approaches to obtain high-quality scalable graphene are discussed as well as graphene transfer approaches. Finally, its potential for sensing applications and more specifically for automotive technologies is introduced.

1.1 Overview: Graphene; a two-dimensional material

Two-dimensional materials are thin crystalline sheets with atomic thickness. They can be typically obtained when reducing to one or few layers (<10) layered materials where the composing sheets are vertically held together by van der Waals (vdW) forces.[1,2] The most famous 2D layered material is also the first one that has been demonstrated: graphene. Graphene, a strictly two-dimensional allotrope of carbon, was theoretically introduced by P.R. Wallace in 1947 [3] but physically isolated and studied only 57 years later, in 2004, by Andre Geim and Kostantin Novoselov via mechanical exfoliation of graphite.[4] Within, carbon (C) atoms are disposed in a honeycomb lattice. The 2s, $2p_x$ and $2p_y$ orbitals hybridize to form sp2 planar orbitals that participate in covalent σ bonds. Perpendicular p_z orbitals form delocalized π bonds tha govern the electrical transport in the material.[5] In figure 1.1, the atomic and electronic structure of graphene is depicted.

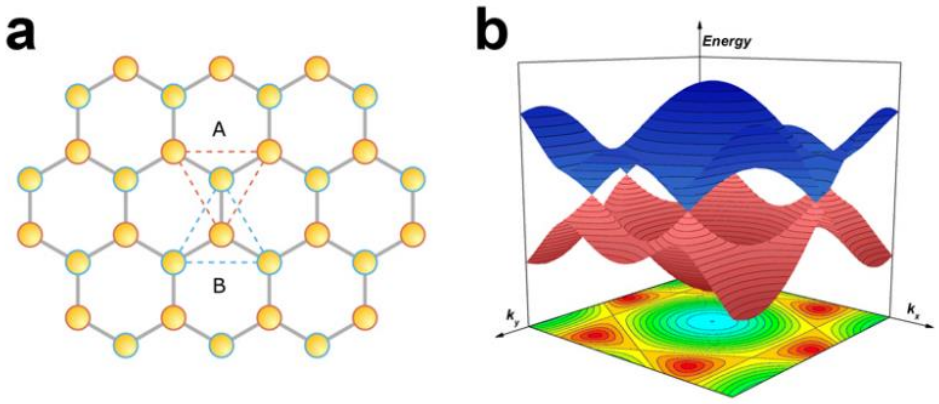

Figure. 1.1 (a) Atomic structure of graphene consisting two triangular sublattices; (b) Three-dimensional band structure in tight binding approximation with π-bands. [6]

The band structure displays a Brillouin zone (BZ) with hexagonal symmetry. Near the K and K' points, the electronic dispersion exhibits what are known as Dirac cones. The electronic wave functions in K and K' points are not equivalent due to distinct pseudospin states stemming from the solution of the Dirac equation for the hexagonal lattice with two carbon atoms in the unit cell. The equation describing graphene band structure near the Fermi energy (E_F) is similar to that of massless Dirac fermions [4]:

$$E(k) = \pm \hbar v_0 |k| \qquad \text{Eq. 1.1}$$

Where $E(k)$ is the energy, $\hbar$ is the reduced Planck constant, v_0 is the Fermi velocity, approximately 10^6 m/s, and k is the wave vector. This accounts for its astonishingly high electron mobility, reaching values as remarkable as 3×10^6 $cm^2\,V^{-1}s^{-1}$ observed experimentally with carrier density of 6×10^{11} cm^{-2} at 1.8 K temperature.[7]. Due to the linear dispersion and the consequent formation of the Dirac cones, the electronic band structure of graphene exhibits a semimetallic character. The Fermi level in graphene coincides with the Dirac point, and at this energy level, the density of states (DoS) is zero, resulting in a semimetal with both electron-like and hole-like carriers. A distinctive feature is the absence of an energy bandgap which renders it unsuitable for devices requiring a high on/off ratio, such as transistors. However, graphene's exceptional electrical characteristics position it as a candidate for future RF analog electronics and magnetic sensing applications[8,9]. Furthermore, the linear dispersion enables broadband absorption within a frequency range of interest for telecom technology, that combined with high mobility allows for the fabrication of high speed modulators.[10][11]. Beyond its electronic merits, graphene's mechanical properties are equally outstanding. With Young's modulus of 1 TPa, graphene is one of the strongest materials on earth[12,13]. Furthermore, graphene exhibits exceptional thermal conductivity, with values approaching 5000 $Wm^{-1}K^{-1}$[14], making it a great candidate to be used in thermal management applications.[15] These multifaceted properties underscore the potential of graphene in revolutionizing diverse fields, from electronics to materials science and beyond. The groundbreaking potential of graphene was recognized in 2010, when the Nobel prize in Physics was assigned to Geim and Novoselov. In the last 19 years, several efforts towards the synthesis and facile and scalable methods to integrate high quality and stable graphene devices in different technologies have been explored.

1.2 Synthesis of graphene

Graphene can be synthesized by using many different techniques which includes mechanical exfoliation,[16] liquid phase exfoliation,[17] epitaxial growth on silicon carbide (SiC),[18] chemical vapor deposition (CVD),[19] and others [20] (see figure 1.2).

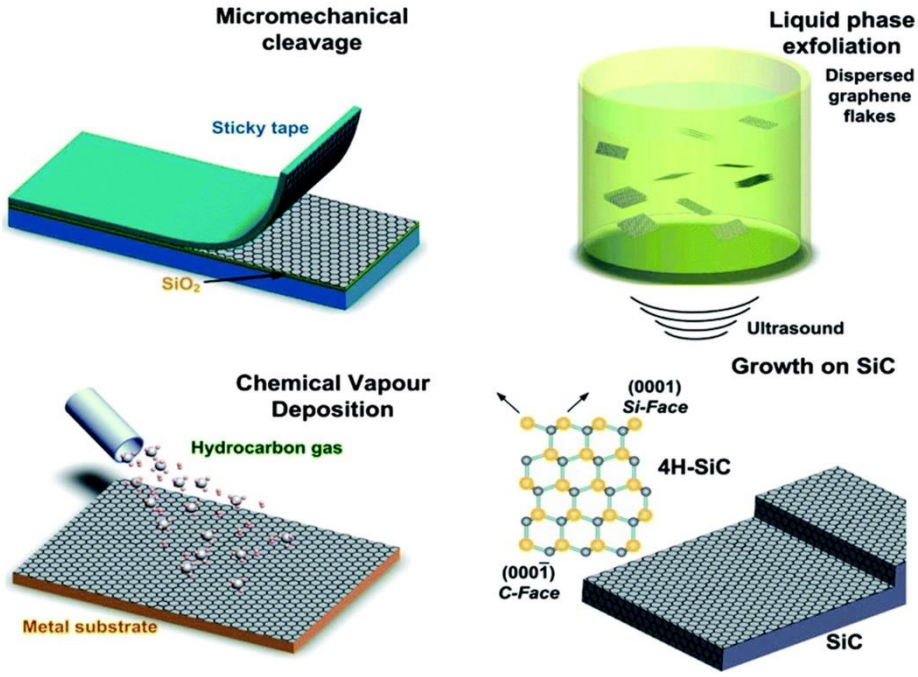

Figure. 1.2 Schematics of most common graphene synthetic techniques.[21]

While comparing all the techniques used for synthesizing graphene, CVD is the one that allows to obtain high crystalline quality graphene over large areas, as it will be discussed below.

1.2.1 Mechanical exfoliation of graphite

Graphene can be obtained from graphite by mechanically applying a force to overcome the van der Waals (vdW) forces between the adjacent layers. In 2004, graphene was mechanically exfoliated by using a scotch tape method leading to the breakthrough research published by Novoselov et al.[4] The micromechanical exfoliation technique is straightforward and can be executed without any need of sophisticated equipment. In this method a piece of adhesive tape is positioned onto the graphite and then repeatedly peeled off until achieving the isolation of atomically thin layers of graphene that are transferred by simply pressing the tape onto another substrate. This process is a promising and popular graphene production technique among the

researchers and for several years has been the only one yielding materials of the highest quality.[22] However, mechanical exfoliation of graphite is a time consuming and operator dependent approach that yields micrometric flakes unsuitable for large-scale production and applications.

1.2.2 Liquid phase exfoliation of graphite

Another common approach for obtaining graphene is liquid phase exfoliation, where ultra-sonication is required for producing graphene from graphite. The key idea behind this approach is to overcome the force between graphite layers in a proper solvent. Typically, this process involves different steps such as graphite dispersion in solvent, exfoliation and purification. Generally, solvents with high surface tension such as (but not limited to) N, N-Dimethylacetamide (DMA), g-butyrolactone (GBL) and 1,3-dimethyl-2-imidazolidinone (DMEU), can be utilized for graphene flakes production.[23] This technique is cost-effective and can easily be scaled up thus yielding high amounts of graphene "inks". However, the control over size and number of layers produced is challenging and by being immersed in a liquid, some of the peculiar properties measured for pristine graphene (such as record carrier mobilities) are significantly altered. This approach is typically adopted to obtain either composite materials (where graphene "inks" are blended with other materials such as for example rubbers to obtain enhanced performance) or coatings.

1.2.3 Thermal decomposition of SiC

An approach to produce scalable highly crystalline graphene is thermal decomposition of SiC. In this technique, SiC substrates are annealed at high temperature either under ultra high vacuum (UHV) conditions or at atmospheric pressure in argon (Ar) environment.[24] At high temperatures (> 1300 °C in UHV), silicon (Si) sublimates and the carbon (C) atoms rearrange in a hexagonal lattice so to form graphene. Graphene can be obtained both on hexagonal [25] and cubic SiC polytypes [26], and on hexagonal ones can be grown either on the Si-face (i.e., SiC(0001)) or on the C-face (i.e., SiC(000-1)). [27,28] On the Si-face is possible to obtain a controlled number of layers (typically from 1 to 3) [29] while on the C-face the surface energetics allow one to obtain several layers of graphene (where layers are typically electronically decoupled). [30] SiC can be purchased either semiconducting or semi-insulating and the grown graphene does not need to be transferred. Most notably, this graphene has been adopted to realize quantum Hall resistance standards. [31]

1.2.4 Chemical vapor deposition (CVD) growth on metals

Among all the graphene growth techniques, CVD graphene growth is the most commonly adopted to obtain scalable crystalline graphene. Typically, cost-effective metallic foils are adopted as substrates as demonstrated in the first work presenting this approach to obtain single layer graphene, published in 2009.[32] In CVD growth of graphene, a carbon based precursor is decomposed with the help of high temperature (and often a catalytic substrate), so that carbon atoms can migrate on the surface and rearrange themselves to form graphene [33]. Carbon precursors can be different, ranging from hydrocarbons,[32] to organic solvents [34] and dry carbon,[35] with methane being the one most commonly adopted. When a metal is used as substrate, the quality and number of graphene layers grown mainly depends on the carbon solubility of the metal. To date, different type of transition metals have been utilized for graphene growth such as Ni[36,37], Cu[32,38], Ru[39], Ir[40], Pt[41], with Cu and Ni being the most adopted thanks to their cost-effectiveness. Graphene growth on Cu offers advantages over Ni, due to the lower solubility of carbon in Cu, which allows to avoid carbon segregation during the cooling down of the metal and thus to obtain single layer growth of graphene.[42,43]

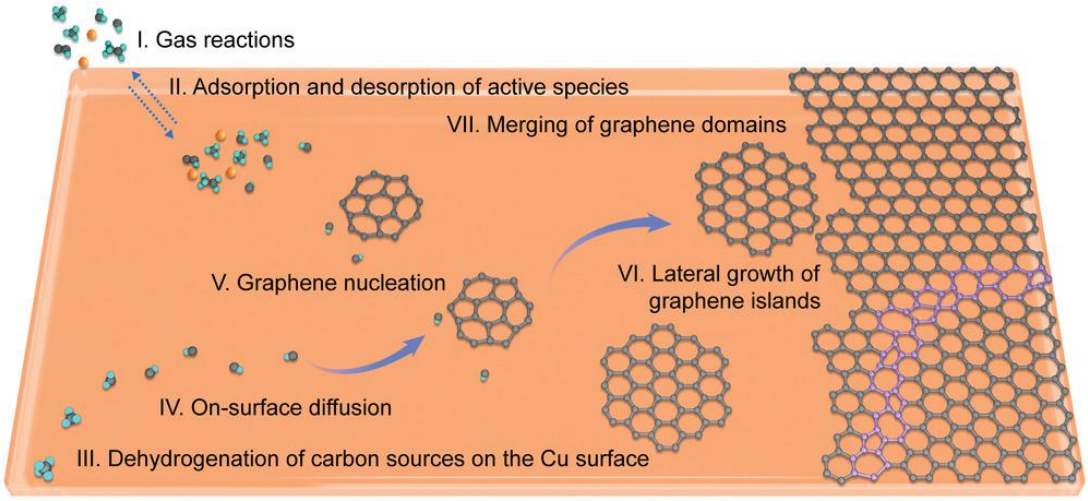

Figure. 1.3 Schematic representation of CVD growth of graphene on copper. [44]

On the other hand, graphene growth on Ni involves carbon dissolution and segregation which leads to multilayer graphene.[45,46] The dynamics of CVD growth of graphene on Cu and Ni are depicted in figure 1.3 and figure 1.4 respectively.

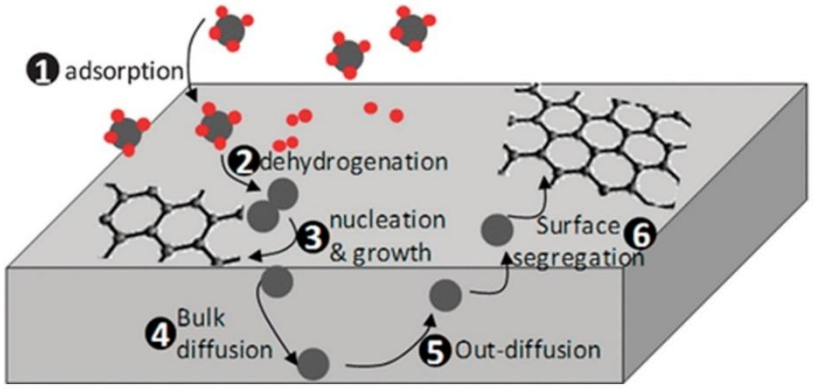

Figure. 1.4 Schematic representation of CVD growth of graphene on nickel.[47]

If grown on metallic polycrystalline Cu foils, graphene has a polycrystalline nature with the boundaries between differently oriented grains [48,49] being responsible for diminished transport and mechanical properties . [50–52] Grain boundaries can be avoided either adopting oriented Cu substrates (e.g., Cu(111))[53], or by growing large single-crystals of graphene with sizes larger than these of the targeted devices. This can be achieved by reducing the number of nucleation sites on the Cu surface by special treatments.[54–56] Typical graphene growth nucleation centers are defects such as impurities, particles and morphological features present on the Cu foils.[57] Chemical treatment achieved by dipping the Cu foil inside acetic or nitric acid solutions can also be utilized for Cu surface smoothening.[58,59]

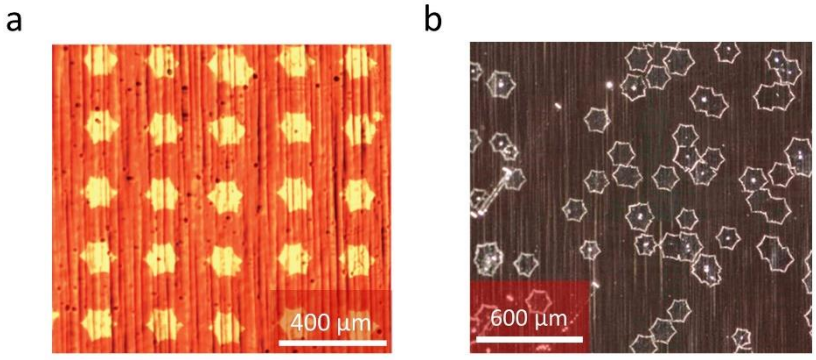

Figure. 1.5 (a) False color optical image of deterministically grown graphene crystals[60]; (b) and graphene single-crystals grown randomly.

For this thesis work we mostly adopted single-crystal graphene grown on Cu foils by using the methodology previously developed by our group which yields graphene single-crystals with lateral

size of hundreds of micrometers either in array or random fashion [56,60], as shown in figure 1.5 and elucidated in chapter 2. Before this doctoral work started, for CVD graphene crystals grown on Cu and transferred with wet transfer techniques room temperature (RT) carrier mobilities above 10 000 $cm^2V^{-1}s^{-1}$ without any encapsulation and on SiO_2 substrates were hardly reported. Low temperature (LT) mobility values up to 120 000 and 350 000 $cm^2V^{-1}s^{-1}$ were achieved with wet and dry transfer technique while encapsulating graphene with exfoliated hBN and measuring in vacuum.[61] Investigations of the mechanical properties of CVD graphene were not extensive due to delicate nature of freestanding graphene. Nevertheless, it has been shown that CVD graphene has mechanical properties comparable to exfoliated graphene with Young's Modulus of ~1 TPa.[62] All these properties make CVD graphene an enticing candidate for several applications, ranging from electronics to photonics and sensing .

1.3 Transfer of CVD graphene

As discussed in the previous section, CVD growth yields high quality large area graphene on metals which are however unsuitable substrates for the fabrication of electronic devices. Therefore, an effective transfer approach from metal to a target substrate is essential for different applications of graphene both in research and in industry. Here, some typical graphene transfer methods are illustrated such as wet transfer, electrochemical delamination and dry transfer out of which some are extensively used for this thesis work.

1.3.1 Wet transfer

CVD graphene wet transfer is a widely adopted technique among the research community because of its ease of implementation. In this approach, ionic etchants such as, ammonium persulfate ($(NH_4)_2S_2O_8$),[63–65] ferric chloride ($FeCl_3$),[66,67] or solutions of hydrogen peroxide and hydrogen chloride (H_2O_2: HCl)[68] are used to dissolve the metallic growth substrates. Graphene during the transfer process is supported by a polymeric layer and is ultimately transferred to the target substrate through various steps which are described below and depicted in figure 1.6. A thin polymeric film, most commonly a polymethyl methacrylate (PMMA) layer, is utilized during the transfer process of graphene grown on Cu foil. Furthermore, any possible unwanted growth of graphene on the opposite uncoated side of Cu is usually removed by solvent such as, 10% nitric acid (HNO3), or by exposure to O_2 plasma. The PMMA/graphene/Cu stack is immersed in a copper etchant to etch the Cu, after which a thorough cleaning of the sample with deionized water

is performed. Finally, the PMMA covered graphene, transferred on the target substrate is usually immersed in acetone for PMMA removal.

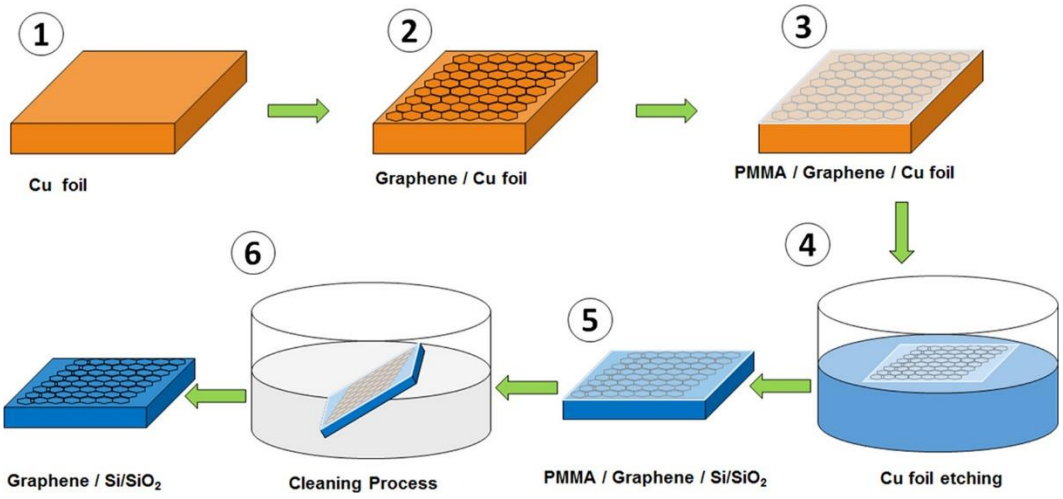

Figure 1.6 Depicting the different steps involved in the wet transfer of graphene.[69]

However, this transfer approach has some drawbacks such as the trapping of ionic species at the interface between graphene and the substrate which might act as scattering centers for graphene charge carriers with an overall detrimental effect for the electronic properties of the material.

1.3.2 Dry transfer

In the dry transfer technique, polymeric layers such as polydimethylsiloxane (PDMS)[61], polyvinyl alcohol (PVA)[70,71] and thermal release tape (TRT)[70] are typically used for graphene transfer onto a target substrate. This transfer process is possible if the van der Waals forces between graphene and the underlying substrate are weak. Usually, either transferred graphene onto a SiO_2 substrate or graphene onto an oxidized Cu substrate are adopted. [61,72] In particular, a two-layered transfer polymer composed of PVA and PMMA can be utilized to support graphene during dry transfer as well as to encapsulate it with hBN.[61] Furthermore, a hollow square of PDMS is generally used to support the stack of graphene or hBN/graphene in case encapsulation is needed. This stack is usually brought into contact with the graphene and separated

afterwards. While lifting the stack, graphene is picked up from the copper by exploiting the strong van der Waals interaction between graphene and hBN.

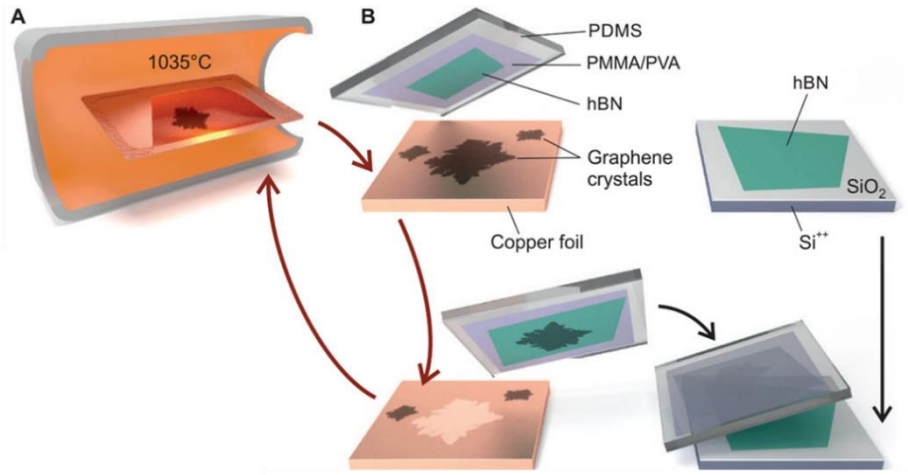

Figure 1.7 (a) Illustration of the CVD furnace with a copper enclosure inside. (b) Schematic process of the contamination-free transfer of CVD graphene from copper.[61]

Once the graphene is transferred, the polymeric layer can be removed, which leaves a hBN protected graphene layer. In particular, this method can be used to fully encapsulate graphene for obtaining high quality graphene devices.[61,72] Furthermore, graphene transferred by using this technique offers great quality but not scalability due to the limited size of the hBN flakes. A typical example of dry transfer technique is shown in figure 1.7.

1.3.3 Semi-dry transfer

This graphene transfer approach, also known as bubble-mediated transfer, is the one mainly used for transferring CVD graphene in this thesis work. Taking the advantage of electrochemical delamination, Wang et al. developed the bubbling transfer route for high-quality graphene transfer.[73] It is a very promising graphene transfer technique based on electrochemical delamination particularly adopted for the transfer of CVD graphene single-crystals. [60,73] In this transfer approach, O_2 and H_2 bubbles are generated via electrochemical reactions in which the graphene on the Cu growth substrate acts as either cathode or anode. These bubbles help to delaminate the graphene by applying a peeling force on it. This method is only limited to

conducting substrates which are appropriate to be used as electrodes. A clean removal of the graphene from the growth substrate can be attained, which also allows the substrate to be recycled, dissimilar to the wet transfer approach which chemically etches the metallic growth substrate. This transfer method is cost-effective as it diminishes the use of etchants or cleaning agents and is scalable. A typical graphene delamination setup is shown in figure 1.8.

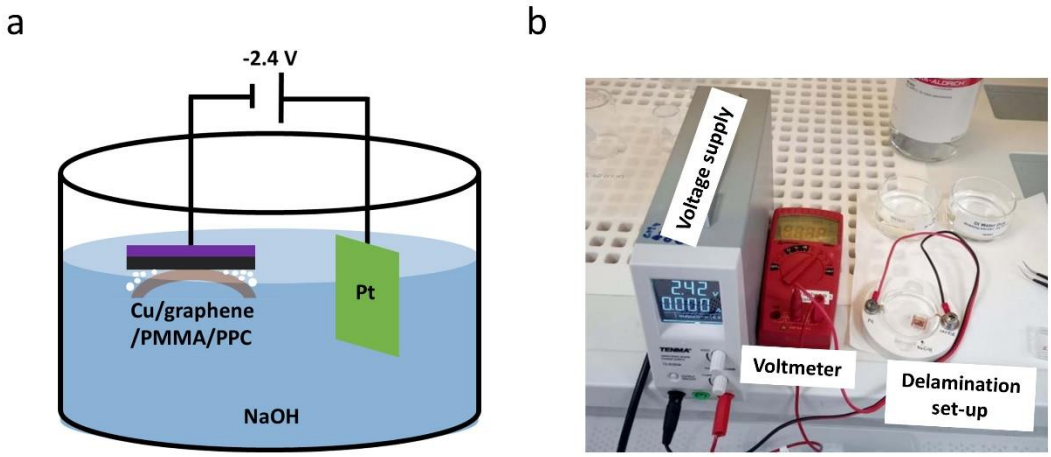

Figure 1.8 (a) Schematical representation of the set-up adopted in the semi-dry transfer process of CVD graphene; (b) home-made set-up used for the delamination process.

1.4 Graphene for technological applications

Thanks to its exceptional properties, graphene is not only a platform for fundamental studies but also a translational material, i.e., a material with great potential for technological applications. Its exceptional charge carrier mobility, ambipolar transport, broadband absorption, make graphene perspective adoption in electronics [74–77] and photonics [10,78,79] particularly promising. However, integration of CVD graphene in any of these technologies brings its own challenges which shall be resolved. In graphene based electronic and photonic devices such as FETs, Hall sensors, and photodetectors, graphene quality should be maximized over large areas. Hence, scalable CVD graphene with high mobility, low residual carrier density and homogeneous quality should be demonstrated. Also, attention should be paid to the possibility of obtaining devices with stable performance in ambient conditions over prolonged time periods. In this direction, attention should be paid to the presence of contaminants on graphene such as polymeric residues left on the surface during transfer. These polymeric residues should be removed from the graphene surface prior to its integration in technologies where high quality material is desired. In this thesis work,

we will address some of the challenges such as material scalability and cleanliness which are relevant for a successful integration of CVD graphene in devices such as Hall sensors and photodetectors. The development of compact and fast performing magnetic field and light sensor devices is of great interest for several technological applications, also in the automotive field.[80,81]

Indeed, in the automotive sector, graphene holds potential not only for the development of advanced sensors but also as a material to be integrated in different car body parts. Its mechanical resistance, heat dissipation properties, electrical conductivity, and low weight are characteristics highly beneficial for the engineering of novel automotive components. The Graphene Flagship together with Dallara Automobili spa, an Italian automotive manufacturer, has demostrated a graphene-enhanced sport car, the Dallara Stradale.[82] The interior of the car presents graphene composites of 10% by weight which have shown to pass the stringent Vertical Flammability Test (UL94-V) REF. Recently, within the Graphene Flagship, Varta and BMW have focused on developing silicon-graphene composite anodes for high energy density lithium-ion batteries.[83] Also, graphene could be potentially adopted in tires. In general, together with rubber, a filler material is needed to improve the rheological and mechanical properties of rubbers in tires. In later times, silica has extensively been used to replace carbon black as a filler material.[84] Silica has been shown to being advantageous for higher stiffness, tear strength, modulus, and to overall improve the rolling resistance of the tires.[84,85] Yet, it is not always easy to disperse due to strong polar bonds among filler particles which restricts its use in non-polar rubbers.[85] Recently, graphene has been suggested as a potential nanofiller candidate for the improvement of the overall properties of tires. In order to have good quality composites, proper graphene dispersion in rubber matrixes shall be achieved. Recent efforts have shown that Zn functionalized graphene can be used for better dispersion.[84] Yet, Zn is an undesirable heavy metal for the environment and therefore other sustainable, eco-friendly solutions shall be found to move toward the development of “green tires” for future automotive applications. Furthermore, in order to make graphene enhanced tires effectively adopted, the electrical conductivity of graphene-rubber composites shall be investigated and ultimately ensured. In the second part of this thesis work, we have thus analyzed the impact of rubbers on the electrical properties of graphene. Subsequently, we have investigated the possibility to functionalize graphene with nitrogen rich molecules such as pyrroles and tetrazoles for improving its dispersion in rubber matrixes and engineer through functionalization

of graphene potentially conductive paths. For both these studies we have adopted CVD graphene as an ideal model system to fully investigate the modification of graphene electronic properties when in contact with rubbers and graphene functionalization mechanisms. Furthermore, as a final attempt we moved towards a more realistic and economically viable approach by replacing CVD graphene with graphene inks. Indeed, inks are the final graphene form that would be utilized to obtain graphene-enhanced automotive tires as already demonstrated in tires for bikes which have been commercialized in recent years and are expected to possess longer durability and improved wet grip.[86]

1.5 Thesis outline

The goal of this thesis work is twofold: (i) it aims at demonstrating the potential of graphene for the development of high-performing magnetic and light sensors which could be of interest for a number of applications, including automotive ones; (ii) it investigates the interaction of graphene and rubbers and tries to identify possible functionalization pathways that could be of use for the realization of graphene-enhanced tires. Apart from the introductory **chapter 1**, the content of the different chapters is summarized below:

- **Chapter 2** reports an overview of all the methodologies and experimental techniques which are utilized in this thesis such as graphene growth, graphene transfer, device fabrication and related characterizations techniques.
- In **chapter 3** we demonstrate a novel graphene cleaning approach which leads to the development of high mobility graphene FET devices. We compare spectroscopic and microscopic characterization of the graphene cleaned with approaches typically adopted in literature with the one developed during this doctoral work. Raman spectroscopy, atomic force microscopy (AFM), X-ray photoelectron spectroscopy (XPS) and transport measurements are used to demonstrate the effectiveness of the reported cleaning approach. The results of this chapter serve as a basis for the rest of the thesis. Indeed, thanks to the ultra-clean graphene obtained with the reported cleaning approach we are able to develop high-performing sensors and to investigate the interactions between clean graphene and rubbers.
- **Chapter 4** describes the development of scalable highly-sensitive graphene-based Hall sensors and their stabilization via encapsulation with a thin polymeric layer. We discuss our device fabrication process and contextualize our results with the state-of-the-art results. Indeed, the

current related sensitivity of our devices is the highest reported to date with CVD graphene without the need of encapsulation with exfoliated hBN. The presented work reports a realistic pathway for the fabrication of graphene-based scalable highly-sensitive Hall sensors with the potential of outperforming conventional semiconductor-based Hall sensors.

- **Chapter 5** presents the development of polymer-capped graphene visible-light photodetectors based on pn-junctions. First, an experimental approach to create ambient stable pn-junctions of CVD graphene is shown. Afterwards, the chapter focuses on the electrical and optoelectronic behavior of these graphene based pn-junction devices. Physical mechanisms behind the photoresponse, responsivity and other main properties of the photodetector are investigated and discussed. In the final section of the chapter, pn-junction graphene photodetectors created with different approaches are compared with the ones developed for this thesis work. This work demonstrates an alternative approach for developing stable, semi-encapsulated graphene based pn-junction visible photodetectors to favor graphene inclusion in optoelectronic technologies such as optical communication in vehicles.
- In **chapter 6**, fundamental studies are performed to understand graphene potential for tire applications. Initially, CVD graphene was non-covalently functionalized with rubbers and their influence on the electronic properties of graphene was investigated. Subsequently, various approaches of graphene functionalization with organic molecules of interest in the tire industry such as tetrazoles and pyrroles were attempted and resulting graphene electronic properties were studied. As a final step, for a more realistic study for the tire industry, investigations of graphene inks functionalization with organic molecules were carried out. The properties of graphene and graphene inks before and after functionalization, were studied mainly by using Raman spectroscopy. This fundamental study provides an important understanding for using functionalized graphene/graphene inks in tires which is important for overall improvement in currently existing tire technology.
- Finally, **chapter 7**, delivers an overall summary of this thesis work and suggestions for future research are offered.

Chapter 2

Experimental methods

In this chapter, the experimental techniques used in this work are presented. For graphene growth, chemical vapor deposition (CVD) has been implemented by using a cold wall reactor. Raman spectroscopy and atomic force microscopy (AFM) was used for structural and morphological analysis of graphene. Electron beam lithography (EBL) was used for fabricating the graphene based field effect transistor (FET). A custom-made four-probe setup was used for electrical and magnetic transport measurements of the graphene FET devices. Furthermore, additional techniques impacting this research such as scanning electron microscopy (SEM), X-ray photoelectron spectroscopy (XPS), reactive ion etching (RIE), and thermal evaporation are briefly introduced.

2.1 CVD technique

As introduced in chapter 1, high quality CVD graphene is a an enticing material for its perspective integration in different technologies. In particular, graphene is commonly grown on different metallic substrates such as Cu [87], Ni [88] and Pt [89] while exploiting their catalytic behavior. However, Cu is considered as the best platform for graphene growth due to its cost-effectiveness and low carbon solubility. By adopting different approaches and adjusting the CVD parameters, single-crystalline or polycrystalline graphene can be synthesized on Cu foils. Moreover, it is possible to grow scalable, high-quality and high-mobility single-crystal graphene randomly or at pre-determined position for their use in optoelectronics and electronics.[60]

2.1.1 SLG deposition on Cu foil by CVD

In this work, single-crystal graphene with a lateral size of 200-250 µm was synthesized by using a cold wall 4'' Aixtron-BM reactor on Cu foil of 2×2 cm^2 area with 25 µm thickness. Initially, the Cu foil was electropolished prior to graphene growth, as shown in figure 2.1. This has been shown to be effective in reducing graphene nucleation density.[90,91]

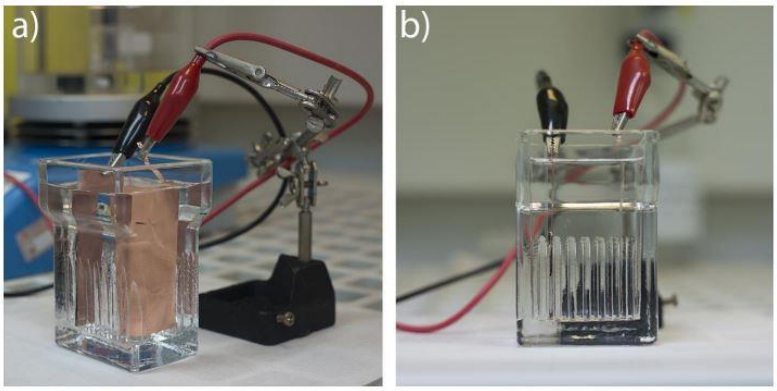

Figure. 2.1 (a) The electrochemical polishing cell; (b) Side profile image shows the parallel position of the Cu foils ensured by the grooves of the staining jar.[56]

Subsequently, the graphene films were grown at 25 mbar of pressure in the same reactor. CH_4 was used as a precursor with a flow-rate of 1 sccm, Ar and H_2 gases were flown as carrier/process gases at 900 sccm and 100 sccm, respectively. A typical quartz/graphite sample enclosure was placed in the CVD reactor as depicted in Fig.2a to minimize precursor flux on the catalytic substrate as described in.[92] The temperature profile of the CVD growth process is depicted in figure 2.2, indicating four fundamental parts of the growth process. The annealing as well as the growth of the graphene was performed at 1060°C, calibrated according to the melting point of Cu foil. The annealing process was performed in non-reducing argon (Ar) atmosphere to preserve surface oxidation as described previously.[92]

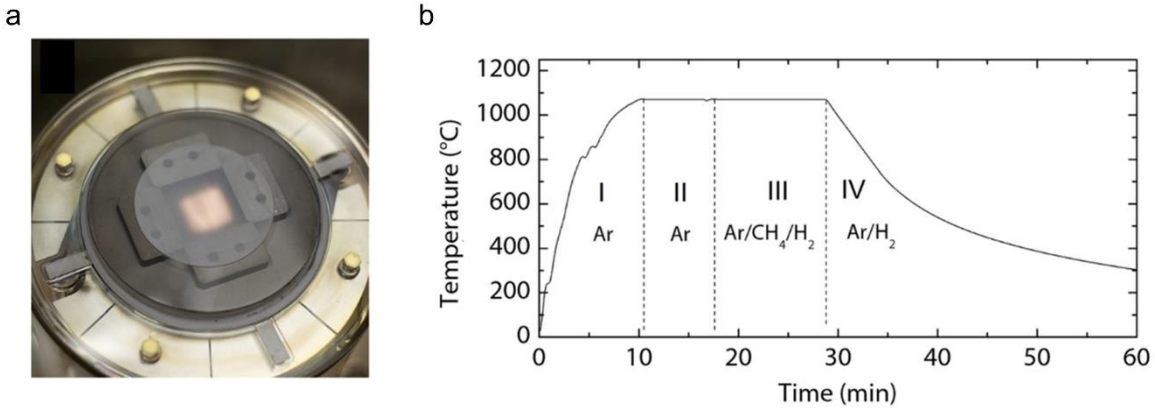

Figure. 2.2 (a) Quartz/graphite sample enclosure; (b) Temperature profile of a typical CVD growth process. (I) Temperature ramp-up, (II) annealing, (III) growth, (IV) cool-down.[92]

Graphene single-crystals were grown on plane electropolished Cu foils or on patterned Cu foils where, after electropolishing, metallic seed arrays were patterned to obtain deterministic growth [60]. The resulting growths are reported in Fig. 2.3. Specifically, deterministic growth was obtained by using optically lithographed chromium (Cr) nano-disks of 25 nm thickness and 5 μm width.

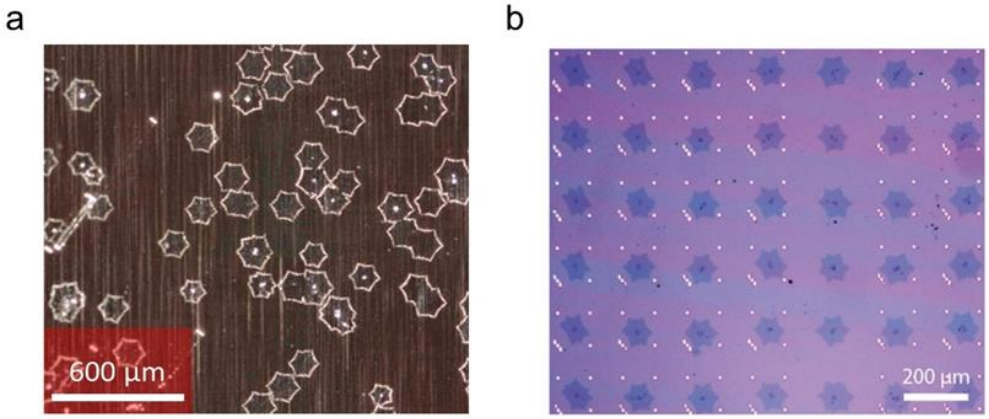

Figure. 2.3 (a) Optical image of randomly grown graphene on Cu foil; (b) Optical image of single-crystal array transferred on Si/SiO_2 substrate.[60]

The Cr seeds are completely removed during the graphene growth process as reported in [60]. After growth, the CVD grown graphene single-crystals were transferred from Cu to SiO_2 substrate for further characterizations by using the semi-dry transfer technique [56] which is detailed below.

2.2 Semi-dry transfer of CVD graphene

Semi-dry transfer, also known as electrochemical delamination or bubbling transfer, was first reported in 2011 [73,89] and subsequently adapted by our group to allow for a clean transfer of graphene and graphene arrays with a high yield to a target substrate.[56,60,93] Specifically, a thin PMMA carrier membrane (typically about 100 nm) is spin-coated on the Cu foil with graphene and the substrate with the PMMA layer is heated on a heating plate at 90°C for few minutes. Also, an additional 1.5 μm PPC layer is employed for a stronger mechanical support to the graphene layer. The graphene/PMMA/PPC stack is then heated again to 90°C for 2 minutes. A PDMS frame is attached to the edge of the Cu foil to facilitate manual handling as previously reported by our group.[93] The double polymeric membrane provides mechanical and thermal advantages during the transfer process as discussed.[93] SLG electrochemical delamination is performed in 1 M

NaOH. Cu/SLG is used as the anode, and ~2.4 V is applied with respect to a Pt counter electrode. The voltage is controlled to keep the current ~3 mA to avoid excessive formation of H_2 bubbles, which may cause damage to SLG. The freestanding polymer/SLG membrane is then removed from the electrolyte, rinsed 2 times in DI water, and dried in air. Using a custom-built aligned lamination setup (see figure 2.4) , the graphene/polymer stack is then transferred on a SiO_2/Si wafer heated to 90°C. The PDMS is then peeled off and the polymer coating is removed by leaving the sample in acetone and isopropanol.

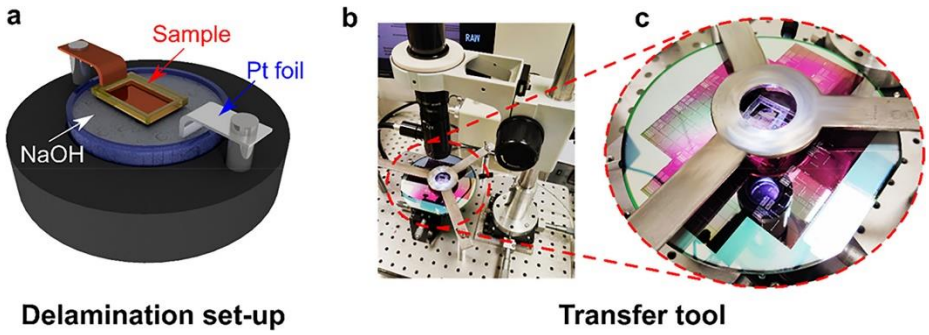

Figure. 2.4 (a) Schematic of the electrochemical delamination setup. (b) Transfer tool holding the delaminated SLG sample and (c) Close-up of SLG/PMMA membrane, with a PDMS frame aligned onto the target substrate.[94]

2.3 Raman spectroscopy

Raman spectroscopy is a versatile tool to identify and characterize the chemical and physical properties of materials both at the laboratory and production scale. This technique basically detects different vibrational modes of the molecules while relying on the inelastic scattering of the light interacting with molecules.

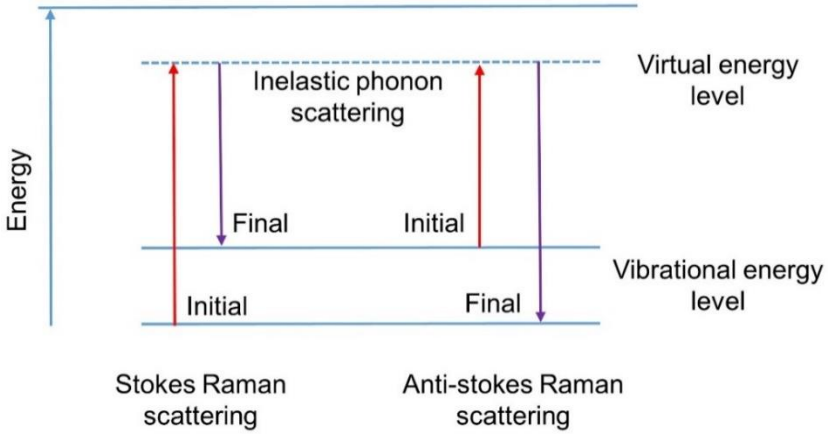

Figure. 2.5 Schematic representation of Stokes and anti-Stokes Raman scattering process.

Raman scattering can be divided in two different types, as depicted in figure 2.5. Stokes Raman scattering (anti-Stokes Raman scattering) takes place when the molecule is promoted from a ground (vibrational) to a virtual state and then drops back to a higher energy (lower energy) vibrational (ground) state so that the energy of the scattered photon is lower (higher) than that of the incident one. In particular, Raman spectroscopy is a fast and non-destructive tool for characterizing the electronic, optical and phononic properties of graphene. Pristine graphene has two distinctive peaks at ~1580 cm^{-1} and at ~2700 cm^{-1} known as G-peak and 2D-peak respectively.[95] The G-peak in graphene originates from a first order phonon scattering process while the 2D-peak comes from the double resonance scattering process of electron and holes. Defective graphene shows an additional peak at ~1350 cm^{-1} known as D-peak [95], which is due to the breathing mode of six-atom carbon ring and is

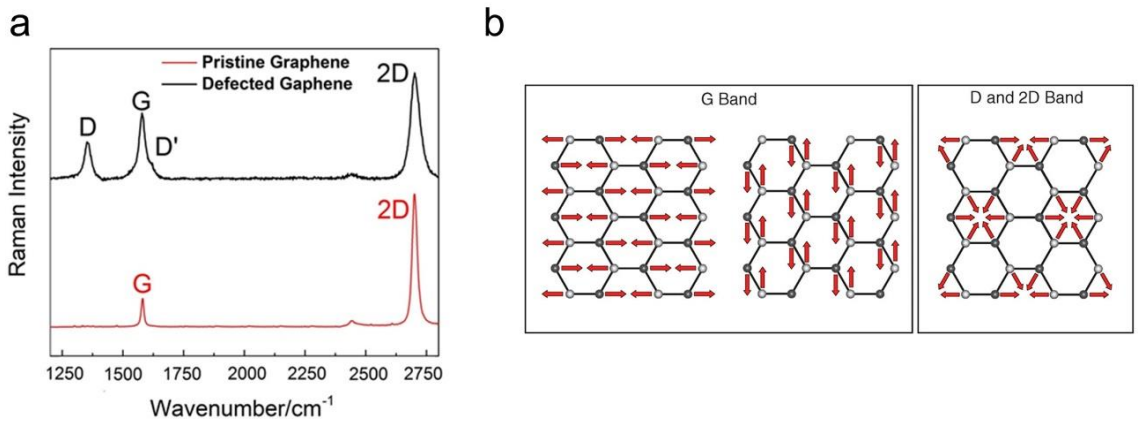

Figure. 2.6 (a) Raman spectra of pristine and defected CVD graphenemeasured at 488 nm excitation wavelength [96]; (b) Vibration modes associated to G, D and 2D-peaks of graphene.[97]

activated by a defective site in graphene. In figure 2.6a, the typical Raman peaks of graphene and defected graphene and their corresponding vibrational modes are reported. The G-peak originates from two different in-plane lattice vibrations as shown in figure 2.6b.[98] The 2D peak is the overtone of the D band, which comes from the in-plane vibrational mode of the carbon rings known as double resonance process.[99]

Raman spectroscopy can be used to determine the doping and strain in graphene. Specifically, the shift in the G-peak position of graphene determines the n or p-type doping in graphene.[100,101] The intensity and area ratio of the 2D and G-peak of graphene can also be used to estimate the doping in graphene.[100,102] However, we know that the Raman spectra of graphene is not just affected by doping[100] but also by strain.[103] To estimate the strain of graphene, the rate of the change of G and 2D-peak positions can be utilized by using Grüneisen parameters.[104] Furthermore, the ratio of the intensity of 2D and G-peak has been used to estimate the number of graphene layers as previously reported.[105,106] Furthermore, the full width at half maximum (FWHM) of the 2D-peak of graphene is also sensitive to strain variations and is typically used as a graphene quality indicator on SiO_2 substrates.[107] In this thesis, Raman spectroscopy was performed with a Renishaw InVia system with a 532 nm laser, and a 100× objective, giving a spot size of ~0.8 μm. Laser power was set to ~1 mW to minimize heating. Raman mapping was performed using a motorised stage, over an area of 12 × 12 μm^2 with a step size of 1 μm.

2.4 Atomic force microscopy

Atomic force microscopy (AFM) is a technique useful for analyzing the morphology of the surface of materials. This technique works by unraveling the intermolecular vdW forces at the nanoscale level with high atomic resolution. Typically, the sharp tip of a flexible cantilever is scanned across the sample surface. A laser is focused on the cantilever which generates deflected light from the surface of the sample and the scanning feedback is collected by a position sensitive detector. AFM usually works in different modes named as contact, non-contact and tapping mode. In contact mode, AFM works in a repulsive force regime, and the feedback loop keeps the force between the tip and the surface constant.

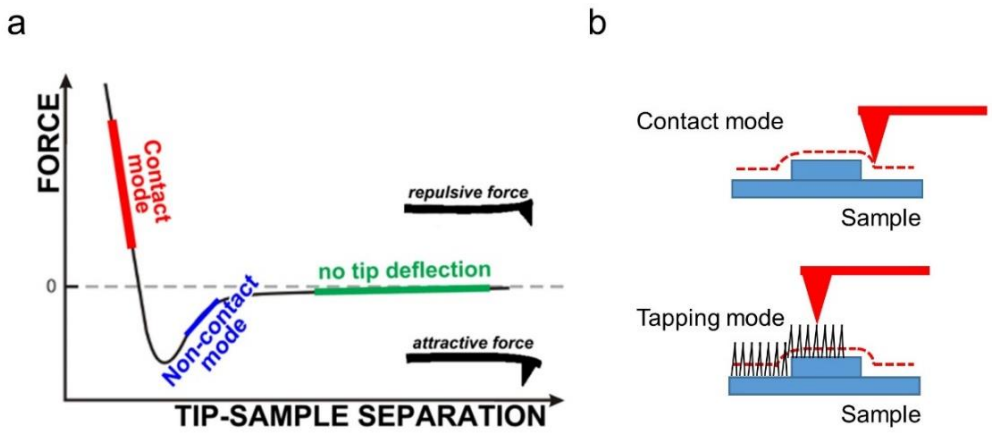

Figure 2.7 (a) Force regime which governs the AFM measurement[108]; (b) Schematics of contact and tapping mode operation.

In tapping mode, the cantilever oscillates around its resonance frequency and the tip periodically taps the surface while the feedback loop controls the changes in amplitude, resonance frequency and phase of the cantilever. In this thesis both contact and tapping AFM modes were exploited. AFM was performed with a Dimension ICON-PT (Bruker Scan-Asyst). Gwyddion software was used to process the AFM images, extract the surface profile and to perform surface roughness calculations and particle analysis.

2.5 X-ray photoelectron spectroscopy

X-ray photoelectron Spectroscopy (XPS) is a surface sensitive technique probing the sample surface, its composition and chemical bonding state by bombarding X-rays on the sample surface. The working principle of XPS is based on photoelectric effect in which electrons are emitted while irradiating the sample surface with light. In particular, the sample is irradiated with soft X-rays (energies lower than ~6 keV) and the kinetic energy of the emitted electrons is analyzed. The emitted photoelectron is the consequence of complete allocation of the X-ray energy to a core level electron. XPS can usually provide information on the chemical elements present within a few nm of the sample surface.

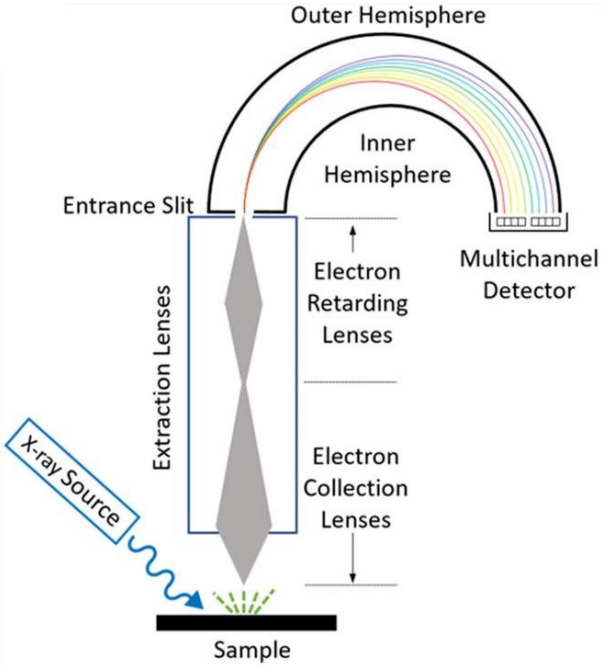

Figure 2.8 Schematics of the major components of an XPS.[109]

The energy resolution of the XPS spectrometer is enough to determine changes in binding energy for different chemical bonds. In this thesis work, XPS measurements were conducted on a Thermo Fisher Scientific Escalab 250 xi, equipped with a monochromatic Al-Kα anode (1486.6 eV). Also, XPS Imaging was exploited for Small-area XPS (SAXPS) for spectroscopy with a space resolution of 10 – 200 µm. Additionally, maps were recorded in the energy range of C 1s, O 1s and Si 2p, using a 200 eV pass energy and 0.1 eV energy step between each acquisition and all the associated binding energies were corrected with respect to the C 1s at 284.5 eV. A basic schematic of the major components of XPS is shown in figure 2.8.

2.6 Scanning electron microscopy

Scanning electron microscopy (SEM) utilizes electrons to form an image instead of photons. It is one of the most common techniques used for characterizing the surface of micro and nanomaterials. The focused electron beam scans the surface of the sample and forms an image of it. Electrons interact with the atoms of the sample and produce various signal of the sample surface and its composition. The electron beam scanned in raster pattern on the sample and as a consequence different type of signal is generated such as, secondary electrons (SE), back-scattered electrons (BSE), characteristic X-rays etc. as shown in figure 2.9. Most commonly, the secondary electrons emitted by atoms of the sample, are detected by using a secondary electron detector to form an image. In general, the intensity of the emitted signal produces the resulting image upon being collected at the detector.

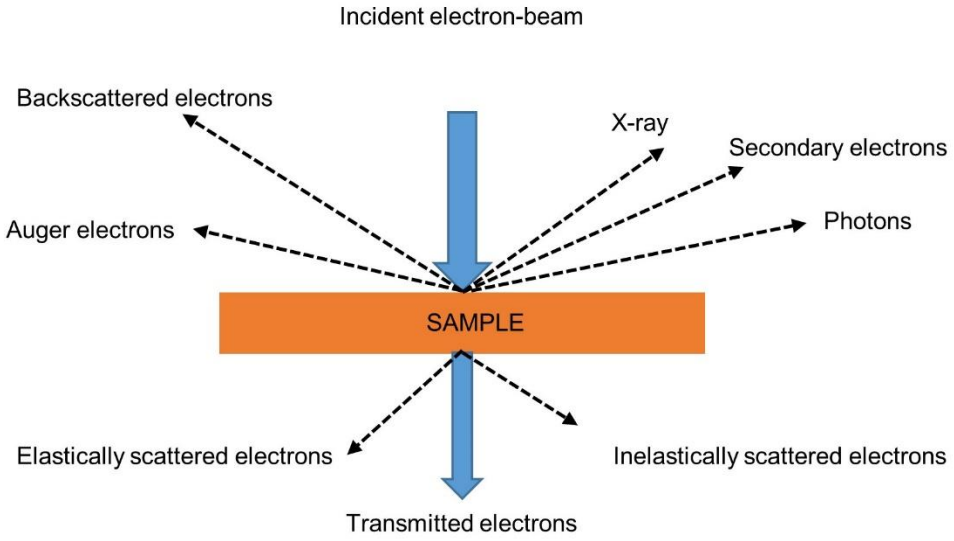

Figure 2.9 Schematics of various signals generated by interaction of electron beam with the sample.

In this thesis, a Zeiss MERLIN field emission SEM was used at 5keV with an in-lens detector for detecting secondary electrons, which could lead to images with a lateral resolution down to 0.8 nm.

2.7 Electron beam lithography

Electron beam lithography (EBL) is a technique used for patterning desired structures on a surface covered with resist (an organic polymer i.e., Poly (methyl methacrylate) (PMMA)) used in nano/microfabrication. The incident electron beam changes the solubility of the resist after interacting with its molecules thus enabling selective removal of either the exposed or non-exposed regions of the resist by immersing them in a solvent called developer. The main advantage of this technique is that it can draw structures in the range of a few nanometers. Figure 2.10 is showing the process flow of a typical EBL process to generate desired structures.

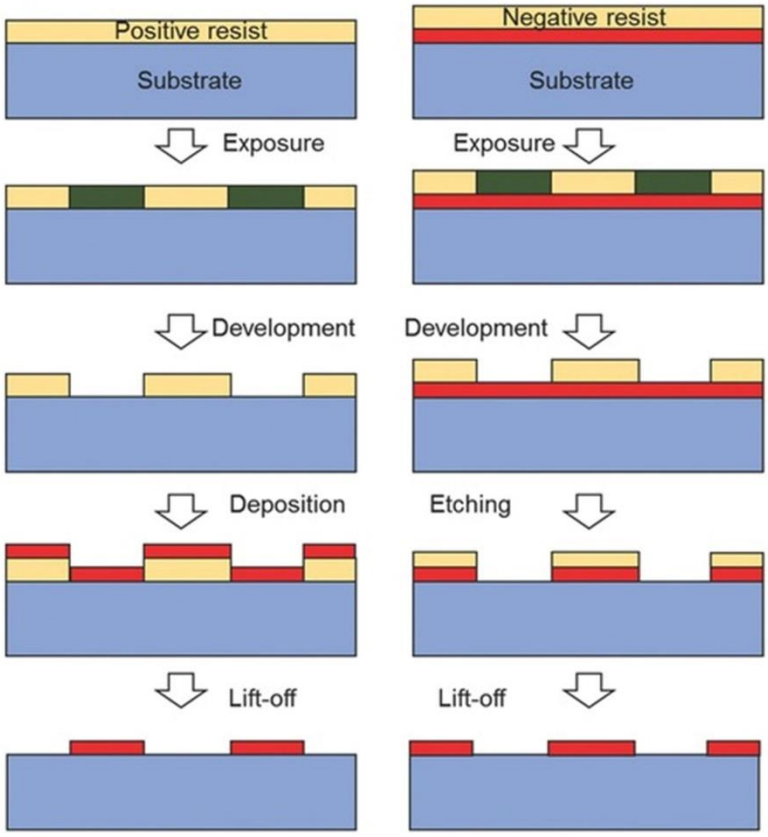

Figure 2.10. Process flow of generating desired patterns on the substrates by using electron beam lithography with positive/negative resist.[110]

To fabricate the graphene-based field effect transistors (GFETs) for this thesis work, a Zeiss UltraPlus scanning electron microscope (SEM) at 20 kV and Raith Elphy Multibeam EBL system was used (Figure 2.11). The patterns were defined in positive e-beam resist (PMMA 950k, Allresist GMBH).

Figure 2.11. Picture of the Zeiss UltraPlus SEM equipped with Raith Elphy Multibeam EBL system located at NEST laboratory in Pisa.

2.8 Reactive ion etching

Reactive ion etching (RIE) is a plasma etching technique used in nano/ microfabrication process. RIE is a dry etching technique which has different characteristics than wet etching. Chemically reactive species (ions) are accelerated toward the substrate, to get rid of a precisely deposited material. The special characteristic of RIE technology is its directional (usually anisotropic) etching ability. The plasma is produced under low pressure in vacuum by an electromagnetic field by applying a RF power to the cathode while keeping the anode grounded, as shown in figure 2.12. Once the plasma is generated, a large negative voltage is formed at the bottom electrode (due to

accumulation of electrons), while the plasma retains a low positive voltage. Due to this large voltage difference, the positive ions drifts toward the substrate, where they collide with the samples to be etched. These ions interact chemically with the material on the substrate. Additionally, owing to the vertical supply of reactive ions, reactive ion etching produces anisotropic etch profiles and etching conditions strongly depends on the different parameters i.e., RF power, gas flow, pressure etc. In this thesis, a parallel-plate reactive ion etching (RIE) plasma system (Sistec) was used at 35 W with Ar/O_2 flow of 5/80 sccm, respectively.

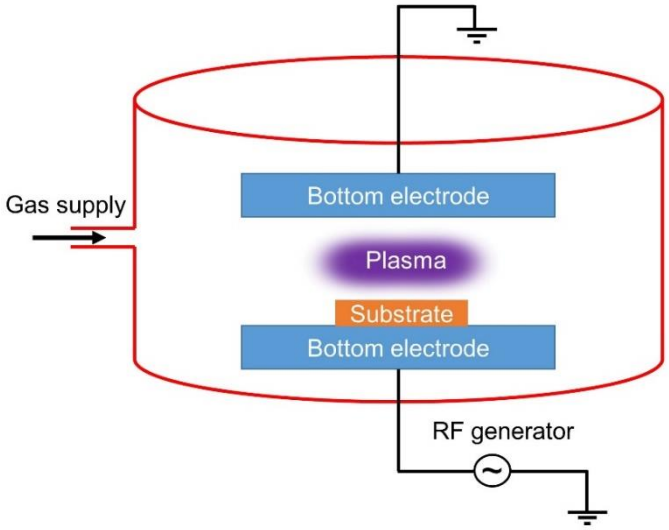

Figure 2.12. Schematics of the reactive ion etching (RIE) mechanism.

2.9 Thermal deposition of thin-film

Thermal evaporation is a common method used in thin film deposition of different materials (e.g., metals).

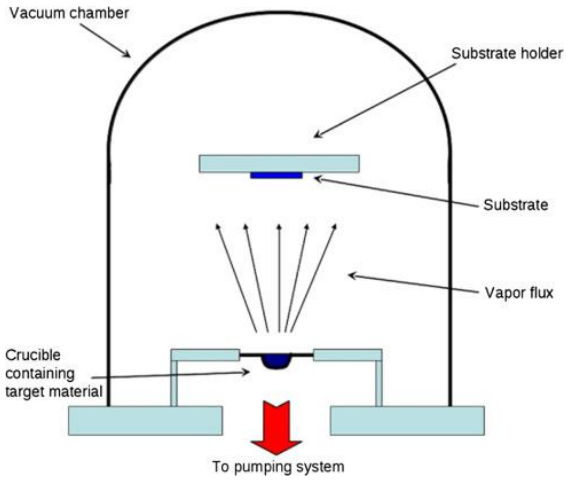

Figure 2.13. Schematic drawing of thermal evaporation.[111]

2.10 Electrical and magnetic transport characterization

Graphene field effect devices were characterized electrically by using a home-made four-probe transport setup with tungsten tips on micropositioners. The experimental setup encompasses a current source (Keithley-2450) that supplied the source-drain current to the graphene device and the voltage drop across the channel then measured by a multimeter (Keithley-2450). Additionally, another Keithley-2450 is used to apply the back gate voltage while measuring the leakage current through the gate oxide.

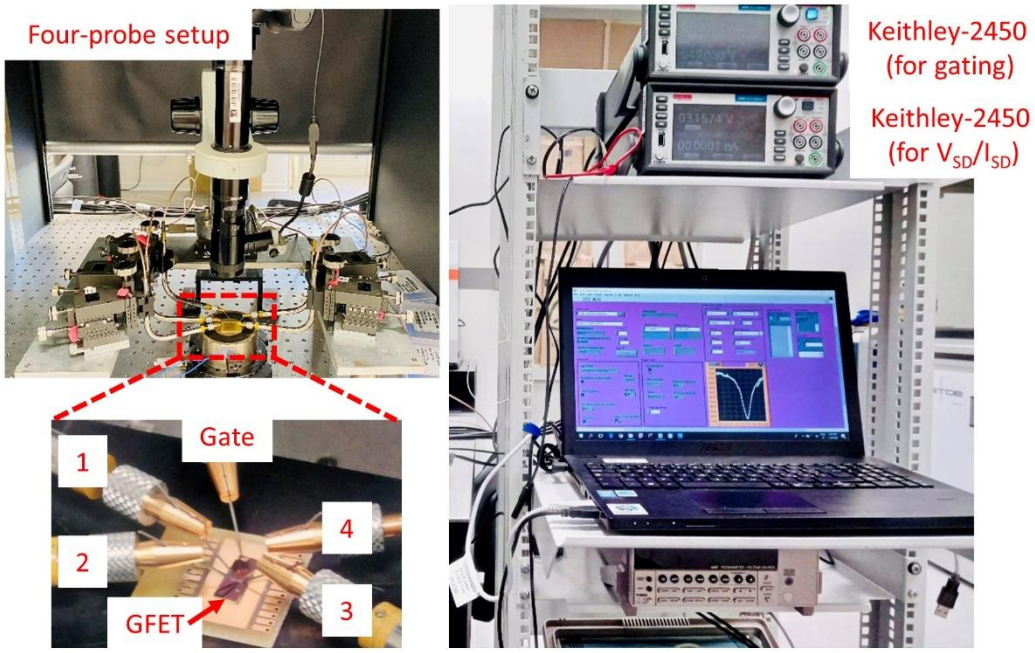

Figure 2.14. Picture of the home-made four-probe electrical and magnetic measurement setup with terminals (1,2,3,4) which can be used to apply voltage/current to channel and to measure current/voltage drop.

Furthermore, the four-probe approach was adopted for minimizing the contact resistance of the graphene-based field effect devices (GFETs). The homemade four-probe electrical setup is shown in figure 2.14.

Additionally, for magnetic characterization (specifically for Hall-measurement), a similar setup was used and a magnetic field of 0.37 T was applied by using a permanent magnet. The noise-frequency characteristics of the graphene devices were measured by using a lock-in amplifier (EG&G 7260 DSP) with a constant applied current of 1μA while changing the frequency.

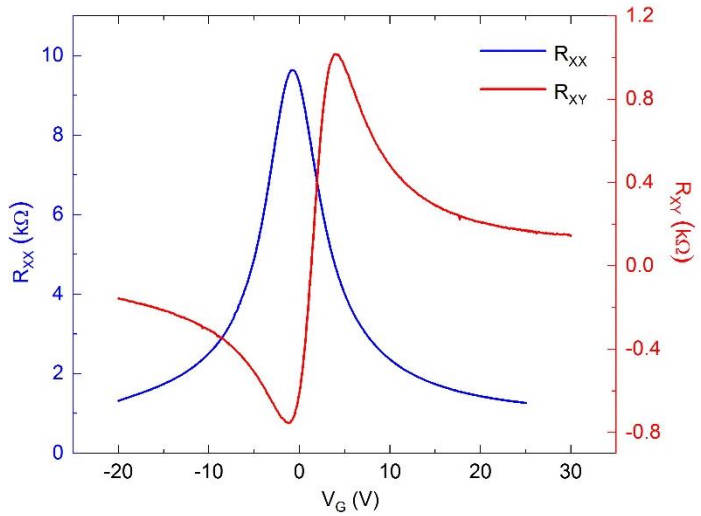

Figure 2.15. A typical resistance (R_{XX}) curve of graphene without magnetic field and with magnetic field (Hall-resistance, R_{XY}) as a function of applied back-gate voltage.

The typical resistance curve of graphene devices with and without magnetic field is reported in figure 2.15. In particular, figure 2.15 shows the typical ambipolar behavior of graphene whether the magnetic field is applied or not, where holes are contributing to the conduction in negative voltage region, and electrons in the positive region. This behavior is different from most of the conventional semiconducting materials, in which the transport is solely due to either electrons or holes.

2.11 Optoelectronic characterization

Graphene optoelectronic devices such as the graphene-based pn-junction photodetectors presented in chapter 5 were characterized in a custom-made setup within the Raman InVia system. This set-up was composed in the following way: a moving stage where the photodetector device could be mounted, electrical probes to connect the source-drain terminals of the device, two lasers of 532 nm and 473 nm which could be focused on the pn-junction of the photodetector with ×50

magnification while performing optical measurements. Figure 2.16 is depicting the graphene photodetector mounted under the microscope.

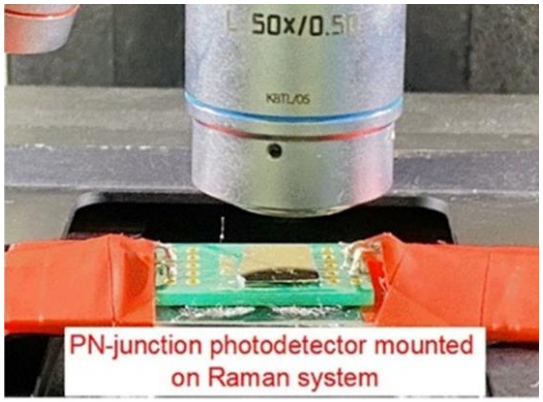

Figure 2.16. Bonded graphene pn-junction device under Raman objective used for optoelectronic measurements.

Chapter 3

Ultra-clean high-mobility graphene

In this chapter, we describe a novel approach for the production of ultra-clean and high-mobility CVD graphene. Specifically, we develop and present a method, a two-step wet chemical cleaning route, to clean transferred CVD graphene on technologically relevant substrates such as silicon-dioxide on silicon (SiO_2/Si) and assess the quality of the obtained graphene via morphological, structural, chemical and electronic characterization performed via AFM, Raman spectroscopy and XPS. Furthermore, electrical transport measurements demonstrate the high-mobility of the graphene devices fabricated upon adoption of the two-step cleaning approach. Finally, we discuss the relevance of ultra-clean high-mobility graphene devices in different technological applications. The results presented in this chapter are published in Ref. [112].

3.1 High-quality CVD graphene

Over the past years, CVD graphene has emerged as a material with a great potential for different technological applications [112] thanks to its many exceptional properties such as high electrical and thermal conductivity.[6,75,113,114] Because of remarkable advancements made in the field of scalable graphene synthesis via CVD, wafer-scale graphene is now accessible and ready to be integrated for different technological applications ranging from sensing, photonics, to optoelectronics.[94,115,116] Most of these applications require high-mobility ultra-clean graphene directly on a technologically-relevant substrate such as SiO_2/Si.[117,118] For example, high charge carrier mobility and low residual charge carrier density are main requirements for graphene use in sensing devices such as Hall sensors[9,119], and in optoelectronic devices such as photodetectors, modulators etc.[10,11,94] Both Hall sensing and light sensing devices are relevant devices in the automotive industry.[80,81] However, a well-known issue in CVD graphene processing is the presence of polymeric contamination: this is a hurdle that affects graphene performances and negatively impacts the integration of graphene in several applications.[120–122] The reasons behind graphene polymeric contamination are the following: (1) the transfer step needed to remove CVD graphene from the metallic growth substrate and place it on target substrates involves coating of the graphene with polymeric resist (which acts as the supporting layer during the transfer, as discussed in paragraph 2.2); (2) the polymeric coating implemented

during optical or e-beam lithography (performed to define devices). In particular, Polymethyl methacrylate (PMMA), is commonly used during the graphene transfer process as well as for fabrication [123], and the existence of PMMA residues on graphene due to strong physical and chemical adsorption effects is cause of concern.[124] Indeed, due to the atomic thickness of graphene, surface adsorbates can induce charge carrier scattering, consequently reducing the carrier mobility of graphene devices.[125] Different techniques have been used to address the issue of the polymer contamination on graphene such as mechanical cleaning with the tip of an atomic force microscope (AFM) [126,127], current-induced cleaning [128], high-temperature annealing [129,130] and wet chemical cleaning. [122,131] However, each of these approaches contains its own shortcomings. Polymer residues can be effectively cleaned from the graphene surface by using an AFM tip operated in contact mode, however, this method is very time-consuming and the areas that can be actually cleaned are presently very limited in size. Similar constraints apply to current annealing. Thermal annealing is compatible with large-scale processing however, when performed on graphene/Si–SiO_2, it appears to increase doping and decrease mobility by inducing strong interactions between graphene and the substrate. [130,132] At present, wet chemical cleaning is one of the most adopted approaches to clean scalable graphene prior to device fabrication. [129] Yet, particular care should be paid in order not to introduce additional contaminants during the process. With such wet approaches, when measuring large-area graphene samples, (i.e. chips containing more than 10 test structures) in ambient conditions, carrier mobility usually does not exceed 5 000 $cm^2\ V^{-1}\ s^{-1}$.[65,94] To realize high-performing optoelectronic and photonic devices of technological relevance, mobilities as high as 10 000 cm^2/Vs would be desirable.[133] Hence, to realize the full potential of CVD graphene in high-performing applications, wafer-scale ultra-clean graphene shall be demonstrated. The next paragraph describes the cleaning solution implemented during this work, which has led to measuring state-of-the-art room temperature CVD graphene mobilities, as it will also be discussed in chapter 4.

3.2 Two-step cleaning approach for high-quality graphene

In first place, graphene was grown via CVD either with random nucleation or in matrixes (see Paragraph 2.2 and [62] and was transferred from Cu to Si/SiO_2 using the semi-dry transfer method described in 2.3 optimized by our group. [94] With respect to the classical transfer reported in literature, in our work we have developed and patented a double polymeric membrane containing a PPC layer optimized to provide ideal mechanical support, maximum transfer yield, and high

optical transparency to allow for deterministic transfer of graphene.[94,95] In the classical graphene semi-dry transfer approach reported in literature, graphene is cleaned with acetone and isopropanol after transfer. In our work we have denoted this procedure as one step cleaning (1SC) approach. As discussed above and reported in literature, after the standard acetone cleaning (i.e., 1SC), polymer is not removed entirely from the graphene surface and hinders the properties of graphene. To remove these remaining residues more effectively, a two-step cleaning approach (2SC) was developed, as schematized in figure 3.1.

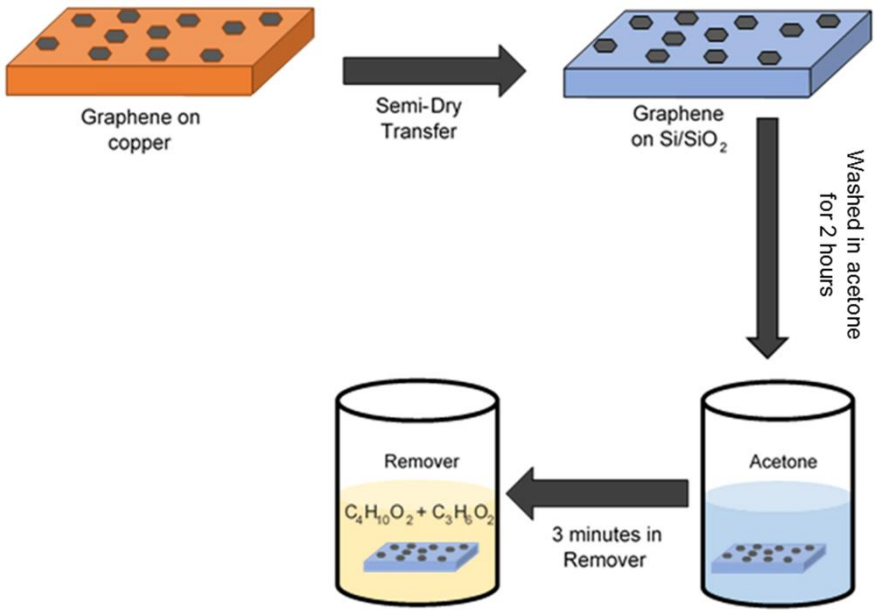

Figure. 3.1 Schematics of the transfer and two-step cleaning process of CVD graphene developed in this work.

In the case of 2SC, the steps of 1SC were followed by a 3 min bath in remover AR 600-71, a 10 s rinse in deionized water, and by drying with compressed nitrogen. AR 600-71 (Allresist) is a two-component solvent (70%, 1,3-dioxolane and 30%, 1-methoxy 2-propanol), effective at stripping PMMA, Chemical Semi Amplified Resist (CSAR) and novolac-based resists. The two-step cleaning procedure was used after graphene transfer as well as after each device fabrication step where PMMA removal was involved, i.e. after graphene etching and metal lift-off. Several attempts were made to find the optimal chemistry and procedure to clean graphene, including the adoption of each single component of AR 600-71. The cleaning efficiency of the attempted approaches was evaluated by spectroscopic and microscopic techniques, with the 2SC approach

detailed above being the most effective. In the following paragraphs we report AFM and spatially-resolved XPS analyses which demonstrate that the 2SC approach is instrumental to rapidly eliminate most of the polymeric residues which remain on graphene after transfer and fabrication and that have adverse effects on its electrical properties. Raman measurements show a significant reduction of graphene doping and strain with high mobility obtained by electrical transport measurements. Electrical measurements ultimately confirm the effectiveness of the reported 2SC procedure demonstrating improved room temperature transport and reduced residual doping.

3.3 AFM analysis: morphological investigation of ultra-clean graphene

AFM was used to evaluate the effectiveness of the developed cleaning method by investigating the surface morphology of graphene after the 1SC and 2SC approaches. Below we report a representative 10 × 10 μm^2 area selected at the border of a graphene single-crystal allowing the analysis of polymer residues on graphene and SiO_2 surface. The topographical images of the selected areas are shown in figure 3.2 (a) and (b) after 1SC and 2SC of graphene, respectively.

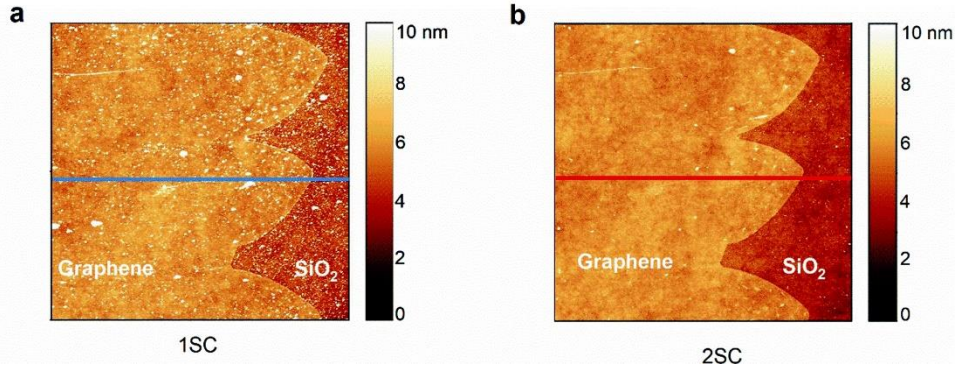

Figure. 3.2 (a) Topography image (10 × 10 μm^2) of graphene crystal edge after transfer to SiO_2/Si and 1SC; (b) The same area after the second cleaning step.

The 1SC protocol leaves nanometer-sized particles on graphene as seen in figure 3.2 (a) and also observed previously.[134] However, when exposed to the second cleaning step, a notable reduction of PMMA contaminants can be observed. Indeed, figure 3.2(b) reveals a flat and homogeneous graphene surface with sporadic wrinkles. When subjected to the one-step cleaning procedure, the height of the surface features of graphene is larger than 5 nm, as shown in figure 3.3, which reports the surface profile measured along the blue line of figure 3.2 (a). While in the case of the two-step cleaning process, the surface features height variation is much less pronounced

as shown in figure 3.3. Indeed, in this case only a limited number of points reach a height of ~2 nm, a size compatible with the surface height variation of the SiO_2 substrate, as can be seen outside of the graphene crystal. Another important information that one can extract from the AFM data is the surface roughness of the sample scanned. In the case of 1SC, the root mean square (RMS) roughness of the graphene-coated area was found to be nearly ~2.8 nm, while for the 2SC was reduced to ~0.6 nm.

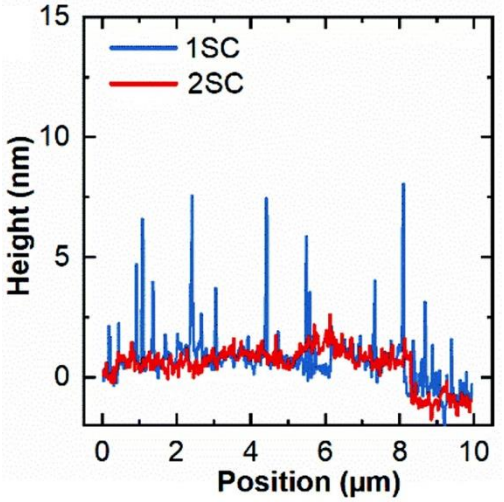

Figure. 3.3 Surface profile of graphene taken from the topographical images after 1SC (blue) and 2SC (red).

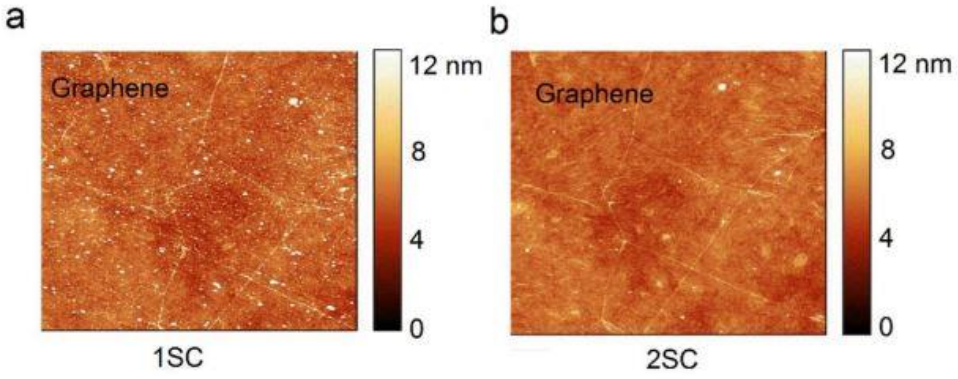

Figure. 3.4 (a) AFM topography image (10×10 μm^2) obtained at the center of a transferred graphene crystal after 1SC; (b) AFM topography image of the same graphene area after 2SC.

The RMS roughness measured after the 2SC approach is nearly matching the intrinsic roughness value of the Si/SiO_2 wafer, which is ~0.5 nm as declared by the supplier and confirmed by AFM measurements prior to graphene deposition. Additional statistics was performed to analyze the number of polymer residues remaining on the graphene surface after the 1SC and 2SC treatments. This particle analysis was performed on a 10 × 10 μm^2 area from the center of a graphene crystal as shown in figure 3.4. The RMS roughness measured on such areas was ~3.3 nm and ~0.8 nm after 1SC and 2SC, respectively, further confirming what measured at the graphene single-crystal edge. The comparison between the height and radius of the polymeric residues after 1SC and 2SC is reported in figure 3.5 (a) and (b), respectively. For 1SC treatment, the total number

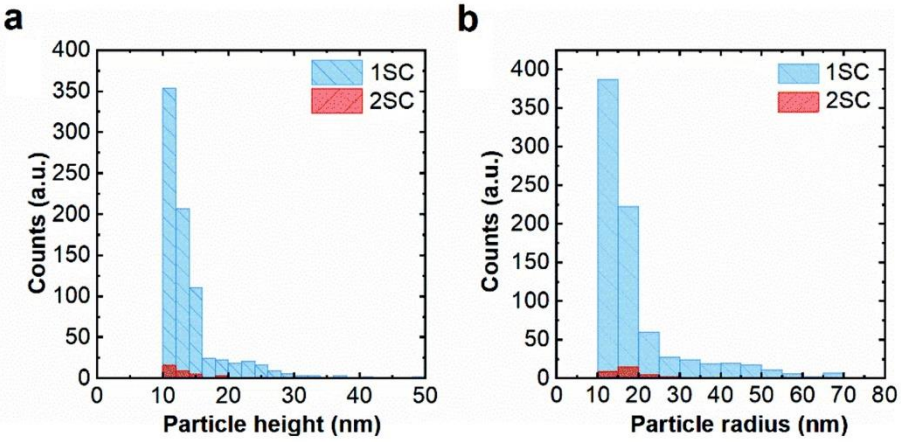

Figure. 3.5 (a) and (b) are depicting the statistical distribution of particle height and radius, respectively, after one-step and two-step cleaning approaches.

of particles was around 810 with an average height of ~14 ± 5 nm. After 2SC, the number of particles and height were reduced to 34 and ~13 ± 3 nm, respectively (see figure 3.5(a)). Similarly, the average radius of polymeric residues on graphene surface was recorded to be around ~19 ± 13 nm after 1SC, while after 2SC it was nearly ~20 ± 14 nm, as described in figure 3.5 (b). These data indicate that more than 95% of surface contaminants are removed when adopting the 2SC approach. We also further tested this approach for wet transferred polycrystalline graphene to show its adaptability for different types of graphene. We found similar results as those obtained for single-crystal graphene transferred onto Si/SiO_2 by using the semi-dry transfer technique. In the case of wet transferred graphene, RMS roughness values were recorded from 3 × 3 μm^2 surface areas showing values of ~ 2.2 nm after 1SC and ~0.7 nm after 2SC, following the same trend of

semi-dry transferred graphene. The AFM measurements after 1SC and 2SC for wet transferred graphene are shown in figure 3.6.

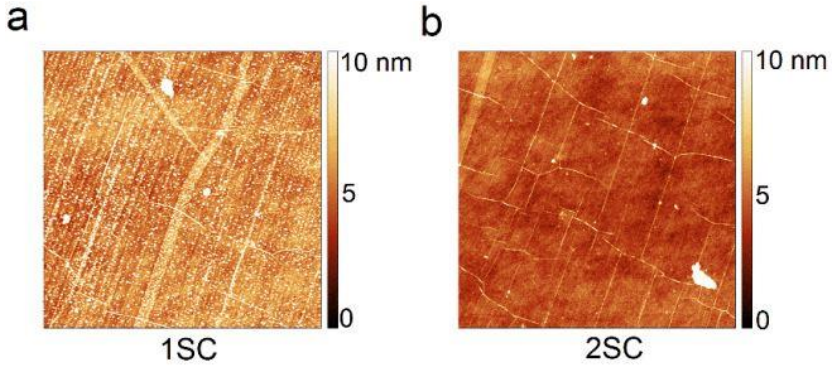

Figure. 3.6 (a) AFM topography image (6×6 μm^2) taken after transferring polycrystalline graphene on SiO_2/Si after 1SC and; (b) 2SC approach.

3.4 Raman analysis: strain and doping of ultra-clean graphene

Raman spectroscopy is a powerful instrument to analyze the properties of graphene such as the amount of doping and strain. For this work, Raman spectroscopy was performed on the graphene samples to evaluate their crystalline quality, doping and strain, after each processing and cleaning step.

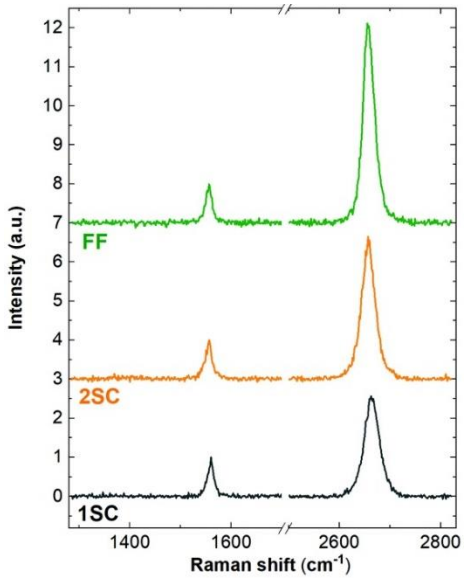

Figure. 3.7 Raman spectra of graphene at various stages of processing: transfer and single-step cleaning, 1SC (black), two-step cleaning, 2SC (orange), full fabrication, FF (green).

In figure 3.7, illustrative Raman spectra obtained after graphene transfer and 1SC (black), 2SC (orange) and full device fabrication (FF) (green) are reported. The full fabrication of graphene device corresponds to the three separate rounds of PMMA deposition followed by 2SC. After 1SC of graphene, the characteristic Raman G and 2D peaks of graphene were found at Pos(G) ~ 1586.5 ± 0.8 cm^{-1} and Pos(2D) ~ 2679 ± 1.4 cm^{-1}, respectively. The average full width at half-maximum (FWHM) of the G and 2D peaks were ~15 ± 1.2 cm^{-1} and ~30.5 ± 1.0 cm^{-1}, respectively. The latter can be

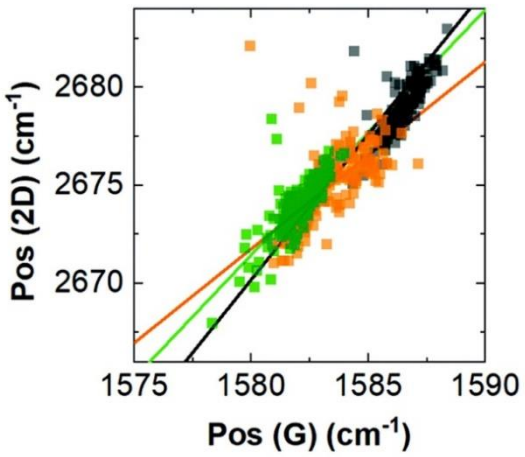

Figure. 3.8 Pos(2D) as a function of Pos(G). Solid lines show linear fits to the three data sets at various stages of processing: transfer and single-step cleaning, 1SC (black), two-step cleaning, 2SC (orange), full fabrication, FF (green).

fitted with a single Lorentzian, as expected for single-layer graphene.[99] No peak associated with defects (D-peak) was observed near 1350 cm^{-1} confirming the negligible number of defects in the CVD graphene grown and transferred with our approaches.[135] To assess doping and strain of the graphene transferred on SiO_2, a correlation plot of the 2D and G peak positions was extracted for a 12 × 12 μm^2 mapped area (see figure 3.8) similar to what reported in [100,103].

The rates of variation of the two peak positions as a function of strain are determined by the Grüneisen parameters [104], and the relative peak shift (ΔPos(2D)/Δpos(G)) is typically observed

to be ~ 2–3 [136]. Furthermore, as indicated by the slope shown by the solid lines in figure 3.8, ΔPos(2D)/ΔPos(G) is ~1.45 after 1SC, ~1.06 after 2SC and ~1.25 after FF, respectively, demonstrating an inhomogeneous distribution of doping and strain. Uniaxial strain presents G-peak splitting [103], which can help to distinguish it from biaxial strain [95], nonetheless for small strain (≲0.5%) the splitting cannot be determined [103,136] and the presence or coexistence of both uniaxial and biaxial strain in our samples cannot be ruled out. Also, the shift of Pos(G) can be used to approximate strain, considering $\Delta Pos(G)/\Delta\varepsilon \sim 23(60)$ $cm^{-1}\%^{-1}$ for uniaxial (biaxial) strain.[103,136] In our samples, the average Pos(G) was measured at ~1586.5 ± 0.8 cm^{-1} after 1SC, ~1583.5 ± 1.2 cm^{-1} after 2SC and ~1581.9 ± 0.6 cm^{-1} after full fabrication, respectively. Considering that unstrained, intrinsic graphene [99,137] is expected to have Pos(G) ~ 1581.5 cm^{-1}, and accounting for the effect of doping [100] which we calculate from the area ratio of the 2D and G peak A_{2D}/A_G (reporte in figure 3.10), we estimate the contribution of strain to ΔPos(G) to be ~1.9 ± 0.9 cm^{-1} after 1SC, ~0.2 ± 0.4 cm^{-1} after 2SC and ~0.3 ± 0.2 cm^{-1} after FF. This corresponds to uniaxial (biaxial) strain of 0.04%(0.02%) to 0.13%(0.05%) after 1SC, −0.01% (0%) to 0.02%(0.01%) after 2SC and 0% to 0.02%(0.01%) after full fabrication, respectively. Moreover, another parameter adopted to analyze strain variation in graphene, is the FWHM of the 2D peak which is sensitive to the strain variation within the area of the laser spot.[138] Indeed, the FWHM of the 2D peak is usually a good indication of the strain inhomogeneity in graphene and thus of its quality on SiO_2 substrates. [107]

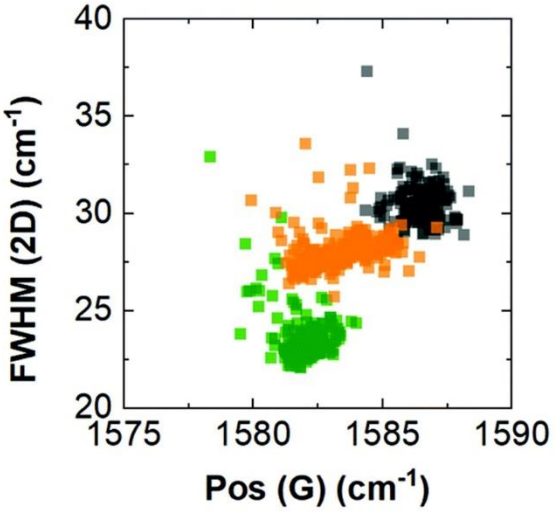

Figure. 3.9 Full width at half maximum FWHM(2D) vs position of G peak at various stages of processing: transfer and single-step cleaning, 1SC (black), two-step cleaning, 2SC (orange), full fabrication, FF (green).

A substantial decrease of the average 2D width is observed upon repeated cleaning: we observe FWHM(2D) going from ~ 30.5 ± 1.0 cm^{-1} after 1SC to ~ 23.6 ± 1.3 cm^{-1} after full fabrication, as shown in figure 3.9. Graphene on SiO_2 typically shows FWHM(2D) values larger than 25 cm^{-1}, even for the case of exfoliated flakes.[107,120] This signifies that our ultra-clean graphene offers extraordinarily low strain fluctuation, which is crucial to achieve high carrier mobility.

Another quantity that can be extracted from the Raman data of graphene is the amount of doping. Doping can be estimated by using the intensity ratio (I_{2D}/I_G) and area ratio A_{2D}/A_G of the graphene Raman peaks. In this work, to estimate the graphene doping, we adapted the approach previously developed by Basko et al.[102] As shown in figure 3.10 (a), the 2D and G peak intensity ratio increases from I_{2D}/I_G ~ 2.8 ± 0.2 after transfer to I_{2D}/I_G ~ 3.1 ± 0.5 after 2SC, ultimately reaching ~ 4.6 ± 0.7 after FF. Also, the peak area ratio after transfer is A_{2D}/A_G ~ 5.7 ± 0.4, increasing to A_{2D}/A_G ~ 6 ± 0.4 after 2SC and A_{2D}/A_G ~ 7.9 ± 0.6 after FF. We use the 2D/G peak area ratio, figure 3.10 (b), to estimate the doping in our samples at various stages of processing. After transfer and 1SC, the doping is estimated to be ~ (2.6 ± 0.5) × 10^{12} cm^{-2}, reducing to ~ (2.2 ± 0.4) × 10^{12} cm^{-2} after 2SC process. After FF, it is further reduced to ~ (1.0 ± 0.3) × 10^{12} cm^{-2}.

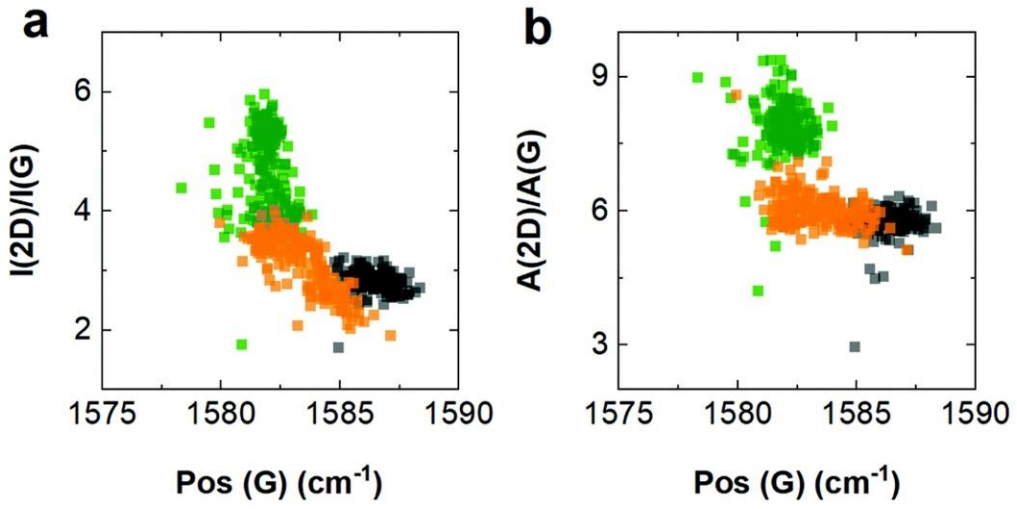

Figure. 3.10 (a) Intensity and (b) area ratio of 2D and G peak of graphene vs position of G peak at various stages of processing: transfer and single-step cleaning, 1SC (black), two-step cleaning, 2SC (orange), full fabrication, FF (green).

To give a clear picture of how the doping is estimated, we account for the dielectric constant ε (SiO_2) = 3.9. We also note that using the electron-phonon scattering rate $\gamma_{e\text{-}ph}$ = 33 meV [92], tends to overestimate the doping in our samples (when comparing Raman and electrical measurements).

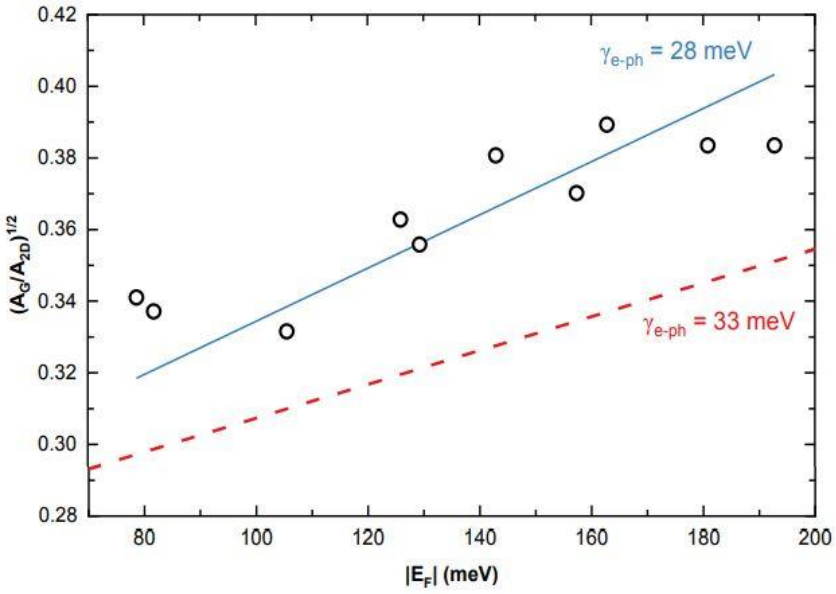

Figure. 3.11 Square root of Raman 2D and G peak area ratio as a function of sample doping obtained from field effect measurements (black circles). Red and blue lines show fits obtained with two different values of $\gamma_{e\text{-}ph}$.

In figure 3.11, we plot the square root of Raman 2D and G peak area ratio as a function of sample doping obtained from measurements of 10 different samples fabricated using 1SC and 2SC processing. As can be seen from the figure, doping dependence in our samples is described much better using γe-ph = 28 meV (blue solid line) instead of $\gamma_{e\text{-}ph}$ = 33 meV (red dashed line).

It should be noted that 2SC is effective not only after graphene transfer but after any of the fabrication steps where PMMA deposition is involved. PMMA deposition and removal with 1SC during any processing step typically leads to a Raman spectrum similar to that of graphene after

transfer, but treating the sample with 2SC always leads to reduced doping and strain inhomogeneity. Interestingly, performing several device fabrication steps using 2SC (i.e., performing several rounds of PMMA resist deposition and its complete removal) leads to an overall improvement of Raman characteristics (reduction of FWHM(2D) and red-shift of Pos(G)) towards values corresponding to pristine graphene[100], compared to as-transferred graphene treated to 2SC. It should be noted that this effect is observed for the first 2 re-depositions of PMMA

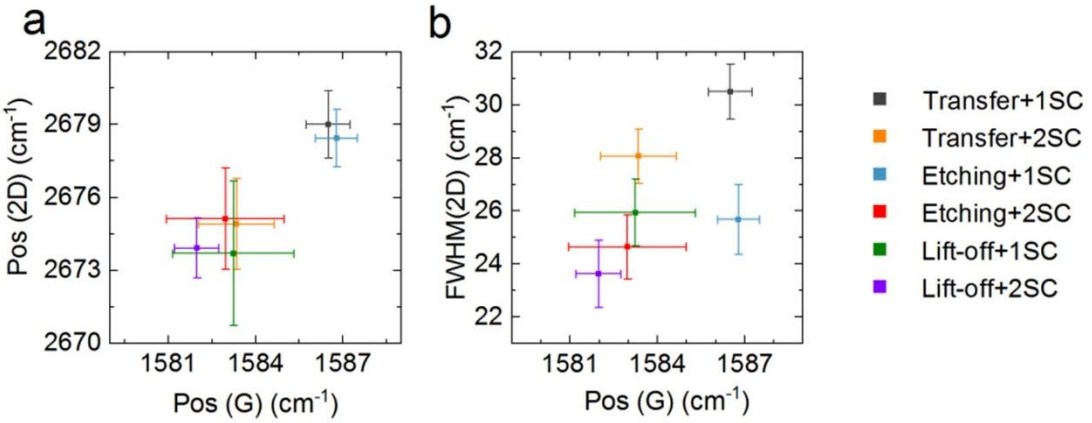

Figure. 3.12 Raman correlation plots after 1SC and 2SC at each transfer/processing step. (a) Pos (2D) as a function of Pos (G); (b) FWHM (2D) as a function of Pos (G).

, after which no improvement is detected. Similarly, treating graphene with AR 600-71 remover beyond the standard 3 minutes does not lead to further improvement. To have a clear understanding of strain and doping during different processing steps involved for graphene device fabrication, a comparison of position of 2D vs G peak of graphene and the FWHM of 2D peak as function of G peak position are depicted in figure 3.12.

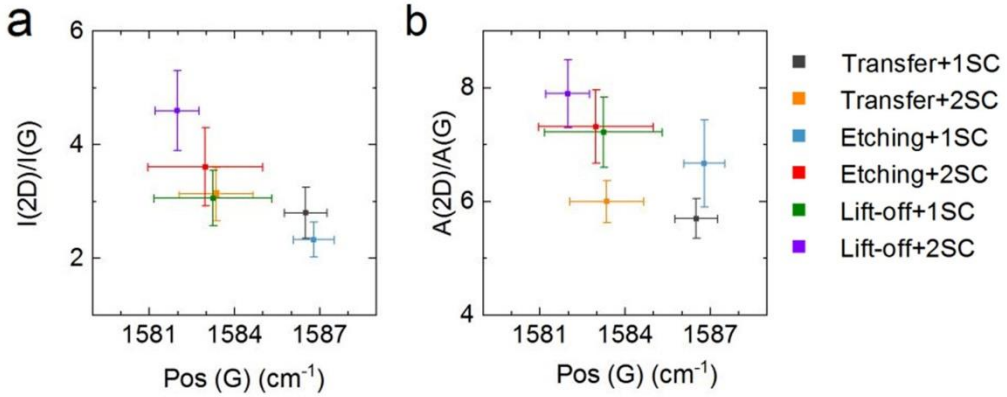

Figure. 3.13 Raman correlation plots after 1SC and 2SC at each transfer/processing step. (a) 2D vs G peak intensity ratio as a function of Pos (G); (b) 2D vs G peak area ratio as a function of Pos (G).

Similar, extracted Raman data useful to compare the doping change during each processing step is shown figure 3.13. These results confirm doping reduction after each 2SC step. All the Raman mapping reported here were performed on the same 12x12 μm^2 graphene area during device fabrication. A Raman map was obtained after each of the 2 cleaning steps following every graphene fabrication procedure (transfer, patterning and metallization). Table 3.1 reports the data plotted in figures 3.12 and 3.13 as average values and respective error bars.

Table 3.1 Average Raman fit Parameters from figures 3.12 and 3.13.

Graphene cleaning stage	Pos (G) (cm^{-1})	Pos (2D) (cm^{-1})	FWHM (2D) (cm^{-1})	I_{2D}/I_G	A_{2D}/A_G
Transfer+1SC	1586.5±0.76	2679±1.38	30.5±1.03	2.8±0.19	5.7±0.35
Transfer+2SC	1583.4±1.29	2674.9±1.8	28.06±1.85	3.13±0.48	6±0.38
Etching +1SC	1586.7±0.72	2678.4±1.18	25.7±1.32	2.3±0.31	6.7±0.77
Etching+2SC	1582.9±0.74	2675.2±1.28	24.6±0.79	3.6±0.42	7.3±0.35
Lift-off+1SC	1583.2±1.34	2673.7±2.34	25.9±1.1	3.1±0.2	7.2±0.34
Lift-off+2SC	1581.9±0.78	2673.9±1.27	23.6±1.28	4.6±0.71	7.9±0.6

The general trend of the data is that after each processing step (i.e., transfer, RIE, metallization) and 1SC cleaning, a blue shift of peak positions and a reduction in 2D/G peak intensity and area ratio is observed, compared to pristine graphene. This indicates increasing doping and strain, though this effect is reversed simply by applying the second cleaning step. 2D width, which is correlated to the nanometric strain fluctuations within the laser spot [107], gradually improves after each step, reaching the lowest value of 23.6 cm^{-1} after metal liftoff and 2SC. This likely indicates that polymer re-deposition releases some of the strain induced in graphene during transfer, without releasing extra contamination due to the effective cleaning by the remover.

As shown in figure 3.14, we find similar results also when applying the 2SC procedure to a standard wet transfer approach of polycrystalline CVD graphene, in agreement with the AFM data shown in figure 3.6.

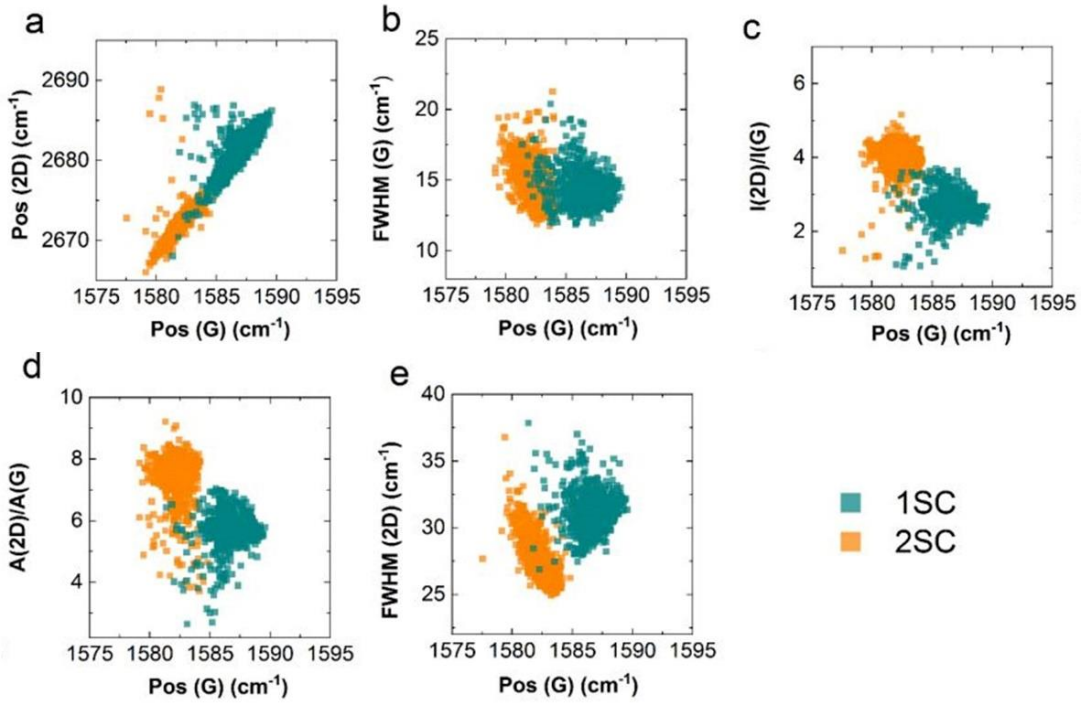

Figure. 3.14. (a) Pos (2D) as a function of Pos (G). (b) FWHM (G) as a function of Pos (G). (c) I_{2D}/I_G ratio with respect to the Pos (G). (d) Area ratio of 2D and G peaks and e) FWHM(2D) as a function of Pos (G) of polycrystalline graphene after 1SC and 2SC.

In conclusion, detailed analysis of Raman data reveals that the 2SC is effective on different types of graphene (i.e., single-crystal and polycrystalline) and after different transfer approaches (i.e., semi-dry and wet) in reducing both doping and strain inhomogeneity: a result consistent with the removal of polymeric residues observed in AFM.

3.5 XPS analysis: chemical mapping of ultra-clean graphene

Chemical analysis performed by XPS is instrumental to better identify any contamination remaining on surfaces. For this purpose, the surface chemical composition of graphene after 1SC and 2SC was examined by X-ray photoelectron spectroscopy (XPS). In order to confine the domains, XPS Parallel Imaging (500 × 500 μm^2) was used. From the C 1s map recorded at 284.5

eV, a 60 µm large area in the middle of a graphene flake was isolated and analyzed by selected Small-area XPS (SAXPS). Here, figure 3.15 shows the C 1s SAXPS spectrum (292–282 eV) recorded on a graphene crystal for 1SC (blue) and 2SC (red) samples.

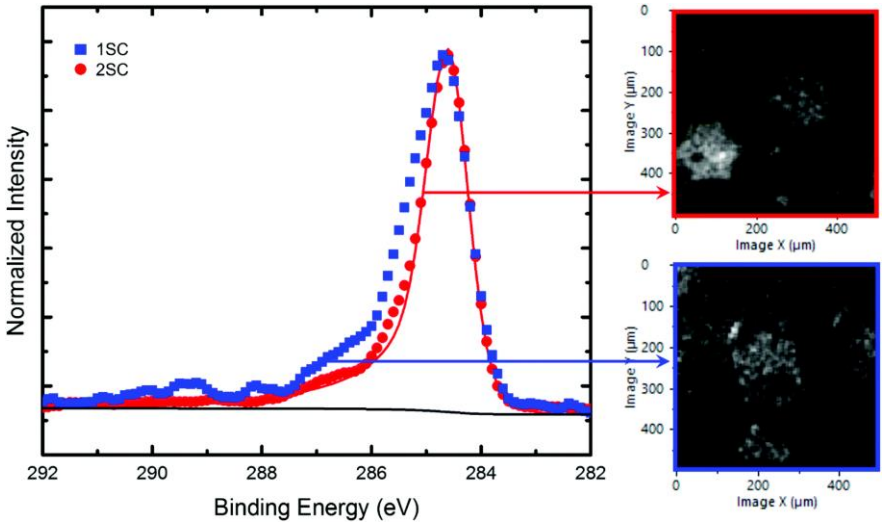

Figure. 3.15. C 1s SAXPS spectra recorded on 60 µm large area of graphene for samples after 1SC (blue) and 2SC (red). Positions were determined thanks to parallel XPS Imaging (500 × 500 µm2) at 284.5 eV. In the spectra, the red and blue symbols represent the experimental data and the red straight line is related to the fit of a graphene component with an asymmetric shape.

The red continuous line measured after 2SC features a broad asymmetric tail towards higher binding energy mimicking a pure sp^2-hybridized C–C component (graphene), while the blue line measured after 1SC indicates the presence of components at higher energies linked to PMMA residues.[134] Hence, XPS analysis by suggesting a clear reduction of these spectral components after the second cleaning step, indicates its effectiveness in lessening PMMA residues. Also, the effect of the remover is also noticeable on the C 1s XPS maps, which demonstrates better-defined flakes after 2SC. In fact, on the C 1s image obtained after 1SC, PMMA residues remain on both the SiO_2 substrate and on the graphene crystals, accordingly yielding a less-contrasted image. In order to ensure that contrasts are primarily related to chemical differences, figure 3.16 shows C 1s and Si 2p XPS mapping in the same zone. The opposite contrasts detected in the maps specify that the observed differences are not governed by topographic effects. Ultimately, the chemical analysis further supports what already observed in AFM.

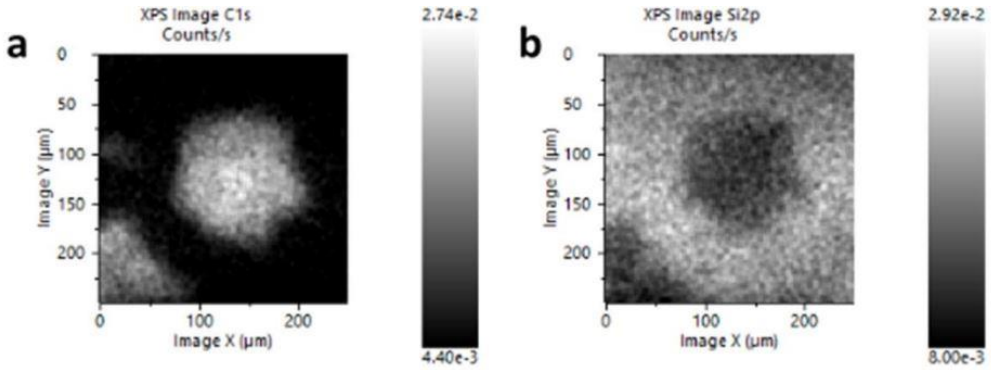

Figure. 3.16. Parallel XPS Imaging of a graphene crystal after transfer to SiO_2/Si and 2SC measured at binding energies of (a) 284.5 eV and (b) 102.5 eV.

3.6 Electrical properties of ultra-clean graphene

After having investigated the effect of the 2SC approach on our CVD graphene by Raman and XPS, we moved to studying the electrical performance of the graphene devices treated with the newly developed approach. To this end, two sets of back-gated Hall-bars (HBs) were fabricated by using electron

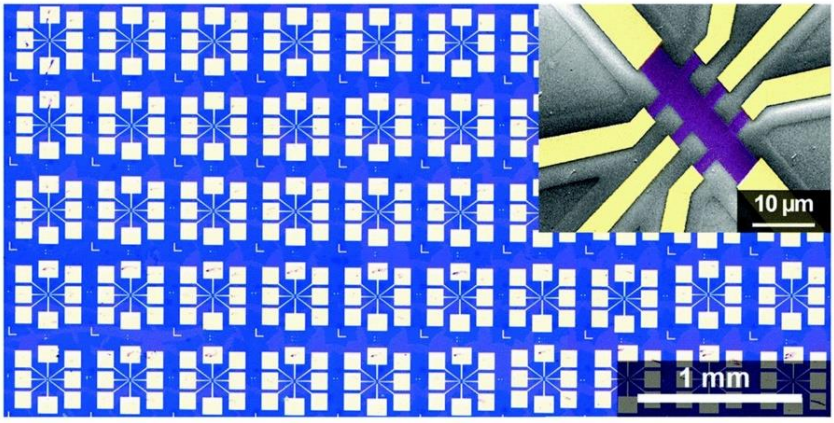

Figure 3.17. (a) Optical image of 50 graphene Hall bars on SiO_2/Si. Inset: false-color SEM image of a single Hall bar.

beam lithography (EBL) on matrixes of single-crystal graphene. One of the fabricated chips containing 50 different devices, shown in figure 3.17, was processed using 2SC after transfer and during individual lithography steps, whereas the reference chip was fabricated by using 1SC at each step. Additionally, the field effect response of each HB with the channel aspect ratio L/W =

1 was measured as a function of the applied back-gate voltage using a 4-probe setup, while applying a source-drain current I_{SD} = 1 μA between the longitudinal contacts and measuring the voltage drop V_{XX} along 2 adjacent side contacts. A schematic of the measurement configuration is shown in figure 3.18.

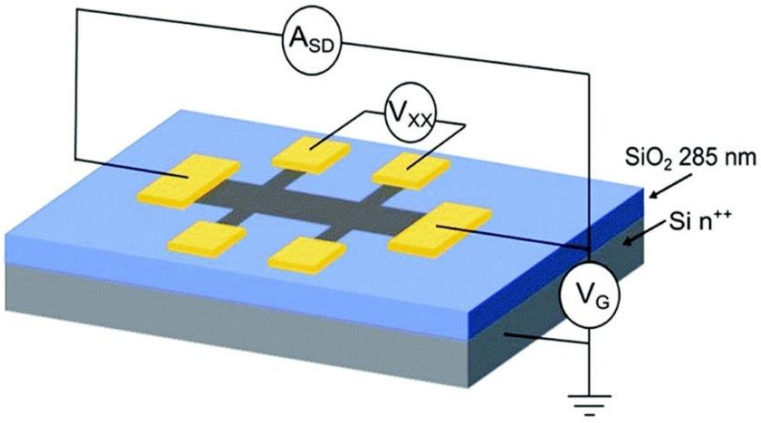

Figure 3.18. Schematic diagram of the 4-terminal electrical characterization setup.

Furthermore, the resistance of the graphene device was calculated as $R = V_{XX}/I_{SD}$. Also, the carrier mobility was calculated for each device as a function of carrier density n (obtained from the applied back-gate bias) using the Drude formula:

$$\mu = 1/(neR) \qquad \text{Eq. 3.1}$$

where e is the electronic charge. Figure 3.19 (a), demonstrates the field effect curve obtained for best performing Hall Bar (HB-27) on the 2SC chip, with the resulting carrier mobility as a function of n depicted in figure 3.19 (b). Hole and electron mobility values at technologically-relevant carrier density of 1×10^{12} cm^{-2} [120], are designated on the curve in figure 3.19 (b). On average, the CNP was measured at ~14.9 ± 2.0 V. The CNP value clearly indicates p-type doping ~ $(1.0 \pm 0.1) \times 10^{12}$ cm^{-2}, which is typical for high-quality non-encapsulated graphene measured in ambient conditions due to atmospheric adsorbates. [139] Lower doping can be obtained by either encapsulating the graphene[140], or performing electrical characterization in vacuum. [139]

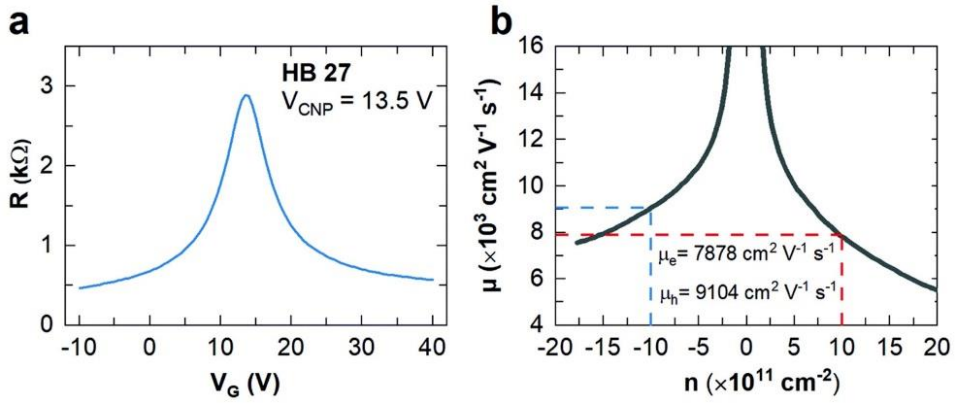

Figure 3.19. (a) Resistance curve of HB27 prepared with 2SC; (b) Carrier mobility as a function of carrier density calculated from the measurement in (a).

Also, the residual charge density at charge neutrality point (CNP), n*, was obtained for each device from a linear fit of conductivity on a double-logarithmic scale, as shown in figure 3.20 for HB27. The residual carrier density of graphene is also a very important factor and should be considered carefully when designing high mobility graphene field effect devices. [141]

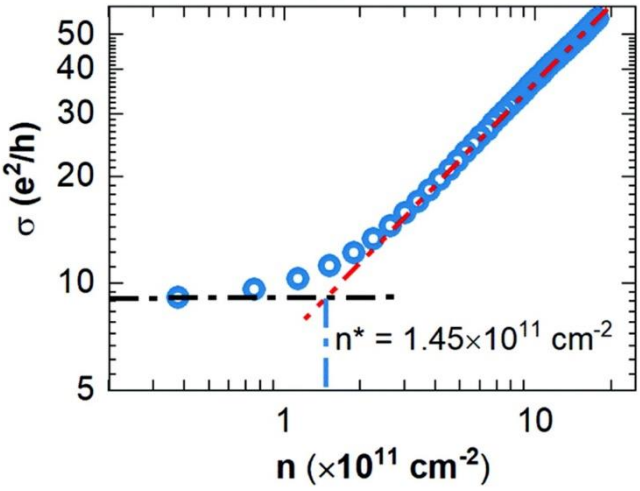

Figure 3.20. Residual carrier density plot of HB27 prepared with two step cleaning approach.

The average values of mobility for HBs fabricated using 2SC were μ_h ~7460 ± 698 $cm^2\ V^{-1}\ s^{-1}$ and μ_e ~6294 ± 781 $cm^2\ V^{-1}\ s^{-1}$ and the residual carrier density was n* ~ (1.7 ± 0.3) × 10^{11} cm^{-2}. Interestingly, the high μ and low n* values are consistent with the low FWHM(2D) observed in the Raman measurements, confirming the ultraclean and high-quality graphene. Notably, the best

performing device (HB-27) presented $\mu_h \sim 9104$ cm^2 V^{-1} s^{-1} and $\mu_e \sim 7877$ cm^2 V^{-1} s^{-1} and n* ~ 1.4×10^{11} cm^{-2}.

In the case of 1SC, the average values of mobility and residual carrier density were $\mu_h \sim 4562 \pm 1000$ cm^2 V^{-1} s^{-1}, $\mu_e \sim 4311 \pm 983$ cm^2 V^{-1} s^{-1} and n* ~ $(2.9 \pm 0.4) \times 10^{11}$ cm^{-2}. Figure 3.21 (a) is depicting a comparison of graphene devices fabricated with 1SC and 2SC in terms of mobility calculated as a function of charge carrier density. A histogram of the carrier mobility of graphene devices fabricated with both 1SC and 2SC techniques, is also presented in the figure 3.21 (b).

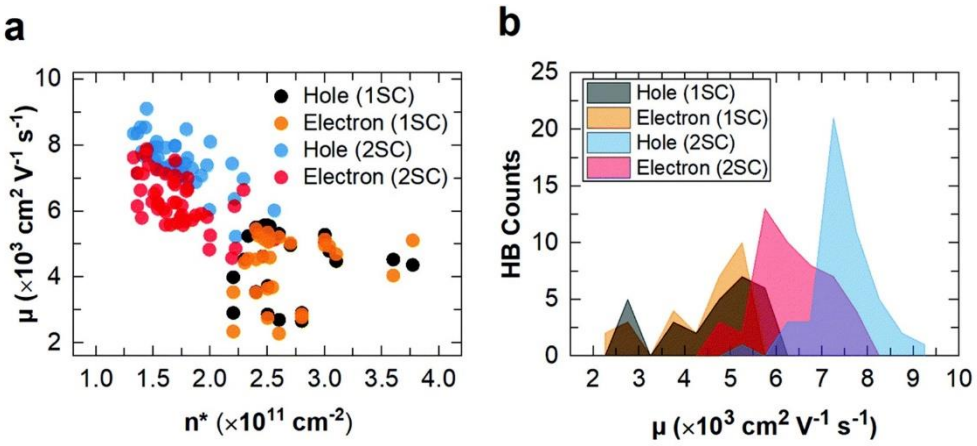

Figure 3.21. (a) Mobility statistics of all graphene Hall bars prepared with 1SC (black, orange) and 2SC (red, blue) as a function of n*; (b) Histogram of electron and hole mobility measured in chips fabricated using 1SC and 2SC.

Thus, the electrical comparison strongly correlates with the Raman, AFM and XPS data suggesting the advantage of 2SC over 1SC approach. Furthermore, to verify the advantage of using the 2SC approach in graphene processing, we used the 2SC method to fabricate three other chips (in addition to the sample shown in figure 3.17) with smaller amount of test structures (5–8 Hall bars), all showing consistently high carrier mobility values ($\mu_h > 7500$ cm^2 V^{-1} s^{-1}, $\mu_e > 6300$ cm^2 V^{-1} s^{-1}), as shown in figure 3.22. The significantly enhanced mobility values of 2SC devices designate the fact that effective removal of polymer (PMMA) residues lessens the charge-carrier scattering and unintentional doping in graphene.[142,143] This clearly demonstrates that 2SC enables graphene transfer and processing on a large scale with high mobility and low carrier density

suitable for the fabrication of functional devices, such as magnetic sensors [9,119], optoelectronic modulators and photodetectors for high-speed telecommunications.[78]

3.7 Conclusions

An effective and rapid two-step cleaning (2SC) method to reduce the polymeric (PMMA) residues present on graphene surface after transfer and lithography processing is demonstrated. In this way, enhanced mobility can be achieved for CVD graphene on SiO_2/Si substrates. AFM surface topography measurements and spatially-resolved XPS evidently illustrate the effectiveness of this approach in removing PMMA residues, for both single-crystal graphene transferred with semi-dry transfer and polycrystalline graphene prepared with wet etching transfer method. This makes the method presented here a relevant technique for preparing high-quality graphene for various kind of applications. A thorough analysis of Raman maps indicates the reduction of graphene doping after 2SC, while the absence of Raman D peak confirms that no structural defects are introduced in graphene. Electrical measurements show a significant improvement of the carrier mobility and residual charge carrier density with respect to the chips processed using the traditional fabrication procedure. The 2SC approach does not introduce defects and yields high cleanliness while being scalable, rapid and easy to perform, with a great improvement over the existing approaches such as thermal annealing, scanning probe cleaning, and polymer-free fabrication (stencil mask lithography). Hence, it provides a straightforward path for the achievement of ultra-clean high-mobility scalable graphene devices which are sought after by several applications.

Chapter 4

Highly Sensitive CVD Graphene Hall Sensors

This chapter discusses on the potential of CVD graphene for scalable Hall sensing applications. Fast magnetic field detection with stable performance is a potential technology area for graphene due to its high carrier mobility and low residual carrier density. Our scalable CVD graphene, thanks to the optimized growth, transfer and cleaning approaches - has demonstrated to yield state-of-the-art values of carrier mobility and very low residual carrier density which would therefore be instrumental to demonstrate high performance Hall sensors. Once fabricated, protecting the graphene-based Hall sensors via a capping strategy would add air stability and might be an aid to lessen the hysteric behavior. In this chapter, we demonstrate scalable high performance graphene Hall sensors and investigate the effect of a PMMA capping layer on the stability, hysteresis, as well as the sensitivities of the devices. State-of-the-art performance of the realized devices, based on scalable synthesis and encapsulation, might contribute to the proliferation of graphene-based Hall sensors.

4.1 Graphene as a Hall sensor

The demand of magnetic field sensors is firmly growing particularly in the automotive and consumer electronics sectors, where they are used in the form of Hall effect sensors.[80,144] To date, silicon-based Hall sensors are dominating in most applications thanks to well-developed silicon complementary metal-oxide-semiconductor (CMOS) technology and low fabrication costs. However, the room temperature (RT) current sensitivity S_I of silicon Hall sensors is typically limited to $\sim$100 V A^{-1} T^{-1}, [145] which restricts their applicability. Higher sensitivity can be obtained when using III–V semiconductor materials, [145] which, however, imply higher fabrication costs. An alternative to these materials could be graphene because of its cost and extraordinary electrical properties. [146,147] Indeed, due to its zero-bandgap nature, the use of graphene is limited in several electronic devices where a bandgap is required, yet in the case of Hall sensor where this is not needed, graphene is expected to outperform conventional materials such as silicon. Graphene, thanks to its ability to achieve extremely low carrier densities and exceptional mobility, [146,147] has emerged as an appealing material for the development of highly sensitive cost-effective Hall sensors that are compatible with the existing CMOS platforms.

To date, the best-performing graphene Hall sensors have been realized using mechanically exfoliated graphene flakes encapsulated with exfoliated hexagonal boron nitride (hBN), reaching a current-related sensitivity (S_I) of ∼5700 V A^{-1} T^{-1}. [148] Hall sensors based on ultraclean exfoliated graphene/hBN stacks were also studied at cryogenic temperatures. [149] RT measurements (presented in the Supporting Information of ref [149]) indicate high S_I ∼ 8000 V A^{-1} T^{-1} in these devices. Indeed, hBN encapsulation is a key ingredient for the realization of highly performing graphene-based devices because it protects graphene from contaminants and ensures the achievement of record carrier mobility. [150] Exposure of graphene-based Hall sensors to air leads to decreasing S_I over time due to the physical adsorption of oxygen or water molecules. [139] Devices based on exfoliated flakes of graphene and hBN, such as the one presented in ref [148], demonstrate high performance, but this approach cannot be considered for industrial production because the size of the exfoliated flakes is typically limited to tens of microns. This issue has been addressed using graphene synthesized via chemical vapor deposition (CVD) on Cu, which has been produced on a wafer scale and can be successfully integrated into semiconductor processing lines. [151] To date, Hall sensors based on CVD graphene have shown S_I ∼ 1200 V A^{-1} T^{-1} [152] and remarkable magnetic resolution. [153] Scalable encapsulation of graphene, however, remains a challenge to be solved. Graphene Hall sensors with CVD hBN encapsulation have shown lowered sensitivity (i.e., S_I ∼ 97 V A^{-1} T^{-1}), [144] although more promising results (i.e., S_I ∼ 1986 V A^{-1} T^{-1}) have been obtained when using CVD hBN as a substrate below the graphene layer. [154] Although graphene Hall elements (GHEs) display enticing prospects, the demonstration of graphene-based magnetic probes that are both highly sensitive and stable over time, while being scalable, is currently lacking.

In this chapter, we demonstrate a facile and systematic approach to achieve high-sensitivity and scalable graphene Hall sensors directly on technologically relevant substrate SiO_2/Si, whose performance over time can be stabilized using a polymeric encapsulation. Scalability is ensured by the adoption of graphene single-crystal arrays grown via CVD (see figure 4.1a), which can be used for wafer-scale integration in several applications. The fabricated Hall sensors demonstrate carrier mobility exceeding 10^4 cm^2 V^{-1} s^{-1} and low charge inhomogeneity at the charge neutrality point (CNP) n* ∼1x10^{11} cm^{-2}. The devices have high current-related sensitivity with S_I up to 5030 $VA^{-1}T^{-1}$. Until now, similar values have been reported only in samples encapsulated with exfoliated hBN, which is not an approach compatible with scalable integration. We also investigate

the air-stability of graphene Hall sensors without encapsulation over a time of 10 weeks and find a significant degradation in the observed performance. To address this issue, we demonstrate a scalable encapsulation with a polymeric protective layer, poly (methyl methacrylate) (PMMA). PMMA was used as an encapsulant for graphene Hall sensing devices. The environmental doping effect on the performance of graphene Hall sensors is studied by electrical transport measurements with and without the presence of magnetic field. PMMA-capped graphene Hall sensors display reduced performance degradation, such as reduced hysteresis and doping. The scalable and facile approach presented in this work can open a realistic path to the fabrication of highly sensitive and air-stable CVD graphene Hall sensors.

4.2 Experimental results

4.2.1 Hall sensing device fabrication process

In order to fabricate the graphene Hall sensing devices, single-crystal CVD graphene matrixes grown on Cu [60], were initially transferred on Si/SiO_2 substrates by using the semi-dry transfer approach described in Pargraph 2.2 (see figures 4.1 (a), (b) and (e)).[94] After transfer, the graphene was cleaned by using the 2SC approach described in chapter 3.[155] For the device fabrication, EBL and RIE were used to define the Hall bar geometry (see figures 4.1(c) and (f)). Specifically, RIE was performed with oxygen (O_2) and argon (Ar) plasma with a gas flow of 5/80 sccm. Afterwards, bimetallic electrical contacts (Cr: 5 nm, Au: 50 nm) were deposited by thermal evaporation. The length of the device channel was kept at 25 µm while the width was 5 µm (see figures 4.1(f) and (g)).

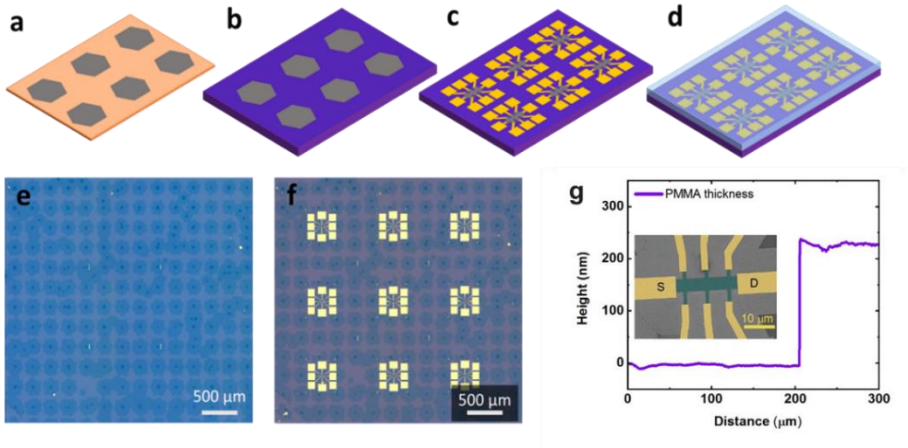

Figure 4.1. Schematic drawing of a typical array of graphene single-crystals a) grown via CVD on Cu foil, b) transferred to Si/SiO_2, c) with fabricated Hall sensors, d) after PMMA spin-coating. e)

Optical micrograph of graphene crystal array transferred on a Si/SiO_2 substrate. f) Hall bars fabricated on the graphene crystal array. g) Thickness evaluation by profilometry of PMMA used as a capping layer for graphene Hall sensor; SEM image of fabricated device in inset.

In the case of PMMA coating, a 240 nm thick PMMA (AR-P672.045 Allresist GMBH) layer was spin coated on graphene Hall sensors with 4000 rpm for 60s and baked at 160°C for 15 minutes (see figures 4.1(d) and (g)). The thickness of PMMA was assessed by profilometry.

4.2.2 Structural analysis by Raman spectroscopy

Raman spectroscopy was performed on the samples to assess the layer number, crystallinity, and doping of graphene before and after PMMA deposition. Raman maps were obtained on the graphene crystals near the Hall bars. Figure 4.2 shows representative Raman spectra obtained before (black curve) and after (red curve) PMMA deposition.

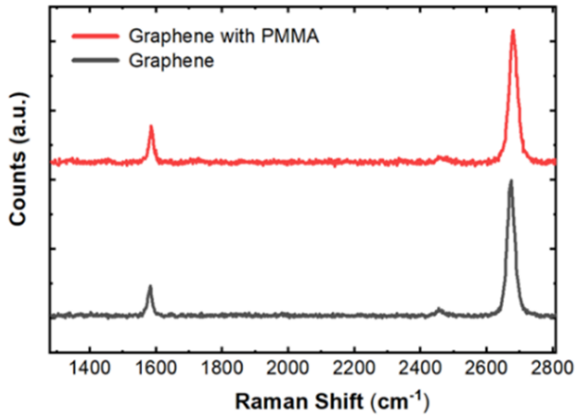

Figure 4.2. Representative Raman spectra of bare graphene (bottom) and PMMA-capped graphene (top).

The spectra show 2 prominent Raman peaks (G peak and 2D peak), which can be fit with a single Lorentzian function, corresponding to single-layer graphene. Before PMMA deposition, the average peak position is found at 1581.5 ± 0.9 cm^{-1} (G peak) and ~2673±1.8 cm^{-1} (2D peak). The full-width-at-half-maximum (FWHM) values are FWHM(G) ~15.3±1.2 cm^{-1} and FWHM(2D) ~25.5±1.5 cm^{-1}. The D peak, typically observed near 1350 cm^{-1} in defective graphene, [131] is absent, indicating high crystalline quality of our material. The 2D/G peak intensity ratio I_{2D}/I_G is ~ 4.7±0.6 and the area ratio A_{2D}/A_G is ~7.8±1, both indicating doping ~10^{12} cm^{-2}. [109] After PMMA deposition, the average positions of both peaks are blue shifted to Pos (G) ~1583.9±1 cm^{-}

[1] and Pos (2D) ~2679.0±2 cm^{-1}. The other fitting parameters show a small change (less than the standard deviation), FWHM(G) ~15.0±1.3 cm^{-1}, FWHM (2D) ~25.6±1.2 cm^{-1}, I_{2D}/I_G ~4.8±0.6, A_{2D}/A_G ~8.2±1. This indicates that polymer deposition has a very small effect on doping or submicron-scale strain variation of the sample, and we can attribute the change of peak positions [99] to a small increase of overall uniaxial (biaxial) strain by ~0.1% (0.05%). Full Raman peak correlation data is presented in the figure 4.3.

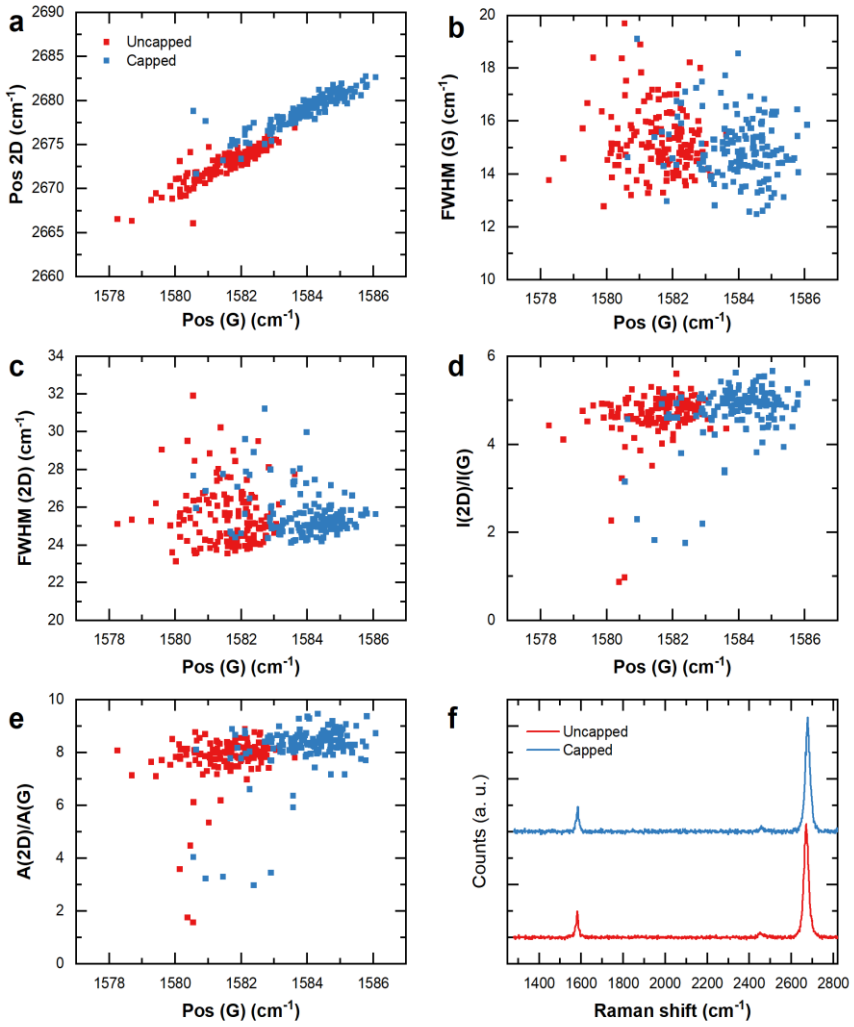

Figure 4.3. (a-e) Raman G peak and 2D peak scattering as a function of G peak position for uncapped graphene (red data points) and capped graphene (blue data points). (a) 2D peak position, (b) G peak width, (c) 2D peak width, (d) Intensity ratio of 2D peak and G peak, (e) Area ratio of

2D peak and G peak. f) representative Raman spectra for uncapped graphene (red) and capped graphene (blue).

4.2.3 Electrical and magnetic response measurements

Thanks to the scalable nature of our graphene, which allows for wafer scale fabrication of devices [94],we defined several Hall bars (see figure 4.1). The set of 9 Hall bars (HB1-HB9) fabricated on Chip 1 and shown in figure 4.1(f) were fully characterized electrically. Electrical transport characteristics of the 9 Hall bars, plotted in figure 4.4 (a), were determined by performing field effect measurements in ambient conditions. As shown schematically in figure 4.4 (a), source-drain current I_{SD} = 1 µA was applied along the channel, while sweeping the back gate voltage VG and measuring the longitudinal voltage V_{XX}. Sample resistivity R_{XX}, shown in figure 4.4 (b), was determined using the relation $R_{XX} = V_{XX}/I_{SD}$. As-fabricated, the charge neutrality point VCNP of the devices was found to be near gate voltage VG ~13 V, corresponding to low p-type doping $\sim 1\times10^{12}$ cm^{-2}.

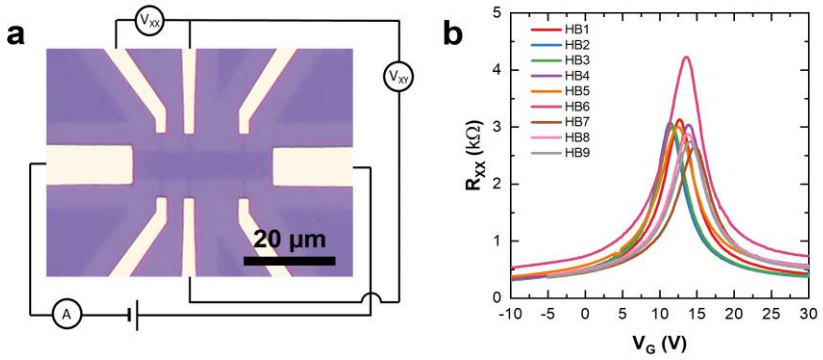

Figure 4.4. (a) Electrical diagram of a typical transport measurement. (b) Resistivity as a function of applied gate voltage. Different colours represent 9 different Hall bars.

The response of our devices to magnetic field was also measured to investigate their potential use as Hall sensors. Using a permanent magnet, a fixed perpendicular magnetic field B ~0.37 T was applied to the Hall bars, while passing constant current of 1 µA. Hall voltage V_{XY} as a function of applied back gate voltage was measured and is shown in figure 4.5 (a). Carrier mobility µ, shown in figure 4.5 (b), was determined using the Drude formula $\mu = 1/(\rho\, n\, e)$, where ρ is the sample

resistivity, equal to R_{XX} due to the square geometry of the channel, n is the gate-induced carrier density, determined from gate capacitance and e = 1.6×10^{-19} C, which is the elementary charge.

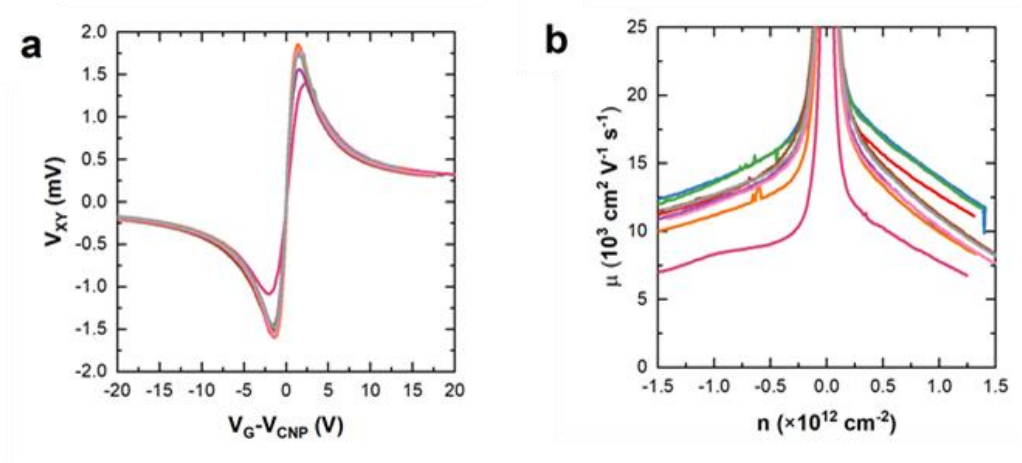

Figure 4.5. (a) Hall voltage as a function of gate voltage applied with respect to the CNP. (b) Carrier mobility as a function of carrier density.

Carrier mobility μ values were estimated at a technologically relevant carrier density n = 1×10^{12} cm^{-2}. Average μ was found to be ~$(1.2\pm0.1)\times10^4$ cm^{2}V^{-1}s^{-1}, with HB2 showing μ as high as ~1.4×10^4 cm^{2}V^{-1}s^{-1}.

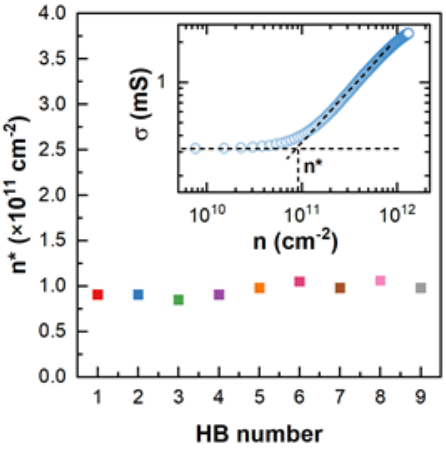

Figure 4.6. Showing the residual carrier density at the CNP, which was determined from a linear fit of conductivity as a function of carrier density on a logarithmic scale. Inset of figure 4.6 shows an example of the fit for HB2.

Full n* fitting data is shown in the supplementary figure 4.7. The average value for the 9 devices was found to be n* ~$(9.5\pm0.5)\times10^{10}$ cm^{-2}.

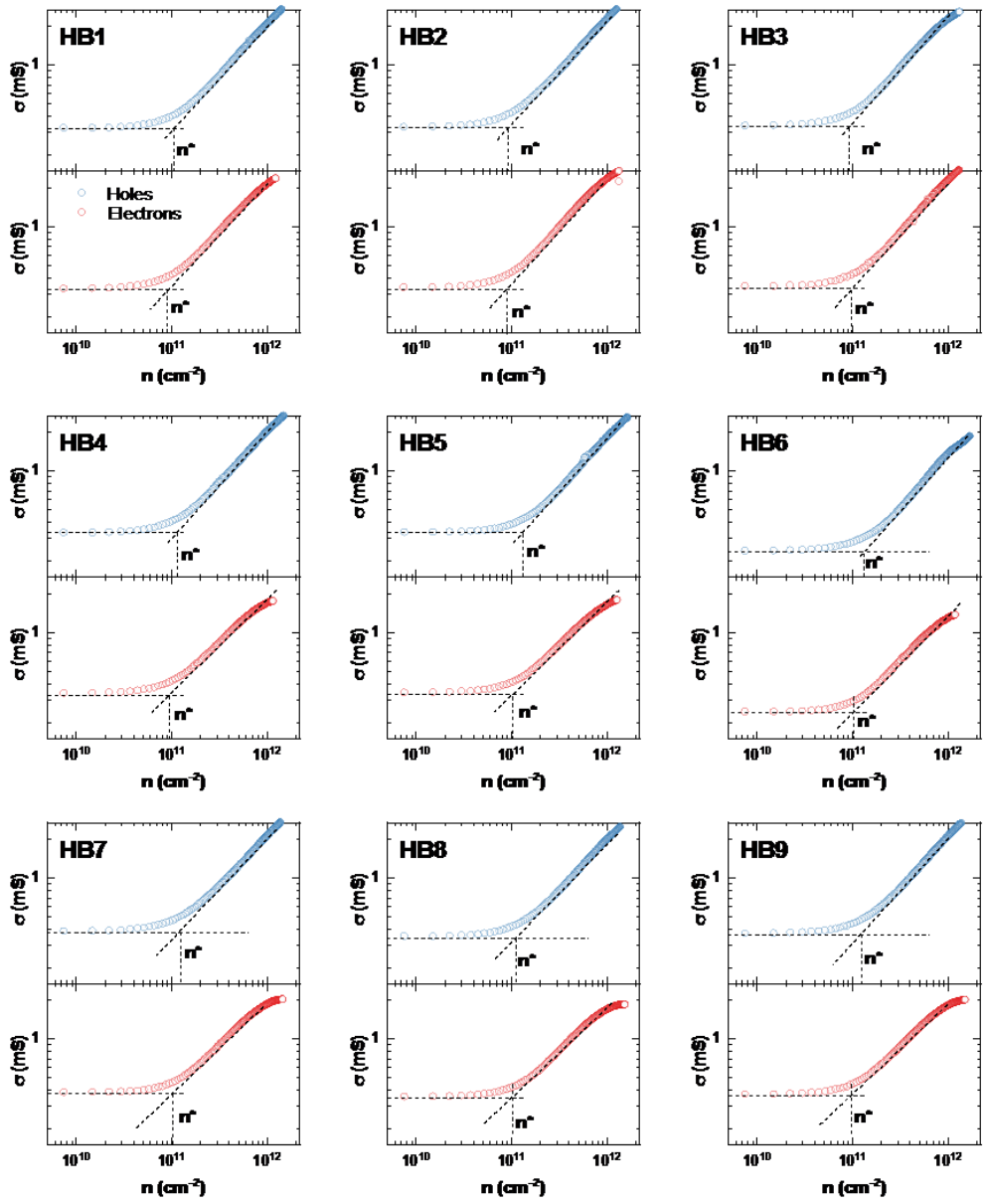

Figure 4.7. n* estimation for the 9 Hall bars of Chip 1 via linear fit of conductivity as a function of carrier density on a double logarithmic scale.

We also estimate the current-related sensitivity S_I of our graphene Hall sensors, which is calculated using the following equation: $S_I = V_{XY}/(IB)$, at a constant current I = 1 μA and magnetic field B = 0.37 T perpendicular to the channel. [156] The average S_I was estimated to be S_I ~4642±392 V A^{-}

$^{1}T^{-1}$, with HB5 showing S_I ~5030 V $A^{-1}T^{-1}$. The high V_{XY} and S_I values measured in our devices are thanks to high carrier mobility and the remarkably low n* (for CVD graphene on SiO_2), which allows us to reach low single-type carrier density in the vicinity of the CNP, a well-known pre-requisite for high Hall coefficient. [9,119] Indeed, as can be seen in supplementary figure 4.7, we observed slight differences in the n* values estimated on the hole and electron branches of the field effect curves of some devices, which agree well with small V_{XY} asymmetry measured in the corresponding Hall bars. To the best of our knowledge, this array of devices demonstrate the highest S_I measured in Hall sensors based on CVD graphene [152,157] , and is approaching the sensitivity observed in Hall sensors based on exfoliated graphene with hBN encapsulation. [148,158] As-fabricated devices show a small spread in resistivity (figure 4.4 (b)), Hall voltage (figure 4.5(a)) and current-related sensitivity figure 4.8. The measured variation of VCNP and other figures of merit between the devices is likely caused by the atmospheric adsorption during device characterization. Indeed, it is well known that electrical performance of bare graphene-based devices measured in ambient conditions can be strongly affected by atmospheric adsorbents. [143]

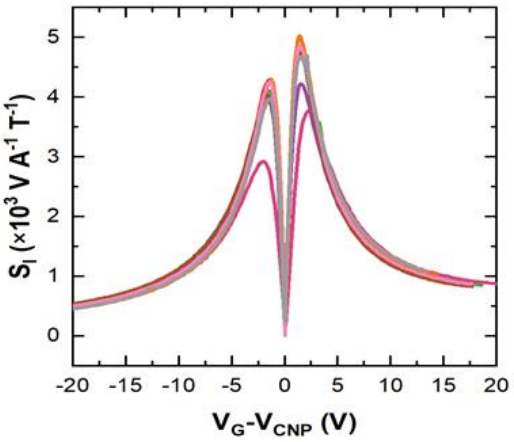

Figure 4.8. Current-related sensitivity as a function of applied gate voltage obtained at B ~0.37 T.

To further study the device stability in ambient conditions, we have fabricated 2 other chips (Chip 2 and Chip 3) with arrays of graphene Hall bars. Both chips were characterized initially, to verify their quality, obtaining average carrier mobility ~10^4 cm^2 V^{-1} s^{-1} in each case. Chip 3 was then capped with a thin (~240 nm) layer of PMMA via spin coating, as described in section 4.2.1. In

figure 4.9, we compare the hysteresis of field effect measurements on uncapped and capped graphene. Top panel shows the field effect measured in chip 2 (uncapped). Sweeping the back gate voltage from -10 V to +30 V (red solid curve), we measure VCNP ~9.5 V, while on the back sweep (orange dashed curve), VCNP is shifted to ~15.8 V, with a hysteresis ΔV ~6.3 V. In the bottom panel, we show the measurements obtained on chip 3 (capped). On the forward sweep (-10 V to 30 V, blue solid curve), we measure VCNP ~10 V, while sweeping back to 0 V (green dashed curve), we measure VCNP ~10.9 V, which indicates a strongly reduced effect of atmospheric adsorbents on the electrical characteristics of this device.

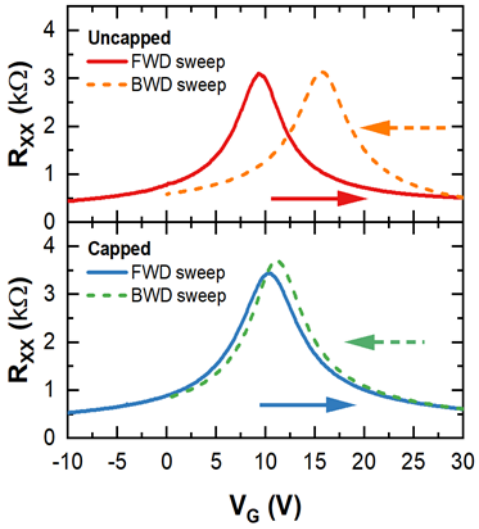

Figure 4.9. (a) Hysteresis of resistivity measurements as a function of applied gate voltage. Top: uncapped Hall bar - Forward (red solid) and backward (orange dashed) back gate sweeps. Bottom: PMMA-capped Hall bar – forward (blue solid) and backward (green dashed) back gate sweeps.

Chips 2 and 3 were then stored in ambient conditions (temperature ~25 °C, relative humidity ~50%) for 10 weeks. To study the trend of aging, we have performed field effect measurements at 2 intermediate time periods, i.e. after 2 weeks and 4 weeks. Figure 4.10 shows the average VCNP obtained for Chip 2 (uncapped, red) and Chip 3 (capped, blue) at various stages of aging. For uncapped chip, there is a strong shift of VCNP over time, reaching average VCNP ~30.6±2 V after 2 weeks, 38.5 V after 4 weeks and ~65±15 V after 10 weeks. There is also pronounced hysteresis in this chip (shown in figure 3c, red), ΔV ~16.5±9 V after 2 weeks and ΔV ~35±20.5 V after 10 weeks. The strong increase in p-type doping, high hysteresis and pronounced device-

to-device variation indicate that uncapped graphene is strongly susceptible to atmospheric adsorbents, making repeated measurements hardly reproducible.

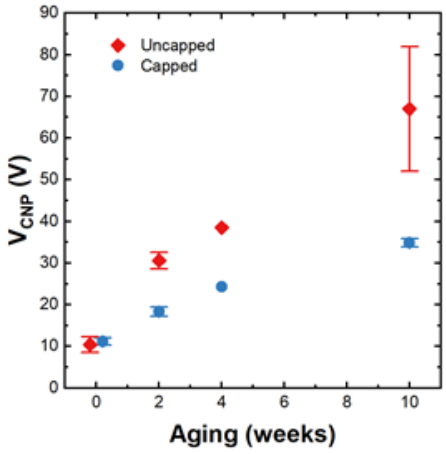

Figure 4.10. position of CNP of uncapped (red) and capped (blue) graphene devices as a function of aging time.

This behavior can also be seen in figure 4.11 (a), where continuous shift of VCNP is seen over repeated back gate sweeps. In contrast, in PMMA-capped sample, repeated gate sweeping has little effect on VCNP position 4.11 (b).

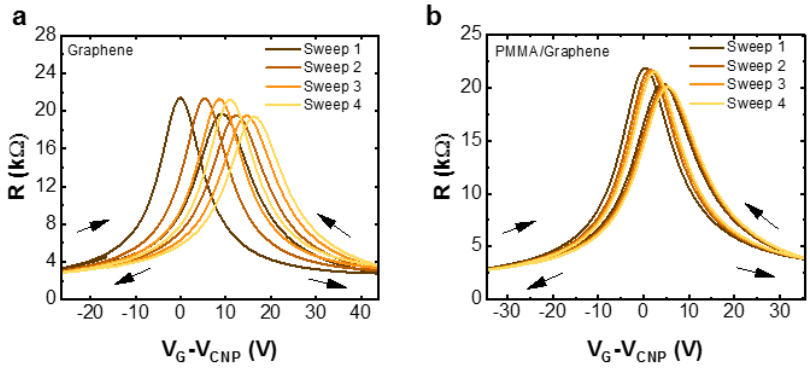

Figure 4.11. Evolution of transfer characteristics as a function of applied back gate voltage over several back-gate sweeps for the a) uncapped graphene device and b) PMMA-capped device.

The role of PMMA capping in Chip 3 is further demonstrated when studying the effect of aging (figure 4.10). The position of VCNP is increased over time (VCNP ~18.3±1.1 V after 2 weeks, ~24.3 V after 4 weeks and ~35±1 V after 10 weeks), though the shift is much smaller than for

Chip 2. Even more strikingly, as can be seen in figure 4.12, Chip 3 shows almost negligible hysteresis over the whole aging period. ΔV remains ~1.0 V even after 4 weeks, finally reaching a maximum average ΔV ~3.0±0.7 V after 10 weeks. This is particularly important, as small hysteresis is crucial to obtain reproducible performance of sensors.

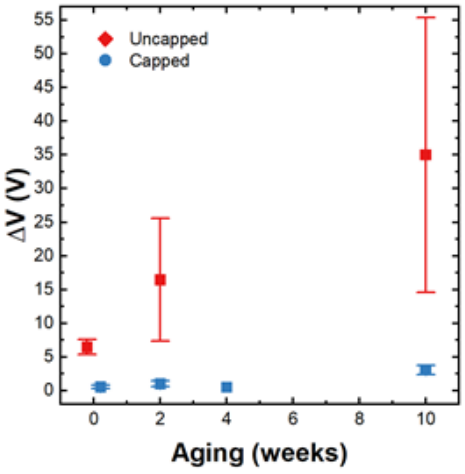

Figure 4.12 Hysteresis of uncapped (red) and capped (blue) graphene devices as a function of aging time.

Figure 4.13 and 4.14 also shows the electrical performance of 3 representative Hall bars (HB1-HB3) on chip 3. We plot the resistivity (figure 4.13 (a)), Hall voltage (figure 4.13(b)) and S_I (figure 4.13(c)) after device fabrication and PMMA capping.

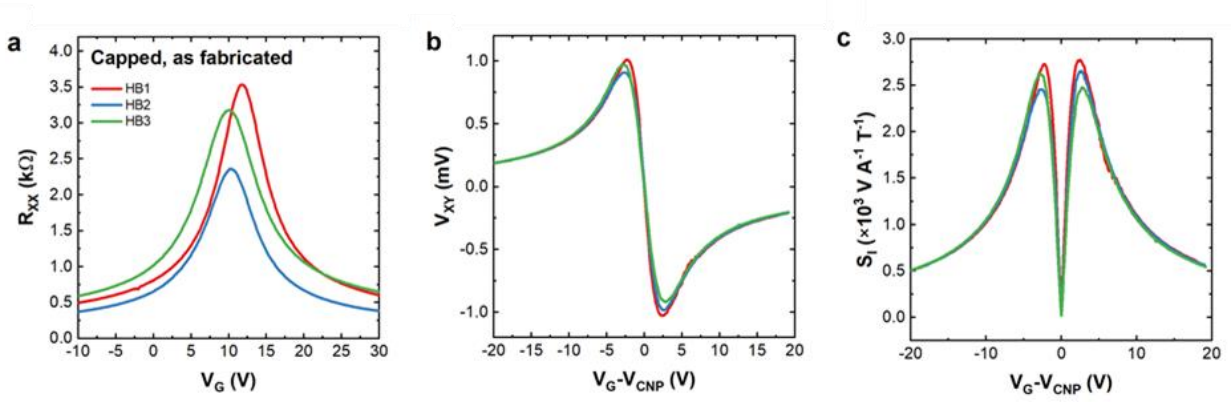

Figure 4.13. (a-c) Electrical performance of Chip 3 after PMMA encapsulation, showing resistance (a), Hall voltage (b) and current-related sensitivity (c) as a function of applied gate voltage.

Compared to Chip 1 (see figure 4.4 (b)), the electrical performance of the sample is slightly reduced, but device-to-device variation is small. Even after 10 weeks we measure resistivity (figure 4.14 (a)), Hall voltage (figure 4.14 (b)) and S_I (figure 4.14(c)) values which compare well with SOTA performance of devices based on CVD graphene.

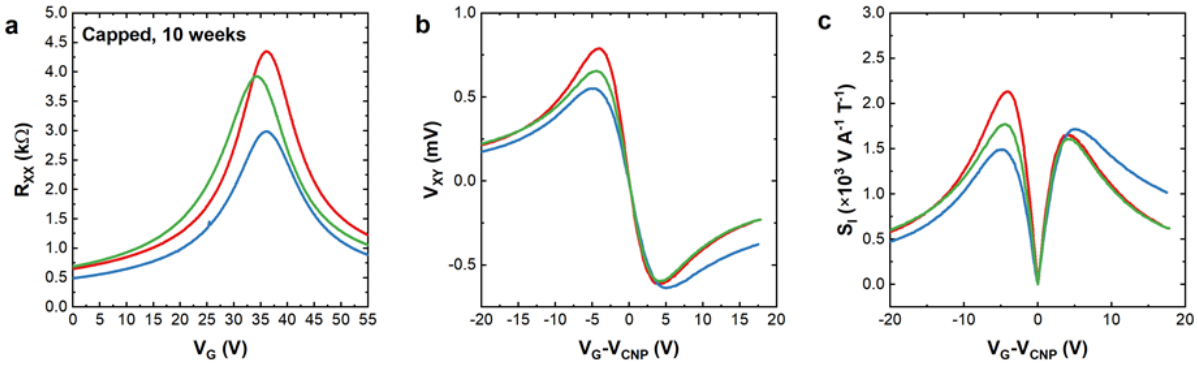

Figure 4.14. (a-c) Electrical performance of chip 3 after 10 weeks of aging, showing resistance (a), Hall voltage (b) and current-related sensitivity (c) as a function of applied gate voltage.

Table 4.1 compares our results to other Hall sensors presented in literature, listing figures of merit such as S_I, μ and n* (where available), as well as the compatibility of the adopted materials with wafer-scale fabrication. As it can be noted, the sensitivity of our devices well compares to that obtained with only exfoliated flakes of graphene and hBN. Yet, our devices offer scalability and thanks to the polymeric capping approach the issue of overtime stability is also addressed.

Table 4.1. Comparison of figures of merit for graphene Hall sensors fabricated with different approaches and the data measured in this work.

Type	S_I (V A^{-1} T^{-1})	μ (cm^2 V^{-1} s^{-1})	n* (cm^{-2})	Potential scalability
Exfoliated graphene encapsulated with exfoliated hBN [148]	5700	N/A	N/A	No
Polycrystalline CVD graphene encapsulated with CVD hBN [144]	97	1200	N/A	Yes
Single-crystal CVD graphene on SiO_2 [119]	2745	7800	1.75×10^{11}	Yes

Single-crystal CVD graphene encapsulated with exfoliated hBN on Kapton [159]	2270	~17 000	N/A	No
This work	~5030 (~2130 after 10 weeks)	~12 000	9.5×10^{10}	Yes

4.3 Conclusions

In this chapter, we have demonstrated a facile and scalable approach to fabricate highly sensitive graphene-based Hall sensors. As-fabricated, our devices have high average carrier mobility ~1.2×10^4 $cm^2V^{-1}s^{-1}$ with a low residual charge carrier density <1.0×10^{11} cm^{-2}. This allows us to reach high Hall voltage, corresponding to average current-related Hall sensitivity of ~4600 $VA^{-1}T^{-1}$ (with the best-performing device showing >5000 $VA^{-1}T^{-1}$), which is a record value for devices based on CVD graphene. We use a polymeric (PMMA) capping to minimize the effects of atmospheric adsorbents, thus ensuring stable performance (i.e. low hysteresis <1 V) of our devices even when measured in ambient conditions. Furthermore, PMMA capping slows down the degradation of device performance even when stored in air for prolonged times (up to 10 weeks). It is also notable that the deposition of PMMA capping does not require highly specialized equipment (i.e., only a simple table-top spin-coater and a hotplate) and provides a simple way to stabilize the fabricated devices for ambient environment measurements. However, more detailed research of wafer-scale encapsulants, providing scalable, ambient stable graphene based Hall elements is very much necessary for future integration of graphene in upcoming magnetic sensing technologies. Our work ultimately demonstrates that monocrystalline CVD graphene on Si/SiO_2 can be a viable material for scalable production of Hall sensors whose performance exceed those fabricated using conventional technology.

Chapter 5

Graphene pn-junction as a visible light photovoltaic sensor

In this chapter, a facile and scalable approach to design a stable graphene pn-junction based photodetector is described. In particular, fast and stable detection of visible light is vital in optoelectronic devices while utilizing them in different technologies i.e., automotive application. However, due to gapless and atomically thin nature, bare graphene usually shows low absorption of light which limits its use in photodetection. Therefore, an alternative to bare graphene is needed. For this purpose, we have demonstrated an approach to create stable graphene pn-junction fabricated by using EBL technique. These graphene pn-junctions are ambient stable owing to a thin PMMA layer deposited on top, which not only provides the stability to the device but – if opportunely tailored – can also act as an antireflective coating [160] and hence boosts the light sensing performance. We have investigated the electrical and optical performance of graphene based pn-junction devices thoroughly followed by structural and doping analysis by Raman spectroscopy.

5.1 Advantage of graphene pn-junction for visible light detection

Photodetectors are key components for different types of technologies such as optical communication in vehicles,[81] and in other technological applications where photonic circuits are needed.[10,78,161] Graphene, owing to its exceptional properties, has shown a great potential not only for electronics but also for optoelectronic applications [113] becoming one of the best candidate materials for converting light signals into electrical signals in future photonic devices.[162–166] Due to the zero-bandgap, graphene is ideal for broadband light detection, although is atomic thickness limits its light absorption and solutions are called to augment the photoresponse of graphene-based photodetectors.[167,168]

The idea of a p–n junction was first presented by Ohl [169] in 1941 at the Bell Laboratories. Basically, a p–n junction was designed at the lateral interface between n-type and p-type silicon. At the interface, charge rearrangement took place, producing a built-in potential which helped in the separation of the excited electron and holes when the energy of incident photons exceeded the bandgap of silicon, facilitating its applicability in optoelectronic devices.[170]

To exploit the full potential of graphene as a visible light photodetector, the fabrication of graphene pn-junctions, which are pivotal in semiconductor-based photodetectors [171,172], is required. Over the years, different type of procedures have been employed to fabricate graphene pn-junctions for light detection such as multiple gating,[173,174] chemical doping, [175] different metal contact deposition, [176] and lateral junctions with other 2D materials.[177,178] However, all the methods mentioned above present technological limitations that need to be overcome. Various systems have been already employed to boost the performance of graphene-based photodetector such as graphene decorated with quantum dots, where the detector speed needs to be improved, and integration into photonic waveguides, which is not trivial in terms of fabrication steps (being the adopted photonic structures complex).[179–181] [182] [183].

In recent times, there has been a quite extensive amount of research devoted to defining the doping in graphene while using focused ion or electron beams.[184,185] In particular, it has been experimentally shown that by controlling the energy of the focused electron beam, a p-type or n-type doping of graphene can be achieved.[186] To date, graphene based pn-junctions defined by electron and ion beams have been demonstrated while using mechanically exfoliated graphene and often measured in vacuum atmosphere.[186–188] To augment the technological potential of these solutions, one would need to extend the study to CVD-grown graphene and perform measurements in ambient conditions.

Here, we demonstrate an approach to define lateral pn-junctions on scalable CVD-graphene by partially exposing the graphene device channel with electrons while protecting the device with a thin PMMA layer. PMMA layer semi-encapsulation of the graphene channel helps to preserve the doping created by the electron beam and thus define a pn-junction (irradiation induces band bending at the SiO_2/graphene). Electron-hole pairs are generated in graphene and charged carriers are trapped at the interface of Si/SiO_2 due to the mismatch of Fermi energy.[187,189] The as designed graphene pn-junctions are used as a visible light sensors at zero applied bias displaying self-powered photodetection mechanism. A large photoresponse compared to bare graphene is achieved without applying any external bias while shining the light at the lateral graphene pn-junction. This methodology allows us to define stable CVD graphene pn-junctions and utilize them as self-powered visible light sensors, demonstrating the potential of graphene for low power consumption optoelectronics.

5.2 Experimental results and discussion

5.2.1 PN-junction device fabrication process

Firstly, the graphene single-crystals were grown by using CVD within a cold wall reactor with a procedure reported in reference[60] and already described in detail in chapter 2. The graphene single-crystals were then transferred on Si/SiO_2 by using the semi-dry transfer technique reported previously and discussed in chapter 3.[94,155] Afterwards, electron beam lithography was implemented to define the device (GFET) channel at 20 kV and 60 µm aperture with ~ 0.85 nA of current and at 270 $\mu C/cm^2$ of dose. The extra graphene was etched away by using reactive ion etching with oxygen and argon plasma with flow of Ar/O_2:5/80 sccm.

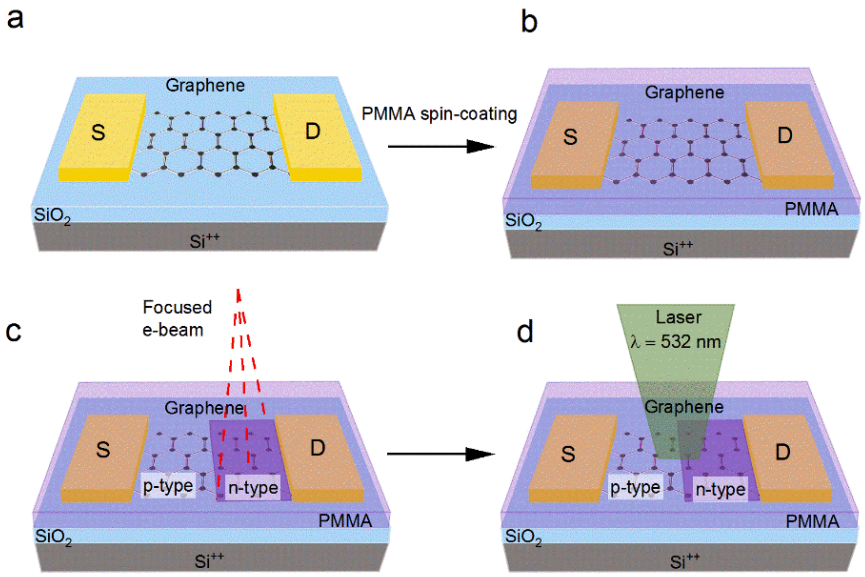

Figure 5.1. Schematics (a-d) depicting the process flow of fabrication of CVD graphene pn-junction and its use as a visible photodetector. Half of the channel is exposed with e-beam to create n-type doping.

The metallic contacts were later deposited on graphene by following the same electron beam lithography procedure. A positive e-beam resist (PMMA AR-P 672.045) was always used in each step of lithography. In addition, once the graphene FET was ready, a layer of ~ 240 nm PMMA was deposited and half channel of the graphene device was exposed to the electron beam radiation in a controlled manner with scanning electron microscope (SEM) at 20 kV acceleration voltage and 500 $\mu C/cm^2$ dose with nearly ~ 1 nA of current for 8 seconds. A schematic depiction of the

graphene pn-junction fabrication process is shown in figure 5.1. The size of graphene device channel was of 30 μm in length with a width of 6 μm.

5.2.2 Raman spectroscopy analysis of the pn-junction

Firstly, to elucidate the impact of e-beam irradiation on the graphene channel, Raman spectroscopy was used to investigate the structural and doping profile. Raman spectroscopy was performed on both the unexposed and the electron beam exposed portion of the device. In particular, figure 5.2 (a) is depicting the D-peak Raman intensity map of the unexposed and the e-beam exposed graphene with their respective spectra in figure 5.2 (b). It can be evidently seen that the exposed graphene region possesses a clear D-peak at ~ 1341 cm^{-1}, while unexposed graphene does not present it.

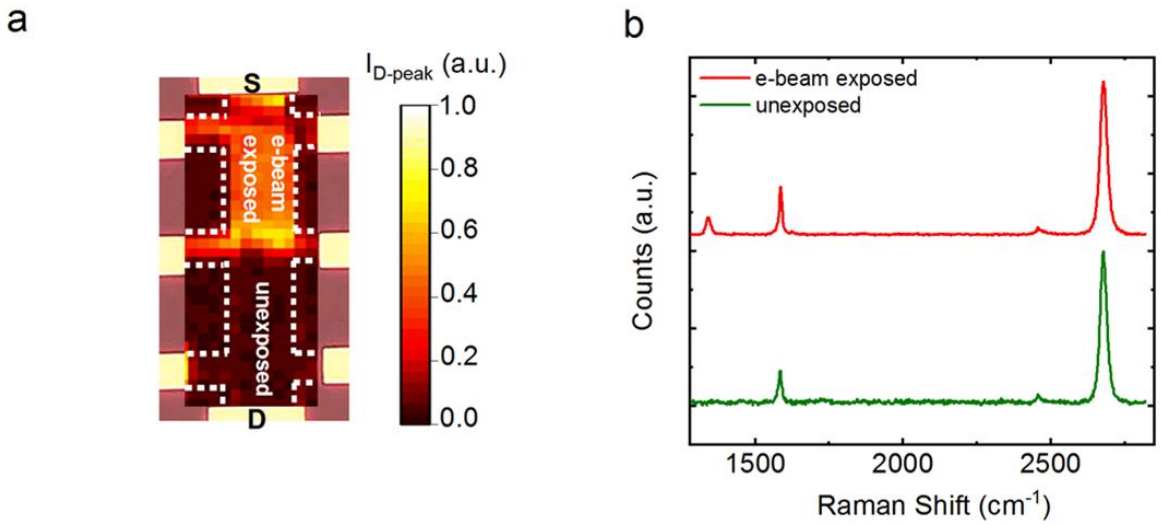

Figure 5.2. (a) Raman mapping of the D-peak intensity on the channel of graphene pn-junction field effect transistor (FET); (b) Raman spectra of both e-beam exposed and unexposed graphene after electron irradiation.

The appearance of a D-peak in e-beam exposed graphene is due to the lattice defects created after electron bombardment.[185] The average value of the intensity ratio of D and G-peak (I_D/I_G) for the e-beam exposed graphene is ~ 0.75±23 while for unexposed graphene is ~ 0 as expected and depicted in figure 5.3. The intensity ratio of the D and G-peak is indicative of the structural integrity (i.e., presence of defects) of graphene and the data confirm that e-beam

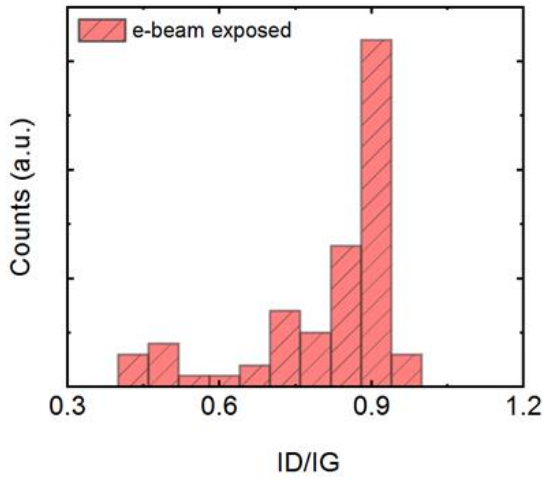

Figure 5.3. Depicting intensity ratio of the D and G-peak of the e-beam exposed portion of the graphene channel.

exposed graphene portion is more defective compared to the unexposed graphene portion. Figure 5.4 (a) shows the correlation plot of the intensity ratio of 2D and G peak (I_{2D}/I_G) and the G peak position in the graphene channel. The average value of I_{2D}/I_G for unexposed graphene is around ~5 while for exposed graphene it is nearly ~ 2.8 which is due to the 2D peak intensity decreases after electron beam irradiation confirming graphene quality degradation.[187] Another reason for the decrease in I_{2D}/I_G can be considered the amorphization of graphene, [184] under electron beam irradiation. However, the amporphization usually happens for long exposure time (≥ 50s), [187] while in our case the exposure time was ~ 8s. Furthermore, the average value of the position of G-peak for the unexposed graphene channel is around ~1584 cm^{-1} compatible with what measure for p-type doped graphene due to ambient exposure during transfer and device fabrication process.[139]

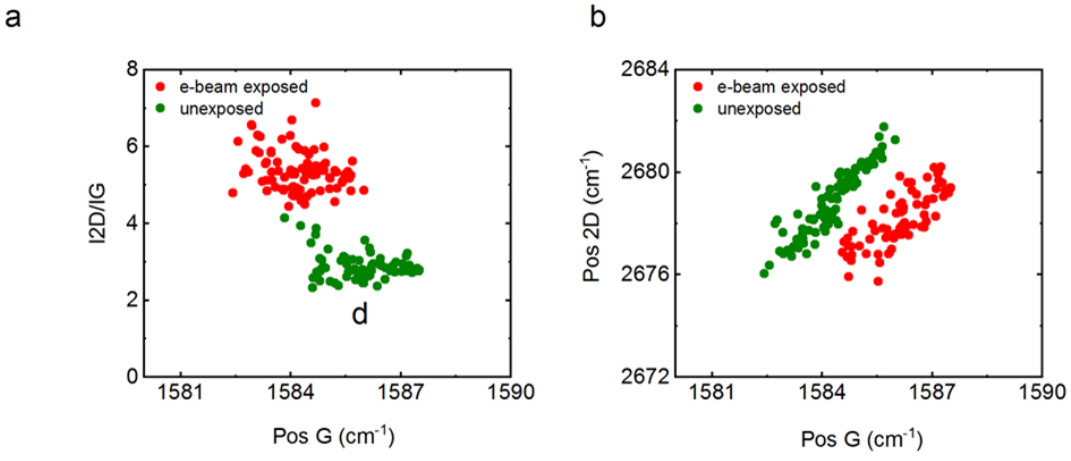

Figure 5.4. (a) Depicting the intensity ratio of the 2D and G-peak; (b) 2D peak position as a function of G-peak position of e-beam exposed and unexposed graphene channel.

process.[139] However, for the electron irradiated graphene the G-peak position is higher, around ~1585.9 cm^{-1} as depicted in figure 5.4 (b). The strong blue shift in the G-peak position of graphene after electron beam irradiation could be attributed to the charge transfer from the electron irradiation resulting in n-type doping of graphene [190], similar to what reported in [186]. In addition, the position of the 2D-peak does not show any strong shift or dependence to the electron irradiation as depicted in figure 5.4 (b). Additionally, we plot the Raman correlation maps of the full-width at half maximum (FWHM) of G-peak and the area ratio of the 2D and G-peak versus the position of the G-peak as depicted in figure 5.5 (a) and (b), respectively.

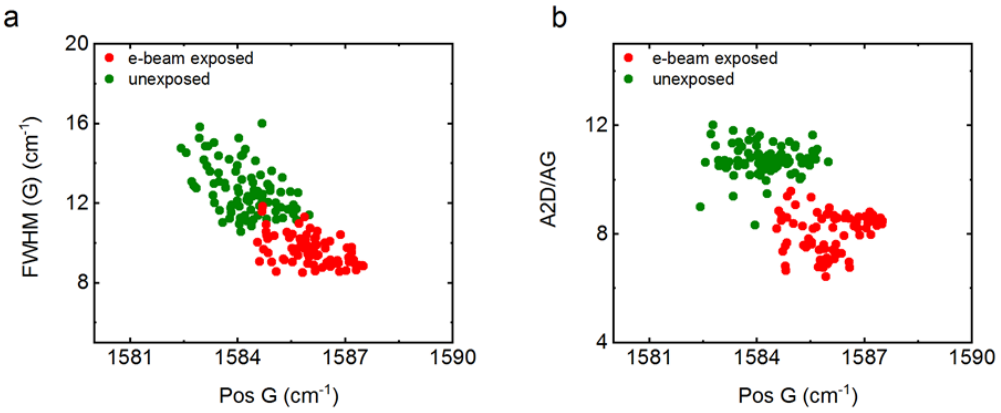

Figure 5.5. (a) FWHM of G-peak as a function of G-peak position; (b) area ratio of 2D and G-peak position of e-beam exposed and unexposed graphene channel.

The FWHM of the G-peak for the unexposed graphene channel averages at ~ 12.7 cm^{-1} wile for exposed graphene is around ~ 10 cm^{-1} as shown in figure 5.5 (a). Figure 5.5 (b) is depicting the area ratio (A_{2D}/A_G: similar to what found in panel 5.4 (a) for the exposed graphene region the area ratio of the 2D and G peak is lower (~ 7.9) than for the unexposed one (~ 10.8), a further indication of defect formation in the irradiated portion of the channel.[102,155] In conclusion, Raman analysis indicates that irradiating graphene with electron beam induces defects and doping in the crystal.

5.2.3 Electrical properties investigation

We now move to study the electrical behavior and doping profile of the devices by electrical characterization. After graphene FET fabrication, and before e-beam irradiation of the channel, electrical measurements were performed in four probe configuration. A constant current of 1 μA was applied to the graphene channel and the voltage drop was measured while applying a back gate voltage using Si as a back gate by following the same approach discussed in chapter 3 and chapter 4. The bare graphene device shows a CNP value ~ 5.5 V in ambient at room temperature (blue line in figure 5.6), indicating p-type doping as it is typically observed in as fabricated graphene FETs (as a consequence of ambient exposure and polymeric residues).

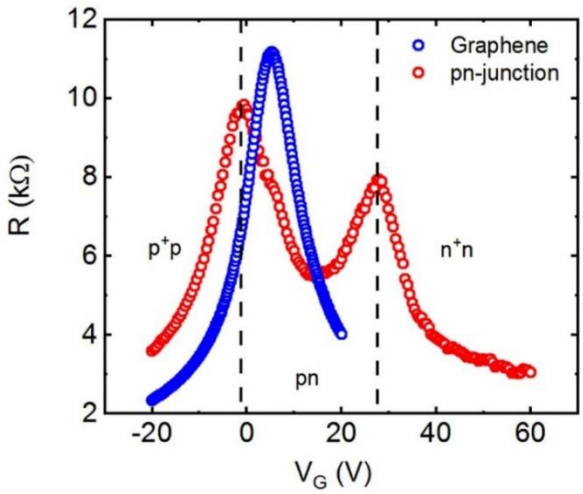

Figure 5.6 Transfer curve of the graphene FET device measured before and after creating the pn-junction with e-beam irradiation.

However, when part of the graphene channel is irradiated with controlled electron beam, the resistance measurement shows two separate peaks, at ~-1.5 V and ~27.5 V, corresponding to different CNPs in the p-type and n-type regions of the graphene channel. The band bending at the SiO_2/graphene interface arises when energetic electron beam irradiates the sample. Electron-hole pairs are generated in graphene and charged carriers are trapped at the interface of Si/SiO_2 due to the mismatch of Fermi energy.[187,189] The so-generated static electric field induces an n-type doping in graphene.[187] An increase in p-type doping in the non-irradiated region might arise due to atmospheric exposure,[139] as graphene is exposed to air during some steps of the fabrication process.

The mobility of charge carriers is an essential factor to asses the quality of the graphene device.

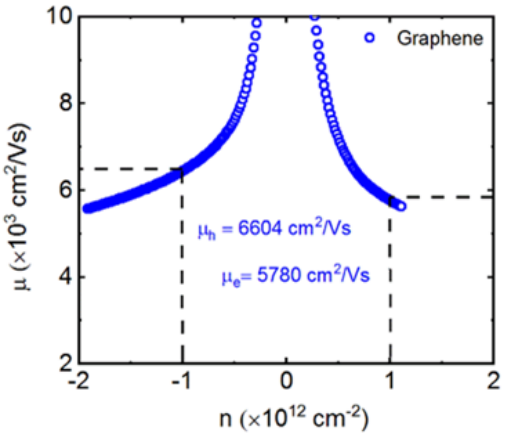

Figure 5.7. Displaying the electron and hole mobility of bare graphene device immediately after fabrication in ambient at room temperature.

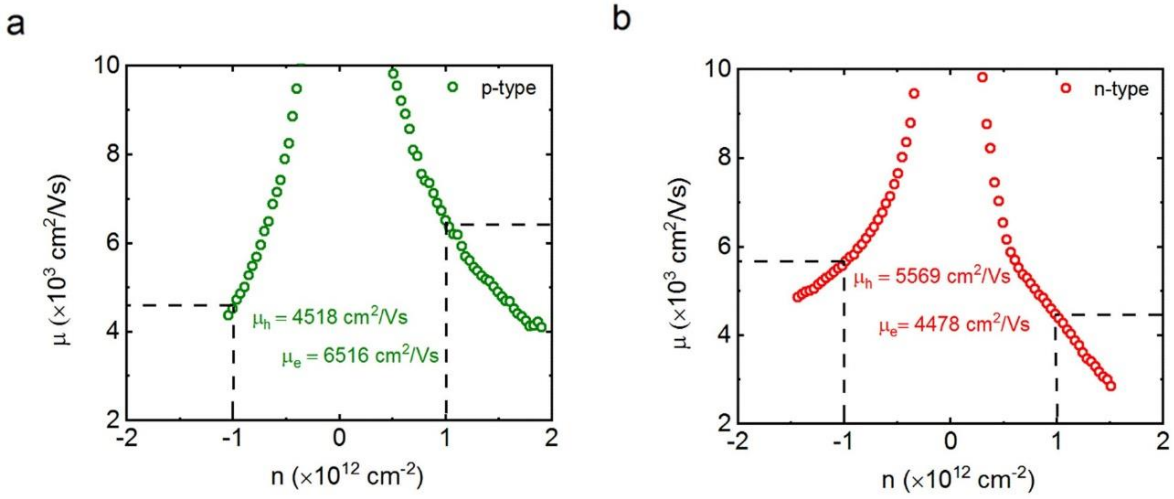

Figure 5.8. (a) Depicting Electron and hole mobility as a function of carrier density of p-type graphene; (c) and n-type graphene channels created with focused e-beam.

Figures 5.7 and 5.8 depict the mobility of both holes and electrons in bare graphene and in p-n junction graphene created by e-beam irradiation, respectively. Before the junction fabrication the

mobility of hole (μ_h) and electron (μ_e) is 6604 cm^2/Vs and 5780 cm^2/Vs, at a carrier concentration of 10^{12} cm^{-2}, which falls within the upper range for non-encapsulated graphene on SiO_2 in ambient conditions reported.[94,112] After the e-beam exposure, the electron and hole mobility for p-type graphene is observed around $\mu_e \sim 6516$ cm^2/Vs and $\mu_h \sim 4518$ cm^2/Vs. In the p-type portion of the device, the electron mobility remains almost unchanged while a decrease in the hole mobility is observed which might be due to the fact that graphene is exposed to ambient several times during p-n junction fabrication. Additionally, the air exposure usually makes graphene more p-doped, leading to a higher hole density and consequently lowering hole mobility due increased carrier scattering.[139] While, in case of n-type channel, both hole and electron mobilities decrease compared to pristine graphene showing values of $\mu_e \sim 4478$ cm^2/Vs and $\mu_h \sim 5569$ cm^2/Vs. The reduction in the carrier mobility of the n-type region can be attributed to the carrier scattering from defects created in graphene after electron beam irradiation.[191] Meanwhile, a slight decrease in the channel resistance is observed in graphene p-n junction which might be due to the PMMA coating which leads to interface charge trapping suppression via blocking adsorption of O_2 and H_2O molecules from ambient.[192] For each type of graphene channel, electron and hole mobility values were calculated by using Drude model at technologically relevant carrier density of 1×10^{12} cm^{-2}.[120]

5.2.4 Optical response of the pn-junction device

After investigating the structural properties and doping profile of graphene pn-junction devices with Raman and electrical measurements, we move to characterize their optoelectronic properties.

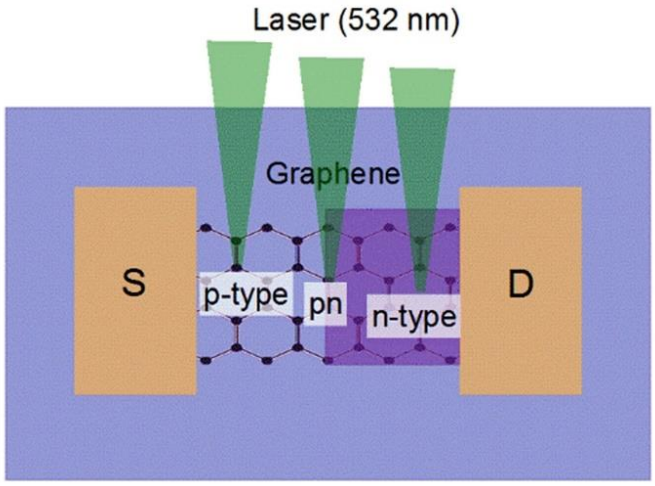

Figure 5.9. Displaying three different regions of the graphene pn-junction device where the laser is focused to detect any possible photocurrent.

In particular, these pn-junction based on PMMA covered graphene are used as visible light sensors. In order to detect the light, the pn-junction was initially placed in the optical system (Raman spectrometer) while the source-drain contacts were used to detect any possible current generation at the junction after shining the light. For this purpose, the graphene pn-junction FET device was placed under a laser of 532 nm of wavelength, focused with a microscope optics (50x magnification) and a spot size of 2 µm. The laser was focused on three different areas of the channel: the unexposed region (p-type), the e-beam exposed region (n-type) and the pn-junction as shown in the schematics in figure 5.9. In particular, zero external source-drain bias (V_{SD} = 0) and gate bias (V_G = 0) was applied to the device in order to investigate the possible self-powered nature of the device. When the laser with a power of 12 mW was illuminated on the unexposed (p-type) graphene channel a negligible change in the source-drain current was observed as expected due to low light absorption of graphene as shown in figure 5.10.[193]

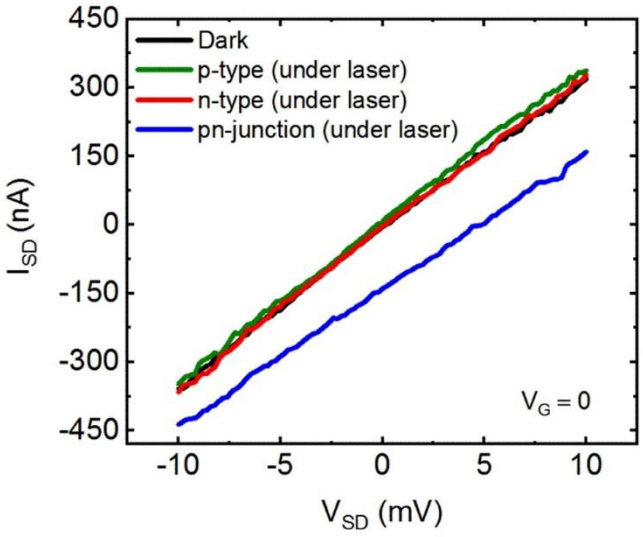

Figure 5.10. Representing source-drain current (I_{SD}) of the graphene pn-junction as a function of source-drain voltage (V_{SD}) in the dark mode and under laser shined on p-type, n-type and at pn-junction separately at V_G =0. Laser of 532 nm wavelength with a power of 12 mW and spot size of ~ 2 µm is used.

A similar effect of light illumination was observed on the e-beam exposed (n-type) side due to negligible amount of light absorption by graphene depicted in figure 5.10. This negligible change in I_{SD} might be due to the compensation of doping for graphene on SiO_2 under laser illumination.[194] However, when the laser was focused on the junction created after controlled e-beam irradiation, an obvious amount of change was observed in I_{SD} which is assigned to the photocurrent generation at the junction as shown in figure 5.10. The reason behind the photocurrent generation at the graphene pn-junction can be due to the photovoltaic effect as previously also observed for lateral graphene pn-junctions.[172,187,193,195] A schematic of the photovoltaic mechanism behind the photocurrent generation is depicted in figure 5.11. In particular, when the laser is illuminated at the graphene pn-junction, electron-hole pairs are generated which are further separated by the built-in electric field at the junction, showing self-powered mechanism.

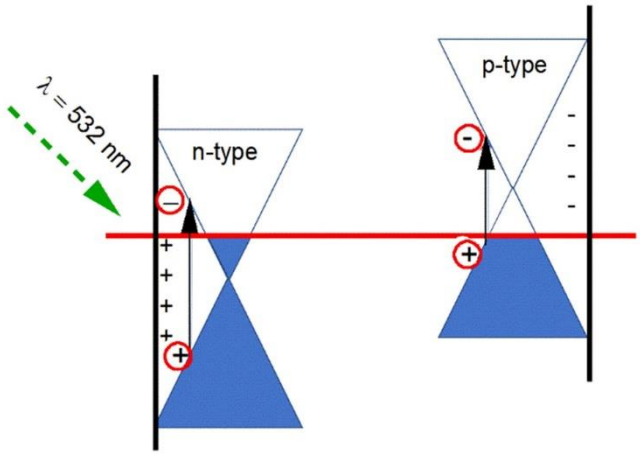

Figure 5.11. Schematic of photovoltaic effect, responsible for photocurrent generation at the graphene pn-junction under laser illumination. Laser of 532 nm wavelength with a power of 12 mW and spot size of ~ 2 µm.

To understand the time response of the pn-junction graphene photodetector, the laser was switched on/off on the three different regions of the device. Figure 5.12 is depicting the photocurrent generated at p-type, n-type and at pn-junction of graphene as function of time where laser is switched on/off manually at 20 s of interval at zero applied gate and source-drain bias ($V_G = V_{SD} = 0$). The photocurrent (I_{photo}) generated at n-type and p-type is around ~2 nA and ~ -2 nA,

respectively, while at pn-junction is around ~ -120 nA. It can be clearly seen that the photocurrent (I_{photo}) generated at the pn-junction is 60 times higher than the value observed for exposed or unexposed graphene. The photocurrent generated at graphene p-n junction is comparable to the previously reported values of lateral graphene p-n junction photodetectors.[187,196–198]

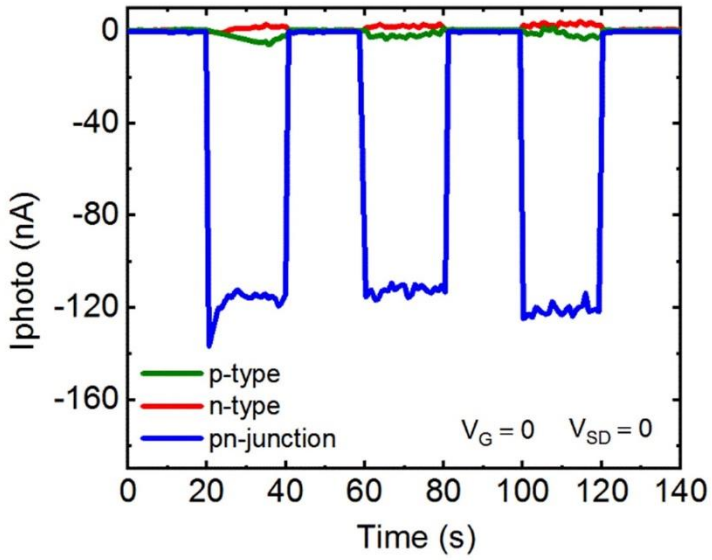

Figure 5.12. photocurrent generated at n-type, p-type and at the pn-junction as a function of switching on/off time at $V_{SD} = V_G = 0$. Laser of 532 nm wavelength with power of 12 mW and spot size of ~ 2 µm is used. The polarity of the photocurrent generated at the graphene pn- junction is in clear agreement with the polarity of the p–n junction characterized electrically as shown in figure 5.6.

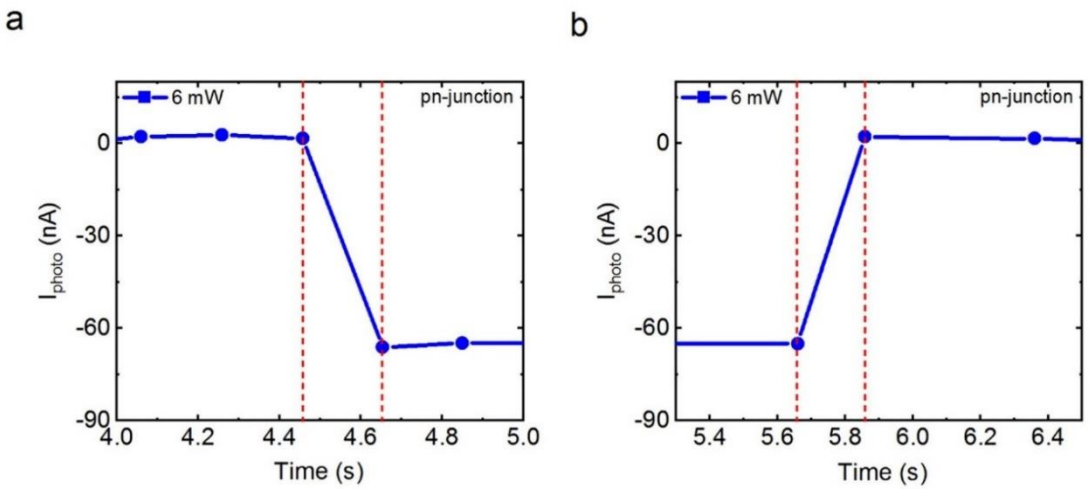

Figure 5.13. (a-b) Zoom in of the time scale as a function of photoresponse of the PMMA protected graphene based pn-junction photodetector showing rise and fall time.

The rise and fall time of the pn-junction photodetector were recorded at a power of 6.0 mW while the laser was switched on/off manually and the relative measurements are shown in figure 5.13. In particular, the value of the rising time was recorded to be ~ 197 ms and the falling time was ~ 198 ms. The response time is possibly limited by the measurement setup rather than the photodetector itself as the laser was manually switched. To better understand the behaviour of our graphene p-n junction photodetector, we compared the photo response at different values of laser power. In figure 5.14, the I_{SD} versus VSD is shown for different laser power on p-n junction (VG = 0): a clear increase in I_{SD} as a function of the laser power is observed, due to more electron-hole pairs generated at the junction.

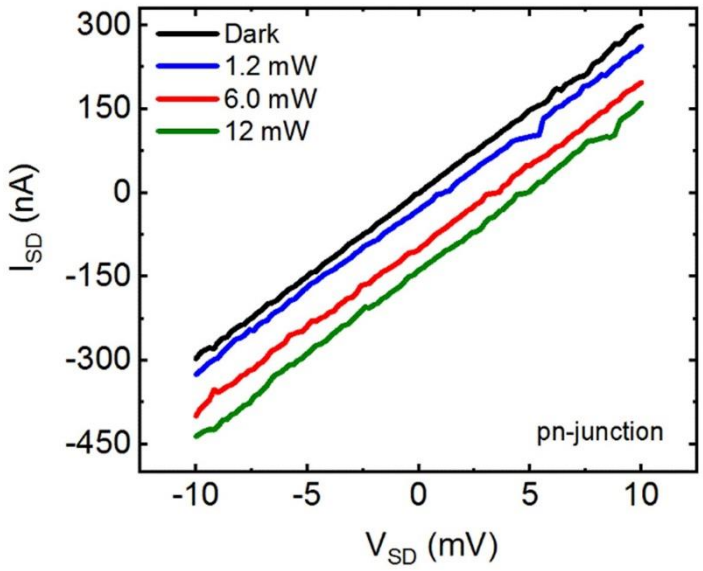

Figure 5.14. Depicting source-drain current (I_{SD}) of pn-junction as a function of applied source-drain bias (V_{SD}) at zero gate voltage (V_G = 0). A laser of 532 nm wavelength at power 1.2 mW, 6mW and 12 mW was used.

Another comparison can be directly made between the optical power applied to the pn-junction photodetector and the photocurrent generated. A clear representation is made in figure 5.15 showing the increase in photocurrent with the applied optical power.

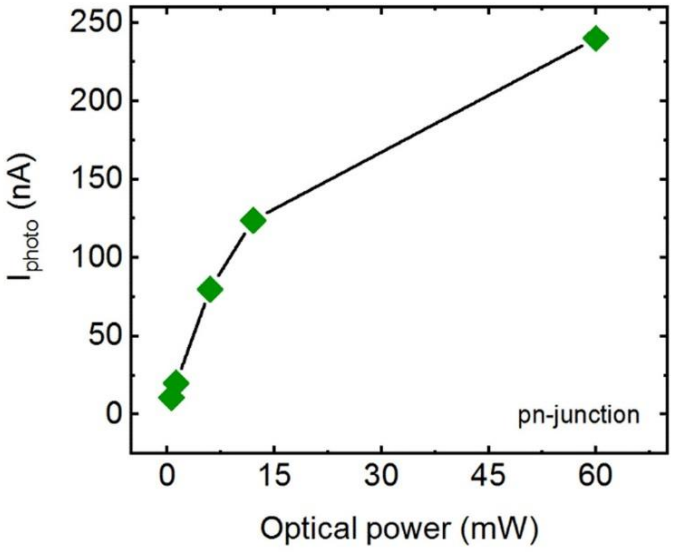

Figure 5.15. Depicting photocurrent as a function of optical power applied to the pn-junction device. The laser of 532 nm wavelength at different power of 1.2 mW, 6 mW and 12 mW is used.

Additionally, the photoresponse of the pn-junction photodetector was measured as a function of time at different applied optical power for the same device channel while the laser was switched on/off each 20 s manually.

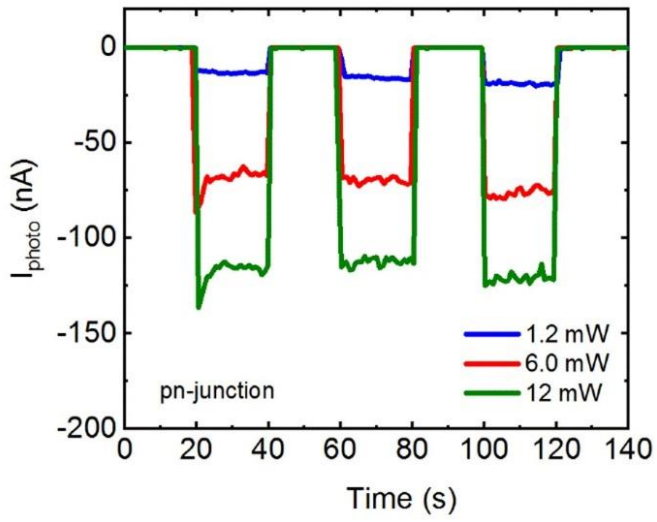

Figure 5.16. Portraying photocurrent as a function of laser switching at different laser optical power.

As expected, the photocurrent increases after each increment in the optical power and the photoresponse is stable at each applied optical power as depicted in figure 5.16. This optical response is recorded at zero applied source-drain and gate voltages ($V_{SD} = V_G = 0$) showing a self-powered behavior.

One of the main characteristics of a photodetector is the responsivity, which can be calculated by using relation;

$$Responsivity = Iphoto/P \qquad \text{Eq. 4.1}$$

where P is the optical power and Iphoto is generated photocurrent. The calculated responsivity in our case is ~ 18 µA/W for laser power of 1.2 mW shown in figure 5d while comparing the responsivity with optical power, which is on par for lateral graphene p-n junction.[196,197,199]

It is important to note that bare graphene photodetector suffers the lack of electrical stability and a very slow response due to the continuous ambient exposure triggering photo-induced molecular adsorption on graphene surface.[200] The semi-encapsulated graphene pn-junction photodetector presents enhanced stability, similar to what reported in [201,202], as shown in figure 5.17.

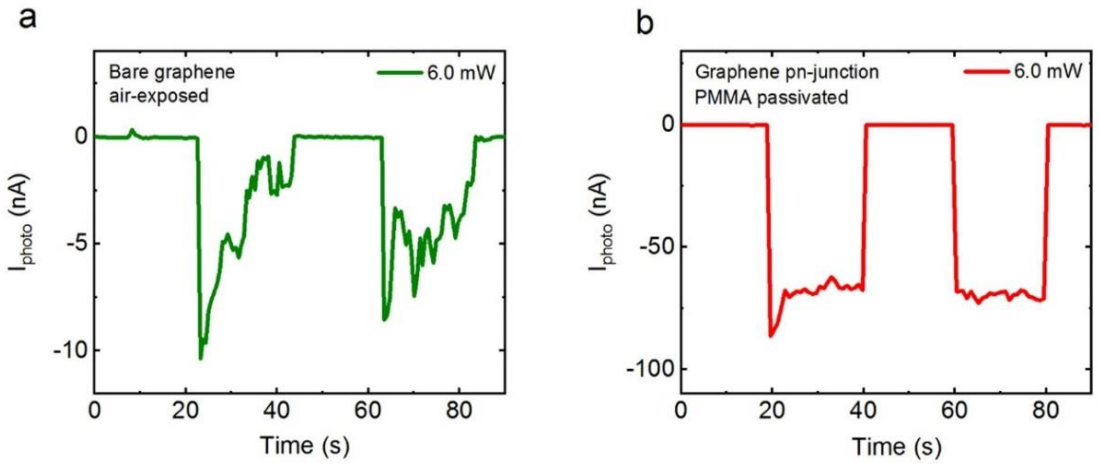

Figure 5.17. (a) Showing photocurrent of air exposed graphene photodetector without pn-junction and PMMA protection; (b) photocurrent of PMMA passivated graphene pn-junction photodetector at 532 nm laser wavelength.

Furthermore, to includie graphene-based visible light sensors in technological applications such as in the automotive field, scalability and reproducibility of the adopted techniques should also be considered.

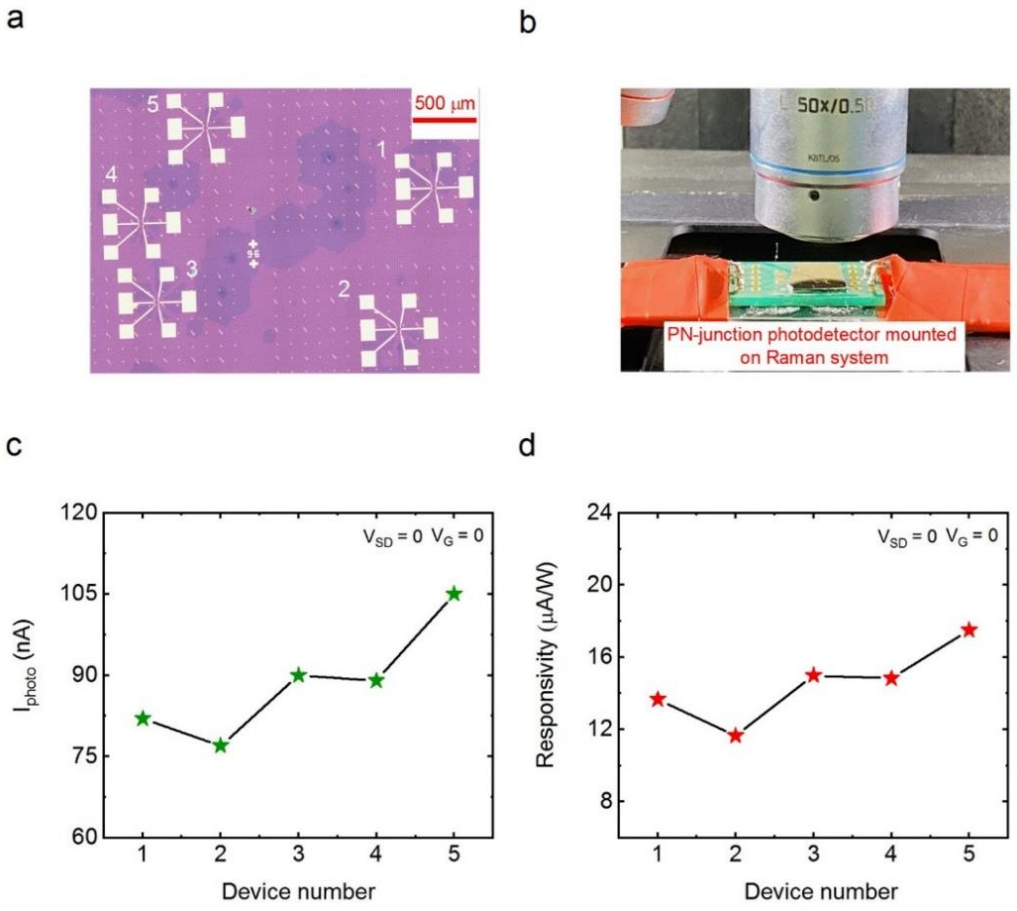

Figure 5.18. (a) Optical image of 5 pn-junction photodetector devices on same chip; (b) image of graphene pn-junction photodetector mounted on Raman system for optical characterization; (c-d) photocurrent and responsivity of 5 different pn-junction photodetectors at 6 mW of power and 532 nm laser wavelength.

Therefore, we have fabricated five different PMMA capped graphene based pn-junction photodetectors on a single chip. In particular, the photocurrent generated at each device and the corresponding responsivity are shown in figure 5.18.

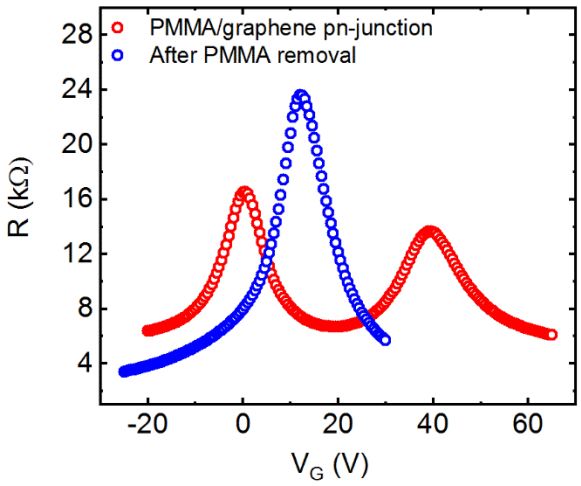

Figure 5.19. Depicting the resistance as a function of applied back gate voltage of PMMA capped graphene pn-junction device and after PMMA removal.

The results demonstrate a reproducible behavior for the visible light photodetectors. Additionally, figure 5.19 shows that the n-type doping of the graphene photodetector is protected by the thin PMMA layer. Once the PMMA layer is removed, the n-type doping gets erased due to ambient exposure[139] and the device becomes p-type again with the junction behavior erased as well.

5.3 Conclusions

In this chapter, we have demonstrated a simple, reproducible and scalable approach to realize CVD graphene based pn-junctions by using electron-beam irradiation. Raman and electrical measurements confirms the pn-junction formation in CVD graphene by e-beam irradiation. The as -abricated graphene pn-junctions are employed as a visible light sensor. The graphene pn-junctions present photocurrent generation of about ~ 120 nA and a reasonable responsivity of ~ 18 μA/W with response time of ~ 197 ms at 532 nm and 12 mW of laser wavelength and power, respectively. We assign the photoresponse in our graphene pn-junctions to the photovoltaic effect as the electron-hole pairs are generated at the pn-junction due to the light absorption and further separated by built-in electric field. Moreover, this work shows the possibility of using electron beam irradiation and PMMA semi-encapsulation to create stable and scalable pn-junction based on CVD graphene which might be of interest in different technological applications including those in the automotive sector.

Chapter 6

Interfacing graphene with rubbers: from electrical properties to functionalization studies

Graphene high thermal and electrical conductivity, and peculiar tribological properties (e.g., high Young modulus and breaking strength) make it an enticing candidate for tire applications. To this end graphene needs to be included in rubber blends and the effect of the interfaced rubbers on the properties of graphene needs to be unveiled. In this chapter, we explore from a fundamental perspective the potential integration of graphene and rubbers by investigating the effect that different rubbers, typically adopted in tire industry, have on the electronic properties of graphene. Additionally, graphene functionalization with different organic molecules that could be adopted in rubber blends is also carried out to investigate whether functionalization approaches could be put in place to improve graphene dispersion in the final composite material.

6.1 Graphene and graphene-based materials in tires

Rubbers, due to their viscoelastic nature and peculiar properties, have enabled different applications, and have a widespread use in the tire industry.[203] In tires, reinforcing fillers are mixed within rubbers to increase tire longevity, strength and in some cases to decrease greenhouse emissions. Carbon black is a popular filler due to its high tensile strength.[84] However, carbon black's recognized drawbacks are lack of improvement in rolling resistance and wet traction.[84] Moreover, carbon black is typically a derivative of crude oil and its production generates substantial waste and greenhouse gas emission. Currently, silica is also widely used as a filler material within tires.[204] It delivers superior resistance to wear and tear, lower heat build-up and improved tensile strength.[205] However, the lack of dispersity is particularly an issue with silica particles when being compounded in non-polar rubbers.[84] Recently, research has shown that graphene-based materials are potential candidate fillers: even low loadings of graphene have shown to provide rubber composites with improved mechanical properties.[84] Nowadays, graphene-enhanced tires are present in the market.[86] Major claims for such tires are improved grip, wear and weight reduction, and thermal dissipation as well as reduced weight. Yet, the dispersion of graphene in a rubber matrix is still a challenging task due to the high specific surface area and the van der Waals interactions characteristic of the material.[206] To obtain optimal

graphene and rubber composites, graphene needs to be homogeneously dispersed within the rubber matrix. The influence of graphene and graphene-based materials on the vulcanization process of the rubber composite should be fully understood as well as how to generate a strong interfacial interaction between graphene and rubbers. Also, the resulting properties of the final composite such as electrical conductivity which shall be guaranteed to avoid static charge buildup on the vehicle shall be investigated. To date, graphene functionalization has been shown to be essential to activate the interfacial interaction between graphene and rubbers [207] and might be a potential tool to improve dispersion and positively influence electrical conductivity. While choosing the functionalizing agent care should be posed (as for the fillers) due to increasing global warming issues so to reduce greenhouse gasses. To date, nitrogen containing compounds such as pyrroles and tetrazoles have been shown to hold great potential as functionalizing molecules for graphene in rubber blends.[208]

In this chapter, we investigate the electrical properties of graphene interfaced with rubbers, and investigate potential graphene functionalization pathways. We initially probe the interaction between rubbers and CVD graphene to understand at a fundamental level what are the effects of these rubbers on the properties of graphene. Different characterization techniques such as Raman spectroscopy, AFM and electrical transport measurements are utilized to assess changes in the properties of graphene when interfaced with rubbers. Then, we investigate CVD graphene functionalization with a simple, sustainable, environmentally friendly and economically viable method, suitable for large scale development while maintaining the ideal graphene structure. Different functionalizing molecules such as pyrrole and tetrazole are exploited for this purpose. Finally, functionalization of graphene inks with tetrazole is explored as a realistic route for tire applications.

6.2 Experimental methods and results

Graphene single-crystals were synthesized and later deposited on SiO_2/Si substrates by using the CVD [92], semi-dry transfer and 2SC cleaning approaches [155] described in chapters 2 and 3. By using the 2SC a very clean graphene surface could be ensured, thus allowing us to fully assess the doping effect of different rubbers and molecules on graphene. To understand the doping effect of rubbers and molecules on CVD graphene, Raman spectroscopy measurement were conducted by using a Renishaw InVia system accompanied with a 532 nm laser and ×100 objective.

Additionally, back gated graphene FETs were patterned by using EBL as discussed in chapter 2. The electric field effect was measured by using a pair of Keithley 2450 source-measure units for a 4-terminal resistance measurement and back-gate sweep.

The polymers NeocisBR (cis Polybutadiene) and SLR (Styrene 1,3- butadiene copolymer) were supplied by Versalis (Italy) and TRINSEO LIMITED (UK), respectively. Before depositing the polymers on graphene, 0.85 g of each polymer were diluted with 30 ml of toluene and stirred at 500 rpm at room temperature for 24 hours in a dark environment. The diluted solutions were then spin coated on the SLG graphene/SiO_2 samples at 3000 rpm for 60 seconds to obtain a thin uniform film of the polymers on the two different materials. The substrates were then heated at 120°C for 30 minutes to completely remove the residual solvent which was used to dilute the polymers. To get the information about the surface morphology of graphene and of the deposited thin films, atomic force microscopy (AFM) was performed with a Dimension ICON-PT (Bruker) and care was taken to avoid damaging the surface with the tip.

For heterocyclic molecule functionalization, both pyrrole and tetrazole were dissolved in THF (tetrahydrofuran) at concentrations varying from 0.1 mM to > 9mM and then drop casted on graphene. Raman spectroscopy was performed to analyze any doping and functionalization effect. Additionally, graphene inks were also utilized as ideal playgrounds to attempt functionalization instead of CVD graphene. To this end, graphene inks were sonicated in acetone for 15 minutes and then the tetrazole molecule was added to the solution and sonicated again for 15 minutes in a ratio of 2:1 respectively. Later, the solvent was stirred at 500 rpm and heated at 180°C for 3 hours to induce covalent functionalization. Afterwards, the graphene ink with tetrazole was centrifuged and washed several times in acetone and then deposited on SiO_2/Si substrates. Raman spectroscopy was performed to investigate the functionalized inks.

6.2.1 Morphology of rubbers deposited on graphene

In order to better understand the interactions between rubbers adopted in tires and graphene and facilitate the modeling of complex blends we started by investigating the morphological characteristics of rubbers deposited on CVD graphene. Specifically, two different types of high molecular weight rubbers were used for this purpose, i.e., NeocisBR and SLR, which are used for tire applications. Morphological characterization of CVD grown SLG where rubbers where deposited via spin-coating, was performed by AFM as shown in figure 6.1. More specifically,

figures 6.1 (a),(d) are showing the topography and height profile images of the edge of a graphene crystal transferred onto SiO_2/Si by using the 2SC method as explained in chapter 3. The RMS roughness of the pristine graphen surface is ~ 0.6 nm. After deposition of NeocisBR on graphene a homogenous carpet could be observed in topography (Figure 6.1b) and the measured RMS roughness was observed to be ~ 0.65 nm. AFM analysis performed for graphene after deposition of SLR revealed a similar morphology with surface roughness of about ~ 0.9 nm as illustrated in figure 3f with height profile in figure 6.1 (c).

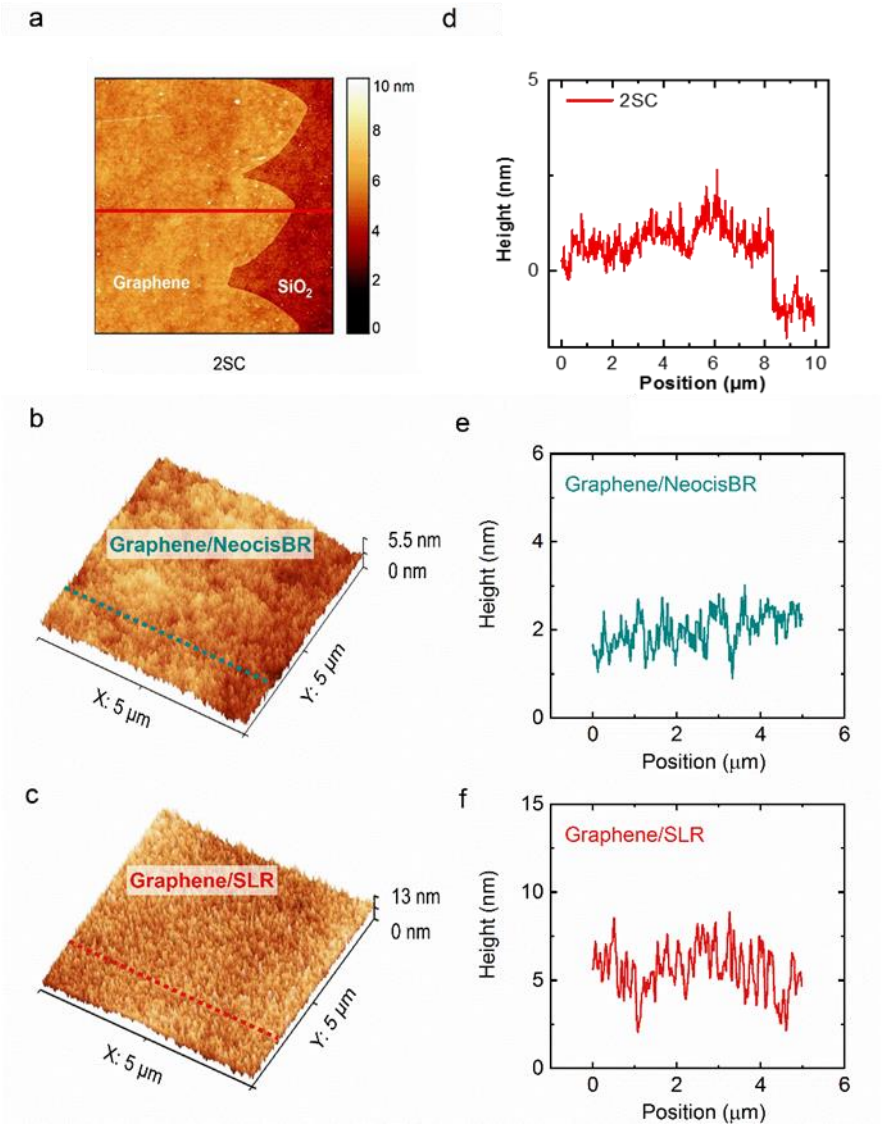

Figure 6.1. AFM images and relative line profiles of (a, d) pristine CVD graphene, (b, e) NeocisBR on graphene and (c, f) SLR on graphene.

The AFM analysis indicates that NeocisBR and SLR films are homogeneously distributed on the graphene surface after spin coating.

6.2.2 Raman spectroscopy of graphene with deposited rubbers

After AFM, we conducted Raman spectroscopy to investigate in a non-destructive way the effect of rubbers on the electrical and chemical properties of graphene. [95] Figure 6.2 is depicting the Raman spectra of bare graphene on SiO_2/Si (blue line), NeocisBR (black line) and NeocisBR deposited on graphene (red line).

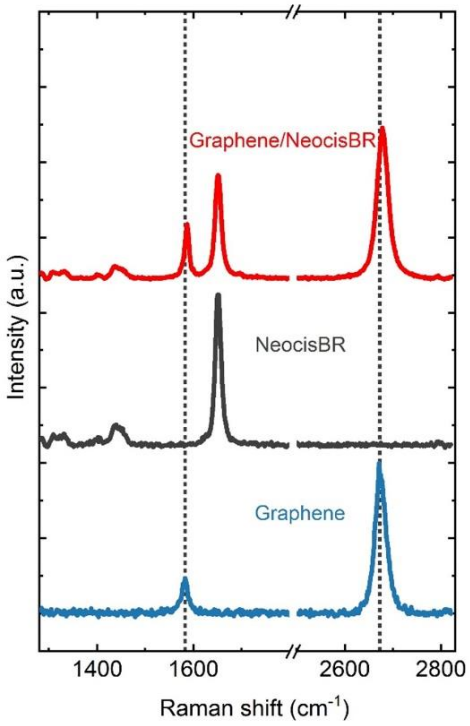

Figure 6.2. Depicting the Raman spectra of graphene on Si/SiO_2, NeocisBR and graphene with NeocisBR on top. Raman spectroscopy was performed with a laser of 532 nm of wavelength.

The 2D-peak position in bare graphene was located at ~2674.1 cm^{-1} while the G-peak at ~1582.8 cm^{-1}, originating from second order phonon and C-C bond stretching, respectively.[209] These values agree well with those reported in Table 3.1 of chapter 3 for graphene cleaned with the 2SC approach. The Raman spectra of NeocisBR shows a strong peak at ~1650 cm^{-1}, in agreement with literature.[210] After depositing the NeocisBR on graphene, the 2D-peak and G-peak values were shifted to higher values by ~3 cm^{-1} and ~2.6 cm^{-1} respectively. The shift in the peak positions

towards higher value can be related to the doping occurring in graphene after NeocisBR deposition, which can also be confirmed in figure 6.3a.[211] The FWHM of the 2D is instead found to be very similar before and after deposition of NeocisBR (figure 6.3b), indicating no significant changes in the strain inhomogeneigty distribution within graphene. Finally the decrease In FWHM of G in figure 6.3d is a further indication of the doping effect of the polymer. Other important parameters one can extract from Raman spectra to evaluate doping effects in graphene are the area A_{2D}/A_G and intensity ratios I_{2D}/I_G of 2D and G-peak of graphene.[102] A_{2D}/A_G was initially ~8.3 while after depositing NeocisBR became ~7.2, an indication of doping in graphene (see figure 6.3 (c)). Similarly, for bare graphene the value of I_{2D}/I_G was nearly ~4.7 while after depositing NeocisBR was around ~3.1, ad additional indication of graphene doping upon NeocisBR deposition (see figure 6.3 (e)).[100]

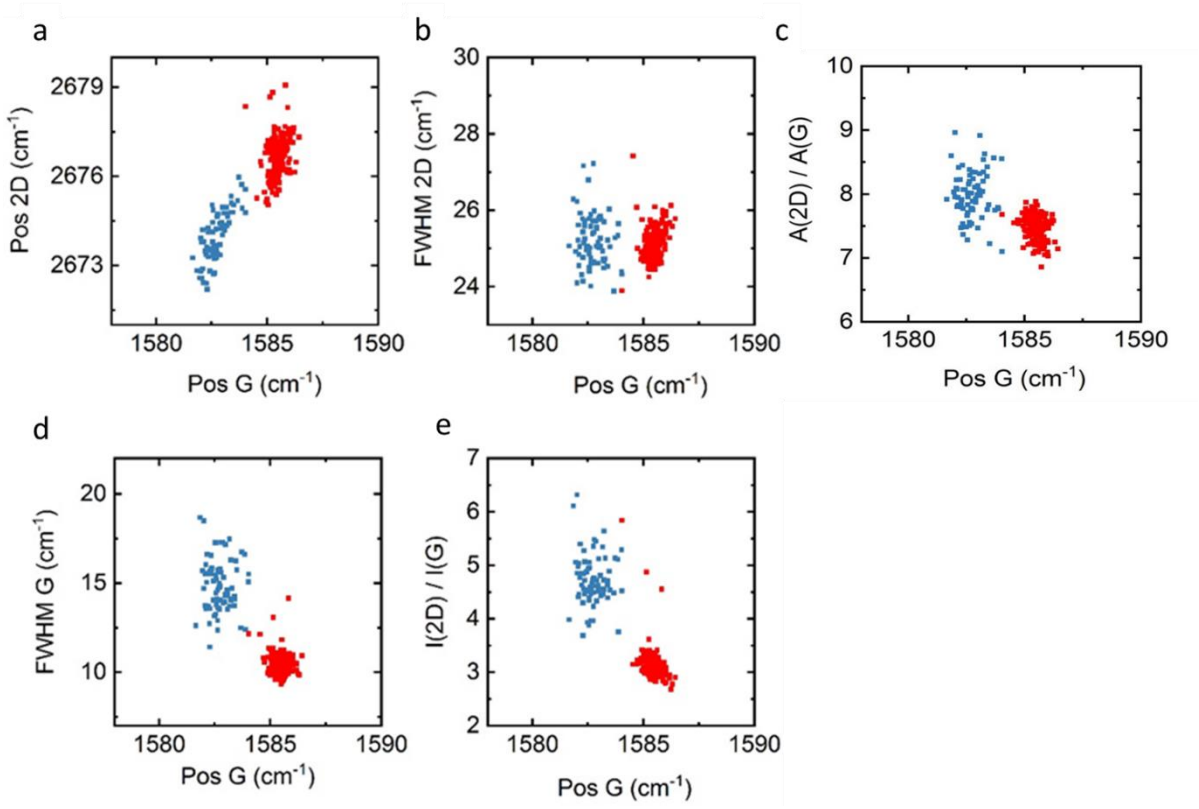

Figure 6.3. Portraying the Raman correlation of (a) Pos(2D) vs Pos(G), (b) FWHM(2D) vs Pos (G), (c) area ratio of 2D and G-peak, (d) FWHM (G) vs Pos (G) and (e) intensity ratio of 2D and

G-peak for bare graphene (blue) and graphene with NeocisBR (red). Raman spectroscopy was performed with a laser of 532 nm of wavelength.

Raman spectroscopy was performed also after depositing a SLR film on graphene (see figure 6.4). The 2D and G-peak position of bare graphene were, again in agreement with Table 3.1 of chapter 3, recorded around ~2675.5 cm^{-1} and ~1583.6 cm^{-1}, respectively. A measurable indication of doping was retrieved in this case as well after depositing SLR on graphene with a shift towards higher values of the 2D and G peaks of ~6.7 cm^{-1} and ~2.8 cm^{-1}, respectively. For SLR, a strong Raman signal around ~1650 cm^{-1} with some other low signals around ~1450 cm^{-1} and ~1300 cm^{-1} was measured, in agreement with literature. [212]

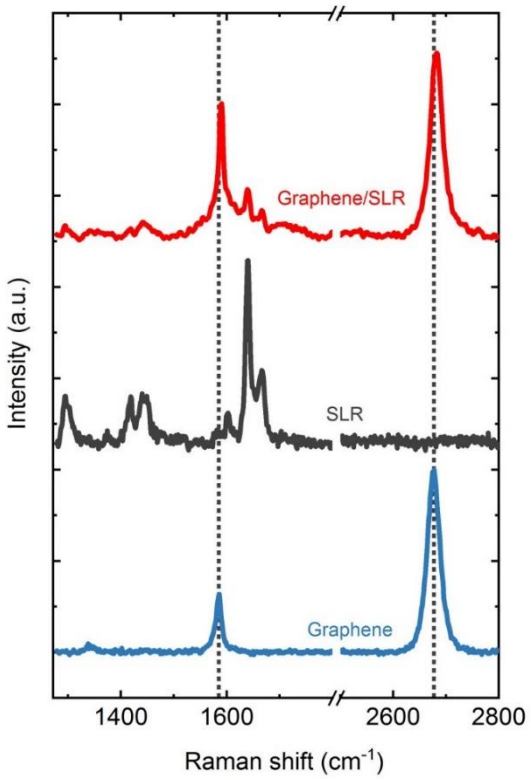

Figure 6.4. Showing the Raman spectra of graphene on Si/SiO_2, SLR, and graphene with SLR deposited on top. Raman spectroscopy was performed with a laser of 532 nm of wavelength.

The relevant ratios A_{2D}/A_G, I_{2D}/I_G, FWHM(G) and FWHM(2D) showed also a similar behavior to those measured for NeocisBR. The value of A_{2D}/A_G was around ~6.8 for bare graphene and later reached ~3.7 after SLR deposition while the I_{2D}/I_G was initially ~3.3 and later decreased to

~2 as shown in figure 6.5. Again, the FWHM of the 2D peak was found not to change after deposition of SLR, while the FWHM of the G peak inreased.

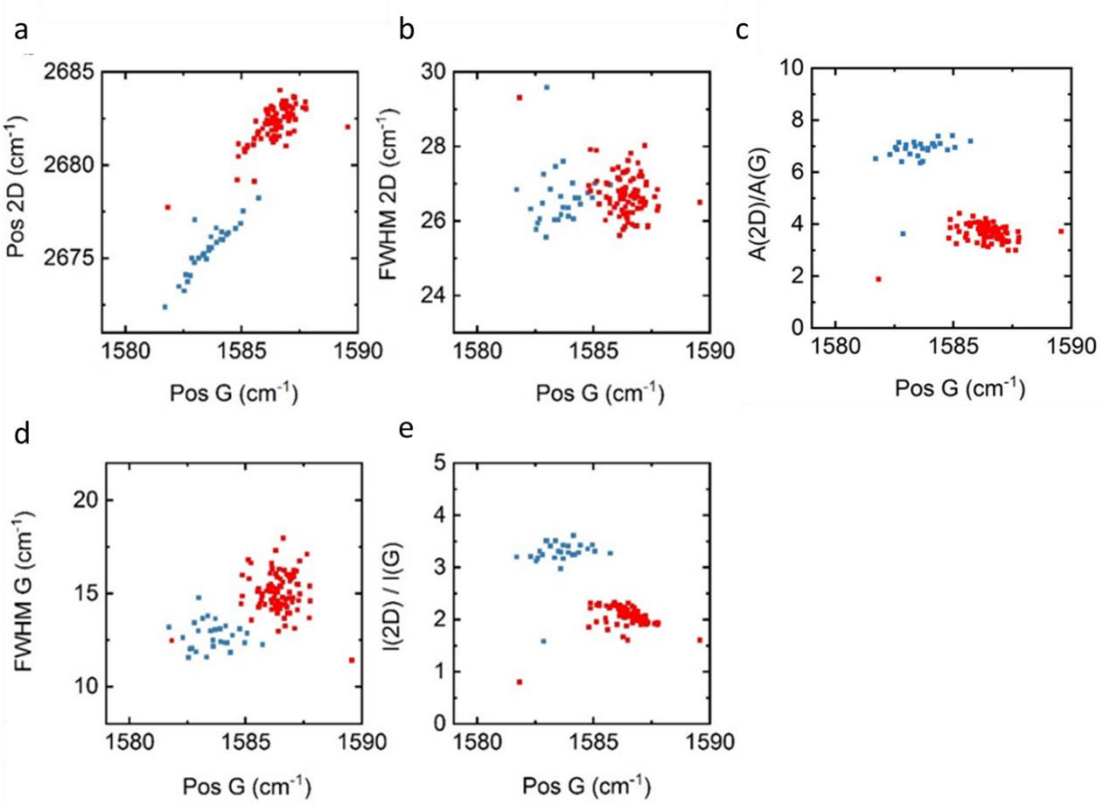

Figure 6.5. Portraying the Raman correlation of (a) Pos(2D) vs Pos(G), (b) FWHM(2D) vs Pos (G), (c) area ratio of 2D and G-peak, (d) FWHM (G) vs Pos (G) and (e) intensity ratio of 2D and G-peak for bare graphene (blue) and graphene with SLR (red). Raman spectroscopy was performed with a laser of 532 nm of wavelength.

Notably, no graphene D-peak was observed upon deposition of both NeocisBR and SLR confirming that there was no defect formation in graphene after deposition of these thin layers, and therefore no covalent functionalization. In conclusion, Raman analyses show that SLR and NeocisBR deposition on graphene induce doping but no structural modification.

6.2.3 Electrical properties of graphene interfaced with rubbers

While Raman can only provide a qualitative indication of SLR/graphene and NeocisBR/graphene doping, electrical measurements can provide a quantitative evaluation. For this purpose, we have

fabricated graphene based FETs by using EBL, and performed electrical measurements in four-probe configuration. Figure 6.6 is depicting the optical image of a typical graphene FET realized for this purpose (panel (a)), together with a sketch of the electric field measurement configuration (panel (b)).

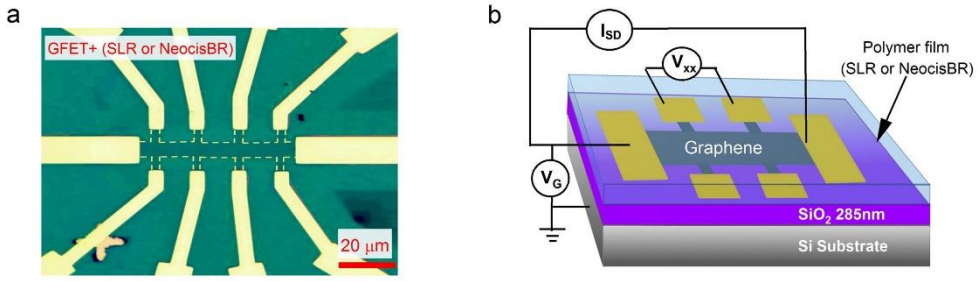

Figure 6.6. Optical image of graphene FET covered with polymer (NeocisBR or SLR); (b) schematics of back gated graphene FET device.

Initially, the field effect measurement was performed on a FET device fabricated on bare graphene and the CNP value was observed to be around 2.2 V, further confirming that graphene after 2SC is very much electrically neutral. After coating the device with a thin layer of NeocisBR, the CNP reached 15.26 V, as shown in figure 6.7 (a). Similarly, after SLR deposition the CNP reached 29.67 V (shifting from an initial 13.4 V measured for the bare graphene device) as depicted in figure 6.7 (b). The CNP shift measured after rubber deposition is indicative in both cases of graphene p-type doping [213].

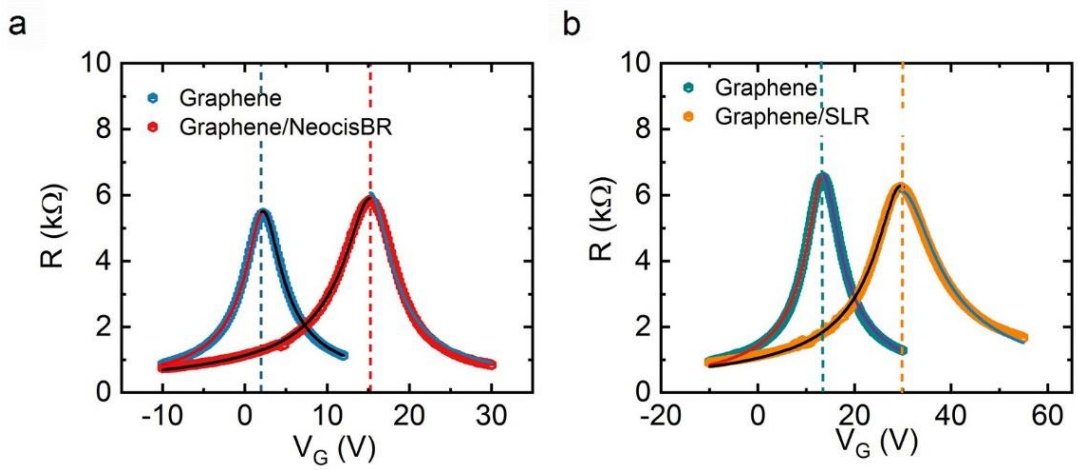

Figure 6.7. Showing resistance curve as function of applied back gate voltage (a) before and after NeocisBR deposition, (b) before and after SLR deposition.

In particular, both hole and electron mobility values were found to decrease after deposition of NeocisBR and SLR. The average mobility of pristine graphene was measured to be around ~ 8000 $cm^2V^{-1}s^{-1}$ (~ 7750 $cm^2V^{-1}s^{-1}$) and was reduced down to ~ 4200 $cm^2V^{-1}s^{-1}$ (~ 3300 $cm^2V^{-1}s^{-1}$) after NeocisBR (SLR) deposition. The reason behind the reduction in mobility is likely related to the charge carrier scattering induced by the interaction between the rubber layer and graphene. Nonetheless, no obvious change in the resistivity of the graphene is observed after interfacing it with both rubbers.

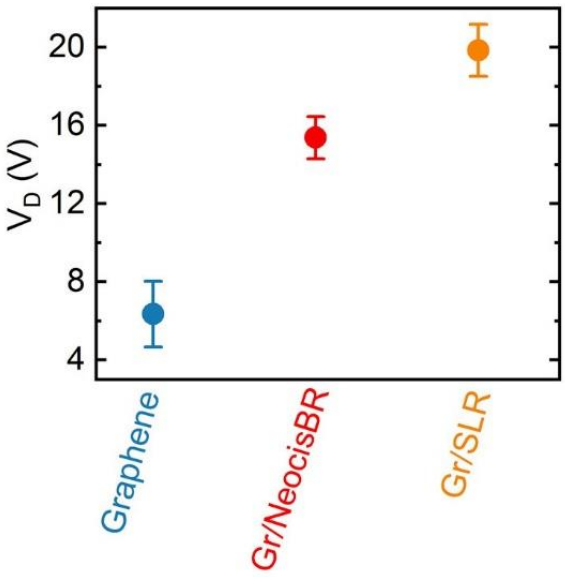

Figure 6.8. Displaying CNP evolution of graphene after deposition of SLR and NeocisBR.

The reported behavior was confirmed by fabricating 10 different devices. Also in this case a similar shift was observed in CNP values after SLR and NeocisBR depositions as shown in figure 6.8. In conclusion, it is evident from both Raman and electrical measurements that graphene upon deposition of SLR and NeocisBR displays increased doping while structurally no damage is observed.

6.3 Graphene functionalization with heterocyclic molecules

After investigating the effect of rubbers at nanoscale on graphene properties, the next step was to identify a molecule which can be produced through a sustainable and eco-friendly approach and used to functionalize graphene to improve dispersion of graphene in rubber blends. Nitrogen containing compounds are very widespread in nature and, among them, particularly suitable for tire applications are pyrrole and tetrazole based molecules.

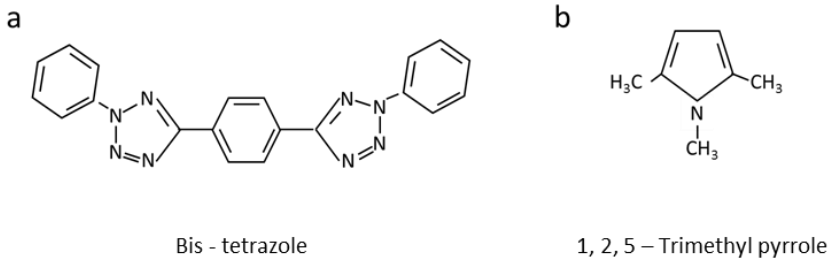

Figure 6.9. (a) and (b) are represent the chemical structure of bis-tetrazole and 1, 2, 5 – Trymethyl pyrrole.

For this thesis work we have investigated the functionalization of graphene with bis-tetrazole and 1, 2, 5 – Trymethyl pyrrole (TMP) are shown in figure 6.9. The characterization of funonalized graphene with Raman spectroscopy and electrical measurements as explained in the next sections.

6.3.1 Raman analysis of graphene functionalized with pyrroles

Initially, the effect of TMP functionalization on graphene was investigated. Graphene was grown on Cu foils and transferred on Si/SiO_2 substrates as done in the rest of the thesis prior to the functionalization. Pyrrole molecules were dissolved in THF (at 0.1nM, 3mM, 9mM and > 9mM concentration) and then deposited on graphene by drop casting and annealed in vacuum at different temperatures (i.e., 150°C, 170°C and at 190°C) from 30 minute to 3 hours. [208] Vacuum was required to avoid graphene damage that instead was observed when performing such a process in air. In fact, in air, most of the CVD graphene crystals present on SiO_2 were damaged as could be observed by optical microscopy and confirmed by Raman spectroscopy as shown in figure 6.10. Raman spectroscopy performed on graphene heated with pyrroles in vacuum, revealed a little shift in the G-peak position of nearly ~10 cm^{-1}, and a lower I_{2D}/I_G ratio, both indicating doping in

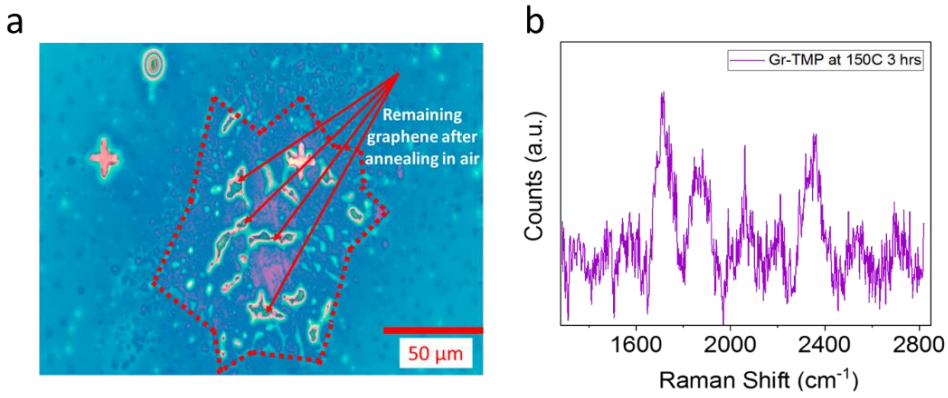

Figure 6.10. (a) Optical image showing the damaged graphene crystal when functionalized with TMP in air, (b) Raman spectra of remaining graphene/TMP with laser of wavelength 532 nm.

graphene probably due to charge transfer between graphene and pyrrole as can be seen in figure 6.11. However, no detectable D-peak was observed, indicating that no covalent functionalization of graphene was achieved. No significant differences were observed in the Raman spectra for different concentrations of TMP or different annealing temperature or time. During preliminary experiments, we also adopted graphene grown on sapphire, where the interaction with the growth substrate is expected to be stronger (with respect to graphene transferred on SiO_2/Si).

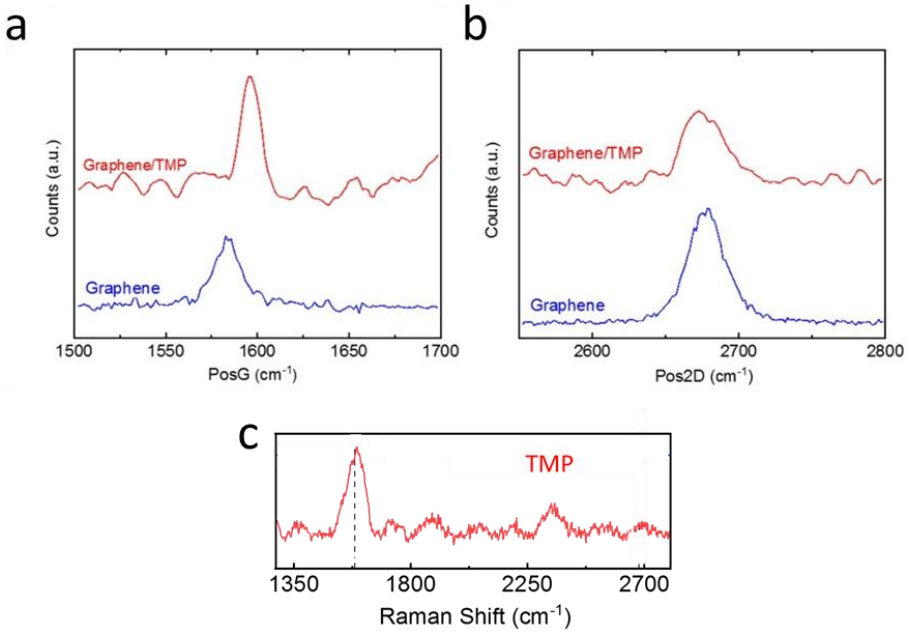

Figure 6.11. (a) Raman spectra in the range of the G-peak, (b) 2D-peak of graphene before and after functionalization with TMP and (c) Raman spectra of TMP with laser of wavelength 532 nm.

Yet, after attempting pyrrole functionalization with the same process as that described above, similar results were obtained. Additionally, Raman spectrosocopy was also performed to evaluate the effect of the solvent (THF) deposited on graphene while annealing at 170°C for 3 hours to get an impression of any possible covalent functionalization or doping. However, as can be seen from figure 6.12, THF does not induce any doping or structural modification effect on graphene.

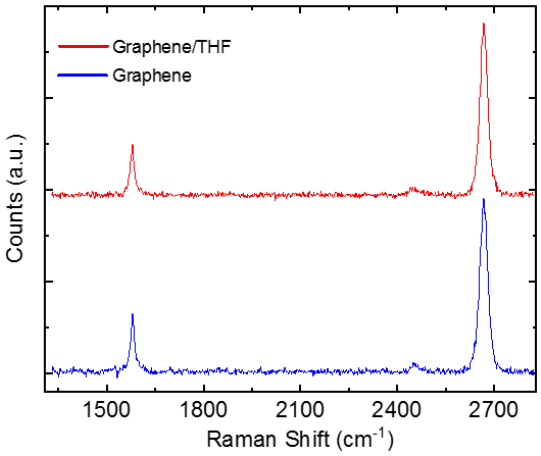

Figure 6.12. Raman spectra of graphene before and after THF measured with laser of wavelength 532 nm.

To stimulate covalent functionalization, pristine graphene grown on Cu and not transferred was also adopted and cyclic voltammetry (CV) attempted. Graphene on Cu was immersed within a pyrrole solution (5Mm) where NMP was used as solvent. Yet, Raman analysis revealed that the TMP molecules were binding to the uncovered Cu areas rather than to graphene (see figure 6.13). Even by adopting CV no covalent functionalization was observed. As covalent functionalization of graphene would be highly desirable to improve the properties of the final blend in tire applications, those results were not seen as encouraging. Yet, one might have to consider that we are attempting to functionalize a nearly perfect crystalline structure with very few edges with respect to the planar area. This assumption is confirmed by STM studies of our material, Raman analysis (absence of D peak among other features) and the extremely high mobility measured on our CVD samples [72,155], signifying very high crystallinity.

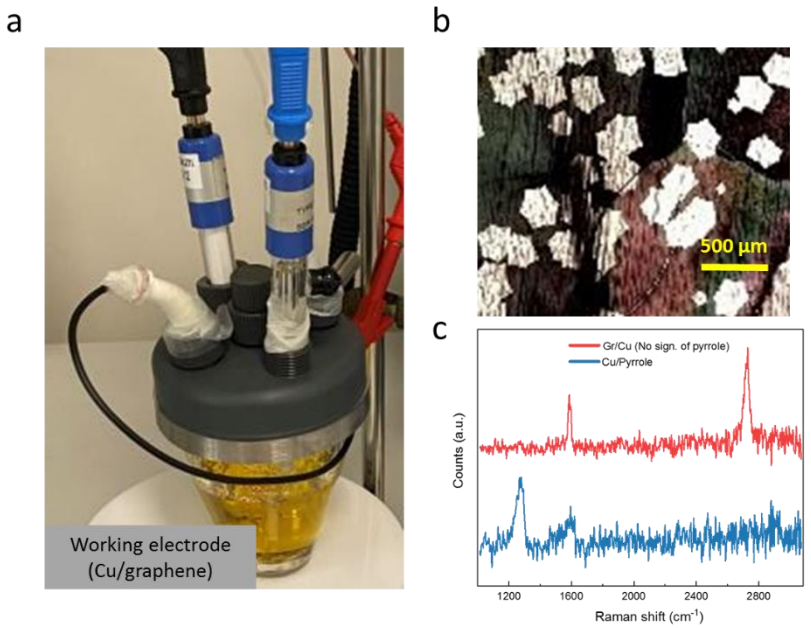

Figure 6.13. (a) Picture of the CV apparathus used for functionalization, (b) optical image of Cu/graphene/TMP after performing CV and (c) Raman spectra measured on Cu and Cu/graphene indicating presence of TMP only on the Cu area.

The absence of preferential binding sites where covalent functionalization shall take place is hence a characteristic of the used material. On the other side, by using graphene inks the number of sites for covalent functionalization (i.e., edges, defects) shall significantly increase.

6.3.2 Raman and electrical analysis of graphene functionalized with tetrazole

Out of the different tetrazole molecules available, we have adopted bis-tetrazole for these experiments, which has already shown potential for graphene functionalization in literature. The process adopted was similar to the one developed for pyrroles: bis-tetrazole was dissolved in THF at concentrations varying from 5mM to 10 mM and drop casted on graphene, then annealed in vacuum at 170°C for 3 hours. In figure 6.14, the Raman spectra of graphene and graphene functionalized with 5mM tetrazole molecule is depicted. Interestingly, upon tetrazole functionalization, the emergence of graphene D-peak around 1345 cm^{-1} was observed in some specific locations (see figure 6.14). A Raman map of I_D/I_G after graphene functionalization is reported in figure 6.15, which clearly shows the spatial localization of the defects.

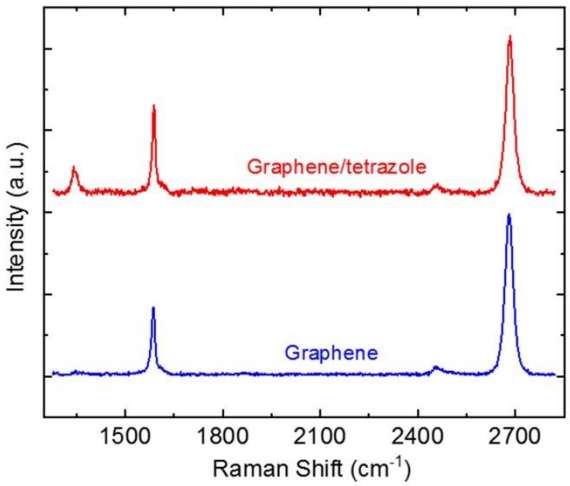

Figure 6.14. Raman spectra of graphene before and after functionalization with tetrazole. Measurement taken with laser of wavelength 532 nm.

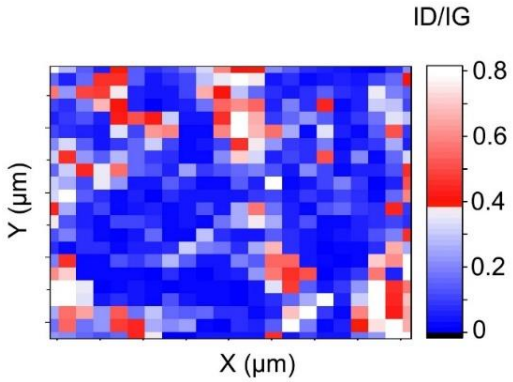

Figure 6.15. Raman map of 10×10 μm^2 showing the intensity ratio of D and G peaks after functionalizing graphene with bis-tetrazoles. Measurement taken with laser of wavelength 532 nm.

To better shed light on this finding, which were obtained with a first batch of graphene samples, additional graphene samples were functionalized with bis-tetrazole in the same way as described above. However, in none of the second batch of samples Raman analysis revealed the occurrence of a D peak. Knowing that after some transfer processes we had observed some residual Cu coming from the original growth substrate on our graphene we hence started to weight the possibility that Cu contamination present in the first batch of transferred graphene might lead to the presence of ions acting as coordination centers for tetrazole binding.[214,215]

Hence, to probe whether Cu ions could be responsible for the observed local covalent functionalization, we used a copper (II) chloride ($CuCl_2$) mixture with tetrazole with THF as solvent (10mM) and used it to functionalized graphene with the standard process reported above.

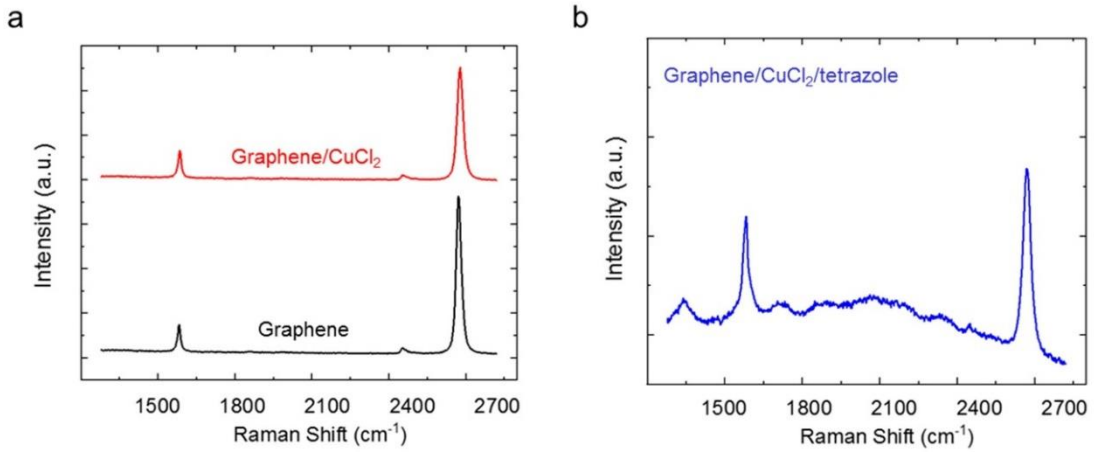

Figure 6.16. Raman spectra of (a) graphene and graphene/$CuCl_2$; (b) graphene after functionalization with $CuCl_2$/tetrazole.

Indeed, the copper (II) chloride alone does not appear to create defects in graphene when deposited at 170°C for 3 minutes in vacuum (see red line in figure 6.16(a)). However, when tetrazole is mixed in and functionalization is performed at the same experimental conditions, the collected Raman spectra reveal a clear D peak (figure 6.16(b)).

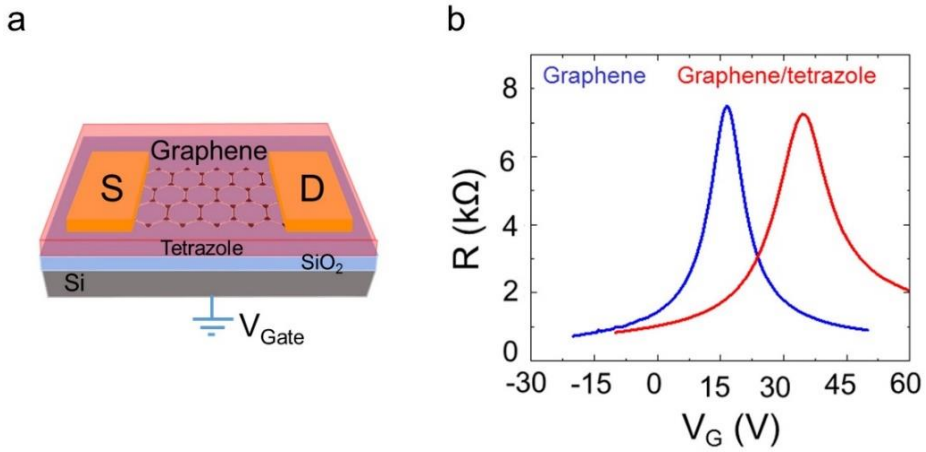

Figure 6.17. (a) Schematics of GFET with tetrazole functionalization; (b) resistance vs applied back gate voltage for graphene and tetrazole functionalized graphene.

We also performed field effect measurement on GFET before and after functionalization with bis-tetrazole. These measurements were performed for the samples where no covalent functionalization was observed. As shown in figure 6.17, the CNP value of bare graphene was around ~18 V while after functionalizing the same sample with tetrazole, the CNP value reached nearly ~38 V. The positive shift in CNP value of graphene is related to the doping coming from tetrazole as a consequence of charge transfer. As the functionalization experiment was performed under vacuum, the possibility of graphene doping from ambient, previously reported [216], is very low. The mobility of bare graphene calculated with the Drude model at a carrier density of 1×10^{12} cm^{-2}, was initially around ~ 6200 $cm^2V^{-1}s^{-1}$ for holes and nearly ~ 5800 $cm^2V^{-1}s^{-1}$ for electrons. After functionalization with tetrazole both the hole and electron mobility values were reduced to ~ 4900 $cm^2V^{-1}s^{-1}$ and ~ 2900 $cm^2V^{-1}s^{-1}$ respectively as shown in figure 6.18.

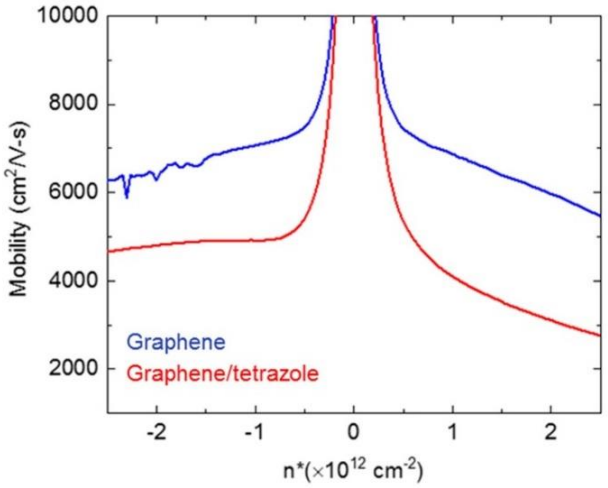

Figure 6.18. Displaying electron and hole mobility of graphene before and after functionalization with tetrazole.

The reduction in graphene mobility values can be attributed to the charge carrier scattering after functionalization.[121] In conclusion, our functionalization attempts of CVD graphene with tetrazole molecules indicate that most likely covalent functionalization is only achieved when Cu ions (leftover from the transfer process on graphene) act as a coordination centers for tetrazole attachment.[215] Yet, it should be noted that the graphene adopted in these experiments does not offer preferential binding locations such as instead the graphene oxide adopted in [217] where the starting amount of defects and active edges is significantly higher as also demonstrated by Raman

analysis. For this reason we proceeded by attempting graphene ink functionalization with tetrazoles as described in the next section.

6.3.3 Graphene ink functionalized with tetrazole

Graphene inks present sp^3 carbon bonds, which offer preferential binding locations helping to initiate covalent functionalization.[218] Here, the impact of tetrazole was investigated on few-layer graphene-based inks obtained from BeDimensional (G-Leaf conductive inks). Few-layers graphene was suspended in DMF by sonicating the ink in the solvent for 15 minutes. A small amount of this suspension was drop casted on SiO_2/Si substrate and dried for further characterization. Figure 6.19 (a), displays the optical image of few-layer graphene deposited on SiO_2/Si substrate and the relative 10×10 μm^2 Raman map of the D-peak intensity.

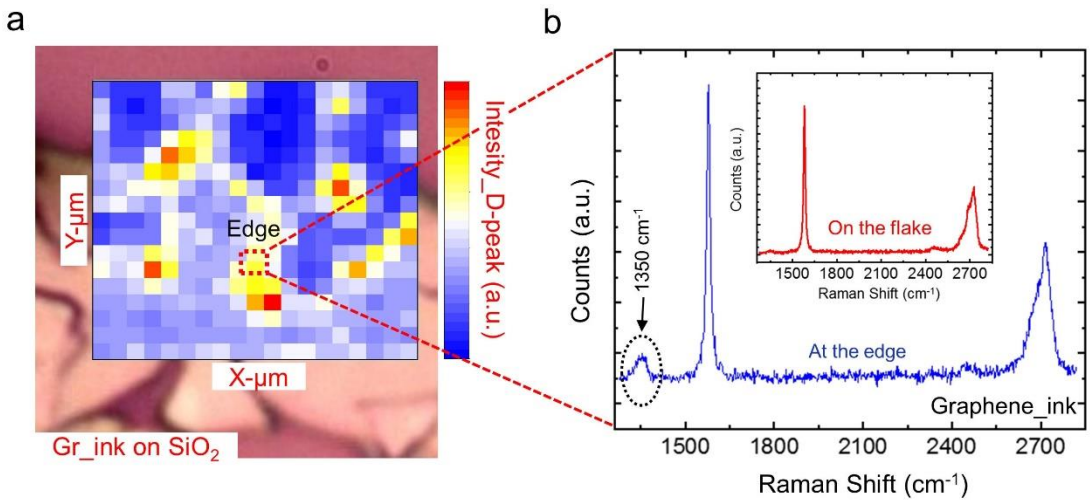

Figure 6.19. (a) Optical image of few-layer graphene ink deposited on SiO_2/Si substrate superimposed with a 10×10 μm^2 Raman map (0.5 µm step size) of the D-peak intensity; (b) Raman spectra of few-layer graphene flakes at the edge and at the center (shown in the inset).

Figure 6.19 (b) reports the Raman spectra of the graphene ink measured at the edge of a flake and at the center of it (the latter in the inset). As expected, at the edges of the flake sp3-bonds are evidenced by the presence of a D-peak (~ 1350 cm^{-1}).[219] The average value of I_D/I_G was found to be ≤ 0.2.[219] Moreover, at the center of the few layer graphene, no defect peak was observed indicating edge defect domination. These Raman spectra were later considered as a reference for further experiment with tetrazole functionalization.

To implement tetrazole functionalization, a suspended solution of graphene and tetrazole with 2:1 ratio was sonicated in DMF for 15 minutes and subsequently heated at 170°C for 3 hours in nitrogen atmosphere with low vacuum. The solution was then centrifuged at 12000 rpm for 5 minutes followed by 3 times DMF and acetone washing. Afterwards, the mixture was drop casted on the SiO_2/Si substrate and dried in vacuum.

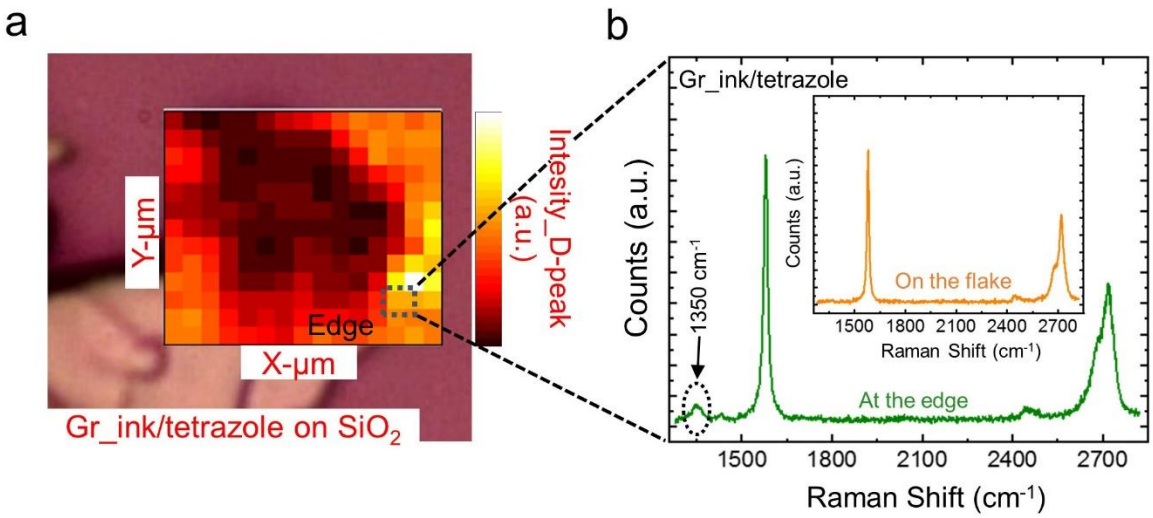

Figure 6.20. (a) Optical image of few-layer graphene ink functionalized with tetrazole with superimposed a 14×14 µm^2 Raman map of the D-peak intensity; (b) Raman spectra of a few-layer graphene flake at the edge and at the center (shown in the inset).

In figure 6.20, we report representative Raman spectra and D-peak map measured after the functionalization attempt with tetrazoles. No D-peak was observed at the center of the flakes, indicating that no covalent functionalization was achieved. At the edges of the flake D-peaks were observed. However, when comparing the I_D/I_G ratio measured for multiple maps after functionalization (averaging ≤ 0.1) with that measured before (averaging ≤ 0.2) we observed a general reduction of the value. The possible reason for the measured reduction could be defect healing, as tetrazole molecules are rich in C-atoms and might be filling the vacancies at the graphene edges. Overall, three samples of graphene ink were functionalized with tetrazole, yielding consistent results as those reported above (see figure 6.21). No significant changes were measured for the G and 2D peak positions. From the evidence above we hence hypothesize a simultaneous covalent functionalization and reduction of graphene layers at the edges with a small amount of tetrazole molecules, in agreement with literature reports.[220]

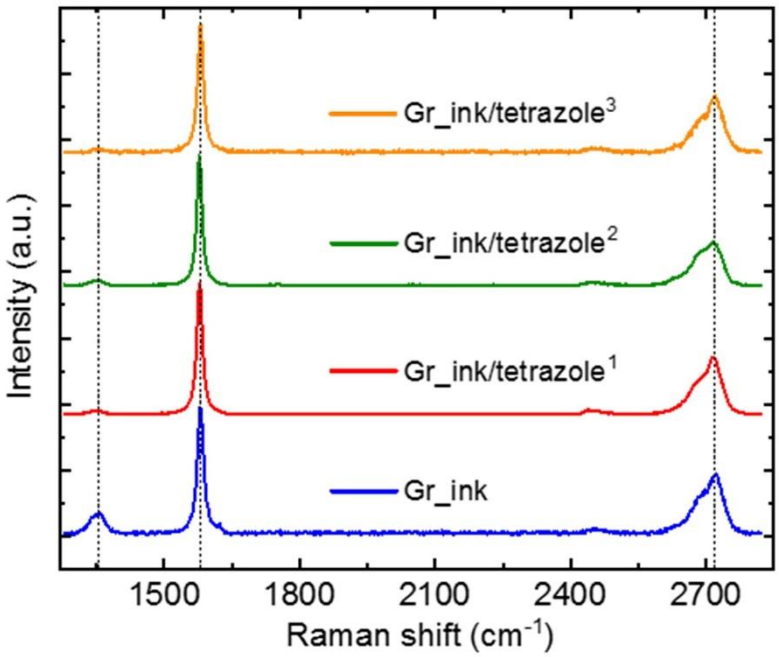

Figure 6.21. Raman spectra of a pristine graphene ink deposited on SiO2/Si and of three different tetrazole functionalized graphene ink on SiO_2/Si substrates. D-peak reduction is observed in each of the tetrazole-functionalized samples.

6.3.4 Graphene ink functionalized with tetrazole with Cu as catalyst

As a final experiment, a similar approach was followed as in the case of CVD graphene, by using Cu ions as catalysts to promote covalent functionalization of graphene inks with tetrazoles. A mixture of graphene ink, tetrazole and $CuCl_2$ with DMF was sonicated and dispersed in similar way as for graphene ink and tetrazole with a ratio of 2:1:1 respectively. As shown in figure 6.22, when few-layers of graphene were functionalized with tetrazole/$CuCl_2$, a clear change in the D-peak intensity was observed. Moreover, the I_D/I_G ratio was increased on average from ≤ 0.2 to ≤ 0.9, which confirms the formation of covalent bonding between graphene and tetrazole (most likely with Cu ions acting as coordination centers). Furthermore, a shift towards lower wavenumbers in the position of the G-peak is compatible with functionalization induced doping (see figure 6.22). Ultimately, these results well agree with those obtained for $CuCl_2$/tetrazole functionalized CVD graphene.

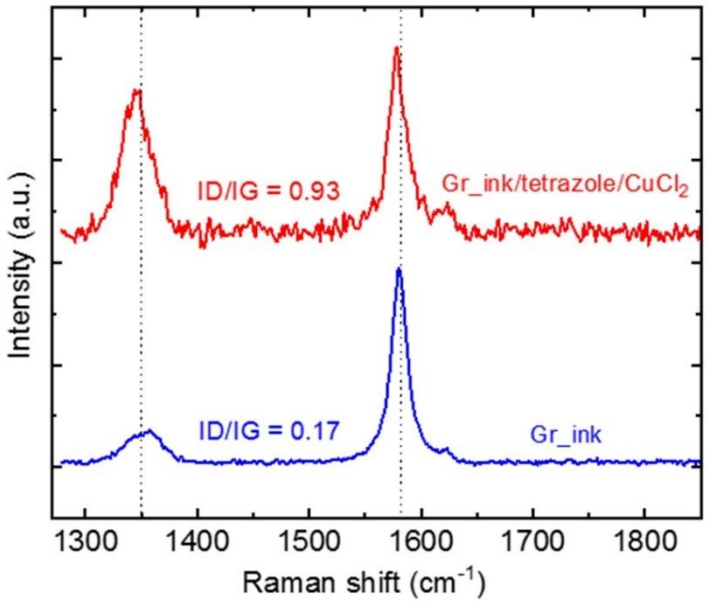

Figure 6.22. Raman spectra of graphene ink and graphene ink functionalized with tetrazole/$CuCl_2$.

6.4 Conclusions

In this final chapter, we have explored the interaction of rubbers and molecules of interest for tire applications with graphene. Concerning rubbers such as NeocisBR and SLR, it was found that they did not alter the graphene structure or properties apart from a slight hole doping, which was confirmed by Raman spectroscopy and electrical transport studies. Furthermore, due to the challenges of obtaining a homogenous graphene dispersion in rubber blends for tire applications, an approach to functionalize graphene with functional eco-friendly molecules was attempted. Two different molecules, trimethyl-pyrrole and bis-tetrazole were used to functionalized CVD graphene and the results were investigated with Raman spectroscopy and electrical measurement. Both the molecules did not show any sign of strong covalent binding to graphene, under different conditions and also when using different types of graphene (CVD on Cu, transferred CVD, CVD on sapphire) as shown in the summary table 6.1 and table 6.2. Yet, for bis-tetrazole local D-peak was found to emerge in the Raman spectrum, possibly indicating some local covalent bonding. Control experiments allowed us to associate these findings with the presence of residual Cu from the growth substrate acting as a coordination center for binding graphene and tetrazole. In fact, when graphene was functionalized with tetrazole/$CuCl_2$ covalent functionalization was confirmed by Raman spectroscopy.

Table 6.1 Graphene functionalization with pyrrole summary.

Approach	Drop casting (0.1nM, 3mM, 9mM and > 9mM) (Graphene on Sapphire, Cu and SiO_2 in IPA, Toluene) (heating in air and vacuum)	Cyclic Voltammetry (N_2 environment, in 0.5M HCl) (Graphene on Cu)	Defect creation and drop casting (Graphene on sapphire and SiO_2)	Immersion in Pyrrole/N-methyl-pyrrolidone (N_2 environment at 150°C, 3 hours) (Graphene on Cu, Sapphire and SiO_2)
Effect	No doping and functionalization occurred (graphene damaging above 9mM and air annealing)	Pyrrole attachment only on Cu no change in graphene	No change even in defected graphene	No functionalization on sapphire and Cu without damage while on SiO_2 graphene was detached

Table 6.2 Graphene functionalization with tetrazole summary.

Approach	Drop casting (5mM and 10mM) (graphene on SiO_2 in tetrazole/THF) (heating in vacuum)	Drop casting (10mM) (graphene on SiO_2 in tetrazole/$CuCl_2$/THF)
Effect	Randomly distributed D-peak were observed (due to residual Cu from growth substrate)	A clear D-peak was observed

CVD graphene represent an ideal model system where defective sites as well as edges are reduced to a minimum, and hence the results above are indicative of the difficulty of inducing covalent functionalization of graphene with the used molecules and at the attempted conditions. Furthermore, from a realistic point of view, functionalization of graphene inks with tetrazole was attempted. Graphene inks possess inherent defective sites at least at the edges. Yet, we observed via Raman spectroscopy defect reduction possibly as a consequent of defect healing, in agreement

with what reported in [220]. Finally, graphene inks were functionalized with tetrazole/$CuCl_2$. This attempt was successful since Raman analysis indicated a strong increase in the D-peak thus further confirming the role of Cu in promoting graphene functionalization with tetrazole. However, since Cu is not a chemical element of choice for tire applications, other solutions shall be identified for functionalizing graphene/rubber blends.

Chapter 7: Summary and outlook

Being a wonder material with exceptional properties, graphene is becoming an optimal candidate for future industrial application, especially within the automotive industry. The main goal behind this thesis was to investigate the potential of graphene for different applications in the automotive industry ranging from magnetic sensing, to light sensing and green tire technology.

As a starting point for the rest of the work, we show that it is possible to achieve ultraclean and high-mobility scalable CVD graphene on technologically relevant substrates. We report, following a tailored graphene cleaning approach, a mobility of nearly ~ 9000 $cm^2V^{-1}s^{-1}$ with low residual carrier density of ~ 1.45×10^{11} cm^{-2} and almost strain-free and flat graphene on SiO_2. The reported cleaning approach indicates a straightforward route for the achievement of high-mobility scalable graphene devices which are sought after by several electronic, optoelectronic and photonic applications.

Additionally, apart from scalability and high quality, stability of graphene based devices is a key element to be achieved for its integration in different technologies, especially for magnetic field detection purposes. For this purpose, we have demonstrated a facile and scalable method to fabricate highly-sensitive air-stable CVD graphene-based Hall sensors through a simple fabrication method. A state-of-the-art current related sensitivity of ~ 5030 V/AT with carrier mobility exceeding 10^4 cm^2 V^{-1} s^{-1} and low charge inhomogeneity at the charge neutrality point (CNP) n* ~$1x10^{11}$ cm^{-2} were retrieved. The stability in the overall performance of the Hall sensors was achieved due to a facile and scalable encapsulation of the devices with a polymeric (PMMA) layer. These capped Hall sensors displayed stable electrical behavior (i.e. low hysteresis <1 V) even when measured in ambient conditions. Furthermore, PMMA capping was instrumental to slow down the degradation of device performance even when stored in air for prolonged times (up to 10 weeks). These are all relevant aspects for a realistic graphene integration in Hall sensing applications. To further proceed in this direction, bi-polymeric layers or a proper enclosure of the Hall sensors devices already capped with PMMA, should be further investigated. Our work ultimately demonstrates that monocrystalline CVD graphene on Si/SiO_2 can be a viable material for the scalable production of Hall sensors whose performance exceed those fabricated using conventional technology.

Furthermore, in this thesis the possibility to adopt graphene to realize visible light sensors was addressed. Light sensors are of interest in vehicle to vehicle communication, especially for future self-driven automatic vehicles. We have developed sensitive, scalable, and self-powered graphene based visible light photodetectors. A facile and reproducible approach was demonstrated to fabricate semi-encapsulated, ambient-stable graphene-based pn-junction devices by using e-beam lithography. The photodetectors displayed a measured photocurrent of ~ 120 nA and a reasonable responsivity of ~ 18 μA/W with response time of ~ 197 ms at 532 nm of wavelength laser with 12 mW of power. The photoresponse in our graphene pn-junctions was assigned to the photovoltaic effect. The reporteds results represent a first step, and further experiments and optimization in the fabrication procedure are needed to improve the photodetection performance of such devices to move towards the adoption of graphene for visible light sensing.

Finally, studies were devoted to understand the interaction between rubbers and graphene and its functionalization in such systems, with an outlook of its adoption in the tire industry. Initially, the impact of different rubbers was investigated on the properties of CVD graphene, and it was found that normally adopted rubbers hole dope graphene. Furthermore, since a major challenge to include graphene in rubber matrixes for tires is its poor dispersion, graphene functionalization approaches were tested. Nitrogen rich molecules (pyrroles and tetrazoles) that can be obtained with eco-friendly approaches were investigated as possible functionalization agents. However, we found that CVD graphene cannot be covalent functionalized with such molecules under a wide range of experimental conditions, probably due to the absence of active binding sites. To overcome this challenge, we attempted functionalization of graphene inks, which typically present more defective sites that shall facilitate covalent functionalization. However, we found that graphene inks display a low amount of covalent binding with tetrazole molecules and a simultaneous reduction of graphene due to defect healing. We observed that when adopting Cu rich chemistries instead, covalent functionalization of both CVD graphene and graphene inks with tetrazole was achieved (with Cu acting as coordination center). In the future, different functionalization approaches (including other green heterocyclic molecules) need to be tested. By demonstrating for the first time the effect that rubbers have on the electrical properties of graphene, and investigating the low reactivity of graphene to the tested tetrazole and pyrroles, our study provide novel information that could be of interest to better understand the behavior of graphene/rubber blends.

Bibliography

[1] Liu Y, Huang Y and Duan X 2019 Van der Waals integration before and beyond two-dimensional materials *Nature* **567** 323–33

[2] Novoselov K S, Mishchenko A, Carvalho A and Castro Neto A H 2016 2D materials and van der Waals heterostructures *Science (80-.).* **353**

[3] Wallace P R 1947 The Band Theory of Graphite *Phys. Rev.* **71** 622–34

[4] K. S. Novoselov et al 2004 Electric Field Effect in Atomically Thin Carbon Films **306** 666–9

[5] Berry V 2013 Impermeability of graphene and its applications *Carbon N. Y.* **62** 1–10

[6] Soldano C, Mahmood A and Dujardin E 2010 Production, properties and potential of graphene *Carbon N. Y.* **48** 2127–50

[7] Banszerus L, Schmitz M, Engels S, Goldsche M, Watanabe K, Taniguchi T, Beschoten B and Stampfer C 2016 Ballistic Transport Exceeding 28 μm in CVD Grown Graphene *Nano Lett.* **16** 1387–91

[8] Liao L and Duan X 2012 Graphene for radio frequency electronics *Mater. Today* **15** 328–38

[9] Collomb D and Li P 2021 Frontiers of graphene-based Hall-effect sensors

[10] Bonaccorso F, Sun Z, Hasan T and Ferrari A C 2010 Graphene photonics and optoelectronics *Nat. Photonics* **4** 611–22

[11] Liu M, Yin X, Ulin-Avila E, Geng B, Zentgraf T, Ju L, Wang F and Zhang X 2011 A graphene-based broadband optical modulator *Nature* **474** 64–7

[12] Papageorgiou D G, Kinloch I A and Young R J 2017 Mechanical properties of graphene and graphene-based nanocomposites *Prog. Mater. Sci.* **90** 75–127

[13] Lee C, Wei X, Kysar J W and Hone J 2008 Measurement of the Elastic Properties and

Intrinsic Strength of Monolayer Graphene *Science (80-.).* **321** 385–8

[14] Balandin A A, Ghosh S, Bao W, Calizo I, Teweldebrhan D, Miao F and Lau C N 2008 Superior thermal conductivity of single-layer graphene *Nano Lett.* **8** 902–7

[15] Renteria J D, Nika D L and Balandin A A 2014 Graphene thermal properties: Applications in thermal management and energy storage *Appl. Sci.* **4** 525–47

[16] Yi M and Shen Z 2015 A review on mechanical exfoliation for the scalable production of graphene *J. Mater. Chem. A* **3** 11700–15

[17] Li Z, Young R J, Backes C, Zhao W, Zhang X, Zhukov A A, Tillotson E, Conlan A P, Ding F, Haigh S J, Novoselov K S and Coleman J N 2020 Mechanisms of Liquid-Phase Exfoliation for the Production of Graphene *ACS Nano* **14** 10976–85

[18] Norimatsu W and Kusunoki M 2014 Epitaxial graphene on SiC{0001}: Advances and perspectives *Phys. Chem. Chem. Phys.* **16** 3501–11

[19] Liu F, Li P, An H, Peng P, McLean B and Ding F 2022 Achievements and Challenges of Graphene Chemical Vapor Deposition Growth *Adv. Funct. Mater.* **2203191** 1–20

[20] Whitener K E and Sheehan P E 2014 Graphene synthesis *Diam. Relat. Mater.* **46** 25–34

[21] Bonaccorso F, Lombardo A, Hasan T, Sun Z, Colombo L and Ferrari A C 2012 Production and processing of graphene and 2d crystals *Mater. Today* **15** 564–89

[22] Mayorov A S, Gorbachev R V., Morozov S V., Britnell L, Jalil R, Ponomarenko L A, Blake P, Novoselov K S, Watanabe K, Taniguchi T and Geim A K 2011 Micrometer-scale ballistic transport in encapsulated graphene at room temperature *Nano Lett.* **11** 2396–9

[23] Hernandez Y, Nicolosi V, Lotya M, Blighe F M, Sun Z, De S, McGovern I T, Holland B, Byrne M, Gun'ko Y K, Boland J J, Niraj P, Duesberg G, Krishnamurthy S, Goodhue R, Hutchison J, Scardaci V, Ferrari A C and Coleman J N 2008 High-yield production of graphene by liquid-phase exfoliation of graphite *Nat. Nanotechnol.* **3** 563–8

[24] Berger C, Song Z, Li T, Li X, Ogbazghi A Y, Feng R, Dai Z, Alexei N, Conrad M E H, First P N and De Heer W A 2004 Ultrathin epitaxial graphite: 2D electron gas properties and a route toward graphene-based nanoelectronics *J. Phys. Chem. B* **108** 19912–6

[25] Riedl C, Coletti C and Starke U 2010 Structural and electronic properties of epitaxial Graphene on SiC(0001): A review of growth, characterization, transfer doping and hydrogen intercalation *J. Phys. D. Appl. Phys.* **43**

[26] Coletti C, Emtsev K V., Zakharov A A, Ouisse T, Chaussende D and Starke U 2011 Large area quasi-free standing monolayer graphene on 3C-SiC(111) *Appl. Phys. Lett.* **99** 2012–5

[27] Starke U, Forti S, Emtsev K V. and Coletti C 2012 Engineering the electronic structure of epitaxial graphene by transfer doping and atomic intercalation *MRS Bull.* **37** 1177–86

[28] Motta N, Iacopi F and Coletti C 2017 Growing graphene on semiconductors *Grow. Graphene Semicond. Pan Stanford, New York.*

[29] Coletti C, Riedl C, Lee D S, Krauss B, Patthey L, Von Klitzing K, Smet J H and Starke U 2010 Charge neutrality and band-gap tuning of epitaxial graphene on SiC by molecular doping *Phys. Rev. B - Condens. Matter Mater. Phys.* **81** 1–8

[30] Berger C, Song Z, Li X, Wu X, Brown N, Naud C, Mayou D, Li T, Hass J, Marchenkov A N, Conrad E H, First P N and De Heer W A 2006 Electronic confinement and coherence in patterned epitaxial graphene *Science (80-.).* **312** 1191–6

[31] Tzalenchuk A, Lara-Avila S, Kalaboukhov A, Paolillo S, Syväjärvi M, Yakimova R, Kazakova O, Janssen T J B M, Fal'Ko V and Kubatkin S 2010 Towards a quantum resistance standard based on epitaxial graphene *Nat. Nanotechnol.* **5** 186–9

[32] Li X, Cai W, An J, Kim S, Nah J, Yang D, Piner R, Velamakanni A, Jung I, Tutuc E, Banerjee S K, Colombo L and Ruoff R S 2009 Large-area synthesis of high-quality and uniform graphene films on copper foils *Science (80-.).* **324** 1312–4

[33] Rümmeli M H, Rocha C G, Ortmann F, Ibrahim I, Sevincli H, Börrnert F, Kunstmann J, Bachmatiuk A, Pötschke M, Shiraishi M, Meyyappan M, Büchner B, Roche S and Cuniberti G 2011 Graphene: Piecing it together *Adv. Mater.* **23** 4471–90

[34] Zhang B, Lee W H, Piner R, Kholmanov I, Wu Y, Li H, Ji H and Ruoff R S 2012 Low-temperature chemical vapor deposition growth of graphene from toluene on electropolished copper foils *ACS Nano* **6** 2471–6

[35] Ruan G, Sun Z, Peng Z and Tour J M 2011 Growth of graphene from food, insects, and waste *ACS Nano* **5** 7601–7

[36] Kim K S, Zhao Y, Jang H, Lee S Y, Kim J M, Kim K S, Ahn J H, Kim P, Choi J Y and Hong B H 2009 Large-scale pattern growth of graphene films for stretchable transparent electrodes *Nature* **457** 706–10

[37] Reina A, Jia X, Ho J, Nezich D, Son H, Bulovic V, Dresselhaus M S and Jing K 2009 Large area, few-layer graphene films on arbitrary substrates by chemical vapor deposition *Nano Lett.* **9** 30–5

[38] Li X, Magnuson C W, Venugopal A, An J, Suk J W, Han B, Borysiak M, Cai W, Velamakanni A, Zhu Y, Fu L, Vogel E M, Voelkl E, Colombo L and Ruoff R S 2010 Graphene films with large domain size by a two-step chemical vapor deposition process *Nano Lett.* **10** 4328–34

[39] Sutter P W, Flege J I and Sutter E A 2008 Epitaxial graphene on ruthenium *Nat. Mater.* **7** 406–11

[40] Coraux J, N'Diaye A T, Busse C and Michely T 2008 Structural coherency of graphene on Ir(111) *Nano Lett.* **8** 565–70

[41] Sutter P, Sadowski J T and Sutter E 2009 Graphene on Pt(111): Growth and substrate interaction *Phys. Rev. B - Condens. Matter Mater. Phys.* **80** 1–10

[42] Ishihara M, Koga Y, Kim J, Tsugawa K and Hasegawa M 2011 Direct evidence of advantage of Cu(111) for graphene synthesis by using Raman mapping and electron backscatter diffraction *Mater. Lett.* **65** 2864–7

[43] Mattevi C, Kim H and Chhowalla M 2011 A review of chemical vapour deposition of graphene on copper *J. Mater. Chem.* **21** 3324–34

[44] Zhang J, Lin L, Jia K, Sun L, Peng H and Liu Z 2020 Controlled Growth of Single-Crystal Graphene Films *Adv. Mater.* **32** 1–27

[45] Liu N, Fu L, Dai B, Yan K, Liu X, Zhao R, Zhang Y and Liu Z 2011 Universal segregation growth approach to wafer-size graphene from non-noble metals *Nano Lett.* **11**

297–303

[46] Addou R, Dahal A, Sutter P and Batzill M 2012 Monolayer graphene growth on Ni(111) by low temperature chemical vapor deposition *Appl. Phys. Lett.* **100** 98–101

[47] Losurdo M, Giangregorio M M, Capezzuto P and Bruno G 2011 Graphene CVD growth on copper and nickel: Role of hydrogen in kinetics and structure *Phys. Chem. Chem. Phys.* **13** 20836–43

[48] Yu Q, Jauregui L A, Wu W, Colby R, Tian J, Su Z, Cao H, Liu Z, Pandey D, Wei D, Chung T F, Peng P, Guisinger N P, Stach E A, Bao J, Pei S S and Chen Y P 2011 Control and characterization of individual grains and grain boundaries in graphene grown by chemical vapour deposition *Nat. Mater.* **10** 443–9

[49] Yuan Q, Song G, Sun D and Ding F 2014 Formation of graphene grain boundaries on Cu(100) surface and a route towards their elimination in chemical vapor deposition growth *Sci. Rep.* **4** 1–5

[50] Zhang J, Zhao J and Lu J 2012 Intrinsic strength and failure behaviors of graphene grain boundaries *ACS Nano* **6** 2704–11

[51] Serov A Y, Ong Z Y and Pop E 2013 Effect of grain boundaries on thermal transport in graphene *Appl. Phys. Lett.* **102**

[52] Zhang H, Lee G, Gong C, Colombo L and Cho K 2014 Grain boundary effect on electrical transport properties of graphene *J. Phys. Chem. C* **118** 2338–43

[53] Gao L, Guest J R and Guisinger N P 2010 Epitaxial graphene on Cu(111) *Nano Lett.* **10** 3512–6

[54] Yan Z, Peng Z and Tour J M 2014 Chemical vapor deposition of graphene single crystals *Acc. Chem. Res.* **47** 1327–37

[55] Geng D, Wang H and Yu G 2015 Graphene single crystals: Size and morphology engineering *Adv. Mater.* **27** 2821–37

[56] Miseikis V, Convertino D, Mishra N, Gemmi M, Mashoff T, Heun S, Haghighian N, Bisio F, Canepa M, Piazza V and Coletti C 2015 Rapid CVD growth of millimetre-sized

single crystal graphene using a cold-wall reactor *2D Mater.* **2** 014006

[57] Murdock A T, van Engers C D, Britton J, Babenko V, Meysami S S, Bishop H, Crossley A, Koos A A and Grobert N 2017 Targeted removal of copper foil surface impurities for improved synthesis of CVD graphene *Carbon N. Y.* **122** 207–16

[58] Chavez K L and Hess D W 2001 A Novel Method of Etching Copper Oxide Using Acetic Acid *J. Electrochem. Soc.* **148** G640

[59] Levendorf M P, Ruiz-vargas C S, Garg S and Park J 2009 Transfer-Free Batch Fabrication of Single Layer Graphene Transistors 1–5

[60] Miseikis V, Bianco F, David J, Gemmi M, Pellegrini V, Romagnoli M and Coletti C 2017 Deterministic patterned growth of high-mobility large-crystal graphene: A path towards wafer scale integration *2D Mater.* **4** 021004

[61] Banszerus L, Schmitz M, Engels S, Dauber J, Oellers M, Haupt F, Watanabe K, Taniguchi T, Beschoten B and Stampfer C 2015 Ultrahigh-mobility graphene devices from chemical vapor deposition on reusable copper *Sci. Adv.* **1** 1–7

[62] Lee G H, Cooper R C, An S J, Lee S, Van Der Zande A, Petrone N, Hammerberg A G, Lee C, Crawford B, Oliver W, Kysar J W and Hone J 2013 High-strength chemical-vapor-deposited graphene and grain boundaries *Science (80-.).* **340** 1074–6

[63] Cha S, Cha M, Lee S, Kang J H and Kim C 2015 Low-temperature, dry transfer-printing of a patterned graphene monolayer *Sci. Rep.* **5** 1–10

[64] Zhang G, Güell A G, Kirkman P M, Lazenby R A, Miller T S and Unwin P R 2016 Versatile Polymer-Free Graphene Transfer Method and Applications *ACS Appl. Mater. Interfaces* **8** 8008–16

[65] Park H, Lim C, Lee C and Kang J 2018 Optimized poly (methyl methacrylate) - mediated graphene-transfer process for fabrication of high-quality graphene layer *Nanotechnology* **29** 415303

[66] Cai C, Jia F, Li A, Huang F, Xu Z, Qiu L, Chen Y, Fei G and Wang M 2016 Crackless transfer of large-area graphene films for superior-performance transparent electrodes

Carbon N. Y. **98** 457–62

[67] de Castro R K, Araujo J R, Valaski R, Costa L O O, Archanjo B S, Fragneaud B, Cremona M and Achete C A 2015 New transfer method of CVD-grown graphene using a flexible, transparent and conductive polyaniline-rubber thin film for organic electronic applications *Chem. Eng. J.* **273** 509–18

[68] Chen M, Stekovic D, Li W, Arkook B, Haddon R C and Bekyarova E 2017 Sublimation-assisted graphene transfer technique based on small polyaromatic hydrocarbons *Nanotechnology* **28**

[69] Goniszewski S, Gallop J, Adabi M, Gajewski K, Shaforost O, Klein N, Sierakowski A, Chen J, Chen Y, Gotszalk T and Hao L 2015 Self-supporting graphene films and their applications *IET Circuits, Devices Syst.* **9** 420–7

[70] Kim J W, Woo J Y, Jo S, Oh J H, Hong W, Lee B C, Jung H J, Kim J H, Roh S C and Han C S 2020 Clean and less defective transfer of monolayer graphene by floatation in hot water *Appl. Surf. Sci.* **508** 145057

[71] Shivayogimath A, Whelan P R, MacKenzie D M A, Luo B, Huang D, Luo D, Wang M, Gammelgaard L, Shi H, Ruoff R S, Bøggild P and Booth T J 2019 Do-It-Yourself Transfer of Large-Area Graphene Using an Office Laminator and Water *Chem. Mater.* **31** 2328–36

[72] Pezzini S, Mišeikis V, Pace S, Rossella F, Watanabe K, Taniguchi T and Coletti C 2020 High-quality electrical transport using scalable CVD graphene *2D Mater.* **7**

[73] Wang Y, Zheng Y, Xu X, Dubuisson E, Bao Q, Lu J and Loh K P 2011 Electrochemical delamination of CVD-grown graphene film: Toward the recyclable use of copper catalyst *ACS Nano* **5** 9927–33

[74] Geim A K 2009 Graphene : Status and Prospects **324** 1530–5

[75] Novoselov K S, Fal'Ko V I, Colombo L, Gellert P R, Schwab M G and Kim K 2012 A roadmap for graphene *Nature* **490** 192–200

[76] Tiwari S K, Sahoo S, Wang N and Huczko A 2020 Graphene research and their outputs:

Status and prospect *J. Sci. Adv. Mater. Devices* **5** 10–29

[77] Kong W, Kum H, Bae S H, Shim J, Kim H, Kong L, Meng Y, Wang K, Kim C and Kim J 2019 Path towards graphene commercialization from lab to market *Nat. Nanotechnol.* **14** 927–38

[78] Romagnoli M, Sorianello V, Midrio M, Koppens F H L, Huyghebaert C, Neumaier D, Galli P, Templ W, D'Errico A and Ferrari A C 2018 Graphene-based integrated photonics for next-generation datacom and telecom *Nat. Rev. Mater.* **3** 392–414

[79] Nguyen B H and Nguyen V H 2016 Advances in graphene-based optoelectronics, plasmonics and photonics *Adv. Nat. Sci. Nanosci. Nanotechnol.* **7**

[80] Kojima E, Kano K, Wado H, Iwamori N and Corp D 2017 Magnetic Field Sensor of Graphene for Automotive Applications 1633

[81] Zhang D, Xu Z, Huang Z, Gutierrez A R, Chun I Y, Blocker C J, Cheng G, Liu Z, Fessler J A, Zhong Z and Norris T B 2019 Graphene-Based Transparent Photodetector Array for Multiplane Imaging *2019 Conf. Lasers Electro-Optics, CLEO 2019 - Proc.* **1** 4–5

[82] Anon 2023 https://graphene-flagship.eu/materials/news/graphene-flagship-s-innovations-in-automotive-technology-accelerate-green-mobility *Accessed Oct.*

[83] Anon 2023 https://graphene-flagship.eu/about/first-10-years/spearheads/c3-sh09-greenbat/ *Accessed Oct.*

[84] Seo J G, Lee C K, Lee D and Song S H 2018 High-performance tires based on graphene coated with Zn-free coupling agents *J. Ind. Eng. Chem.* **66** 78–85

[85] Ansarifar A, Wang L, Ellis R J, Kirtley S P and Riyazuddin N 2007 Enhancing the Mechanical Properties of Styrene– Butadiene Rubber by Optimizing the Chemical Bonding Between Silanized Silica Nanofiller and the Rubber *J. Appl. Polym. Sci.* **105** 322–32

[86] Anon 2023 https://velo.outsideonline.com/road/road-racing/graphene-2-0-vittoria-updates-compound-reinforcer/ *Accessed Oct.*

[87] Li X, Cai W, Colombo L and Ruoff R S 2009 Evolution of graphene growth on Ni and

Cu by carbon isotope labeling *Nano Lett.* **9** 4268–72

[88] Yu Q, Lian J, Siriponglert S, Li H, Chen Y P and Pei S S 2008 Graphene segregated on Ni surfaces and transferred to insulators *Appl. Phys. Lett.* **93** 1–4

[89] Gao L, Ren W, Xu H, Jin L, Wang Z, Ma T, Ma L P, Zhang Z, Fu Q, Peng L M, Bao X and Cheng H M 2012 Repeated growth and bubbling transfer of graphene with millimetre-size single-crystal grains using platinum *Nat. Commun.* **3** 699

[90] Luo Z, Lu Y, Singer D W, Berck M E, Somers L A, Goldsmith B R and Johnson A T C 2011 Effect of substrate roughness and feedstock concentration on growth of wafer-scale graphene at atmospheric pressure *Chem. Mater.* **23** 1441–7

[91] Chen S, Ji H, Chou H, Li Q, Li H, Suk J W, Piner R, Liao L, Cai W and Ruoff R S 2013 Millimeter-size single-crystal graphene by suppressing evaporative loss of Cu during low pressure chemical vapor deposition *Adv. Mater.* **25** 2062–5

[92] Miseikis V, Convertino D, Mishra N, Gemmi M, Mashoff T, Heun S, Haghighian N, Bisio F, Canepa M, Piazza V and Coletti C 2015 Rapid CVD growth of millimetre-sized single crystal graphene using a cold-wall reactor *2D Mater.* **2**

[93] Coletti C, Giambra M A, Miseikis V and Romagnoli M Graphene and Two-Dimensional Materials Transfer Method By Using Free-Standing Bilayer Polymeric Membrane 2020, EP3135631A1

[94] Giambra M A, Mišeikis V, Pezzini S, Marconi S, Montanaro A, Fabbri F, Sorianello V, Ferrari A C, Coletti C and Romagnoli M 2021 Wafer-scale integration of graphene-based photonic devices *ACS Nano* **15**, **2** 3171–87

[95] Ferrari A C and Basko D M 2013 Raman spectroscopy as a versatile tool for studying the properties of graphene *Nat. Nanotechnol.* **8**

[96] Calizo I, Bejenari I, Rahman M, Liu G and Balandin A A 2009 Ultraviolet Raman microscopy of single and multilayer graphene *J. Appl. Phys.* **106**

[97] Lan Y, Zondode M, Deng H, Yan J A, Ndaw M, Lisfi A, Wang C and Pan Y Le 2018 Basic concepts and recent advances of crystallographic orientation determination of

graphene by raman spectroscopy *Crystals* **8**

[98] Pimenta M A, Dresselhaus G, Dresselhaus M S, Cançado L G, Jorio A and Saito R 2007 Studying disorder in graphite-based systems by Raman spectroscopy *Phys. Chem. Chem. Phys.* **9** 1276–91

[99] Ferrari A C, Meyer J C, Scardaci V, Casiraghi C, Lazzeri M, Mauri F, Piscanec S, Jiang D, Novoselov K S, Roth S and Geim A K 2006 Raman spectrum of graphene and graphene layers *Phys. Rev. Lett.* **97** 187401

[100] Das A, Pisana S, Chakraborty B, Piscanec S, Saha S K, Waghmare U V., Novoselov K S, Krishnamurthy H R, Geim A K, Ferrari A C and Sood A K 2008 Monitoring dopants by Raman scattering in an electrochemically top-gated graphene transistor *Nat. Nanotechnol.* **3** 210–5

[101] Lee J E, Ahn G, Shim J, Lee Y S and Ryu S 2012 Optical separation of mechanical strain from charge doping in graphene *Nat. Commun.* **3**

[102] Basko D M, Piscanec S and Ferrari A C 2009 Electron-electron interactions and doping dependence of the two-phonon Raman intensity in graphene *Phys. Rev. B* **80** 165413

[103] Mohiuddin T M G, Lombardo A, Nair R R, Bonetti A, Savini G, Jalil R, Bonini N, Basko D M, Galiotis C, Marzari N, Novoselov K S, Geim A K and Ferrari A C 2009 Uniaxial strain in graphene by Raman spectroscopy: G peak splitting, Grüneisen parameters, and sample orientation *Phys. Rev. B - Condens. Matter Mater. Phys.* **79** 1–8

[104] Zabel J, Nair R R, Ott A, Georgiou T, Geim A K, Novoselov K S and Casiraghi C 2012 Raman spectroscopy of graphene and bilayer under biaxial strain: Bubbles and balloons *Nano Lett.* **12** 617–21

[105] Das A, Chakraborty B and Sood A K 2008 Raman spectroscopy of graphene on different substrates and influence of defects *Bull. Mater. Sci.* **31** 579–84

[106] Hao Y, Wang Y, Wang L, Ni Z, Wang Z, Wang R, Koo C K, Shen Z and Thong J T L 2010 Probing layer number and stacking order of few-layer graphene by Raman Spectroscopy *Small* **6** 195–200

[107] Couto N J G, Costanzo D, Engels S, Ki D K, Watanabe K, Taniguchi T, Stampfer C, Guinea F and Morpurgo A F 2014 Random strain fluctuations as dominant disorder source for high-quality on-substrate graphene devices *Phys. Rev. X* **4** 041019

[108] U. Maver, T. Maver, Z. Peršin, M. Mozetič, A. Vesel M G and K S-K 2013 Polymer Characterization with the Atomic Force Microscope *Polym. Sci.* 51060

[109] Stevie F A and Donley C L 2020 Introduction to x-ray photoelectron spectroscopy *J. Vac. Sci. Technol. A* **38** 063204

[110] Hsiao H H, Chu C H and Tsai D P 2017 Fundamentals and Applications of Metasurfaces *Small Methods* **1** 1–20

[111] Martín-Palma R J and Lakhtakia A 2013 *Vapor-Deposition Techniques* (Elsevier Inc.)

[112] Tyagi A, Mišeikis V, Martini L, Forti S, Mishra N, Gebeyehu Z M, Giambra M A, Zribi J, Frégnaux M, Aureau D, Romagnoli M, Beltram F and Coletti C 2022 Ultra-clean high-mobility graphene on technologically relevant substrates *Nanoscale* **14** 2167–76

[113] Randviir E P, Brownson D A C and Banks C E 2014 A decade of graphene research: Production, applications and outlook *Mater. Today* **17** 426–32

[114] Sang M, Shin J, Kim K and Yu K J 2019 Electronic and thermal properties of graphene and recent advances in graphene based electronics applications *Nanomaterials* **9** 1–33

[115] Mackenzie D M A, Smistrup K, Whelan P R, Luo B, Shivayogimath A, Nielsen T, Petersen D H, Messina S A and Bøggild P 2017 Batch fabrication of nanopatterned graphene devices via nanoimprint lithography *Appl. Phys. Lett.* **111** 193103

[116] Kim Y, Kim T, Lee J, Choi Y S, Moon J, Park S Y, Lee T H, Park H K, Lee S A, Kwon M S, Byun H G, Lee J H, Lee M G, Hong B H and Jang H W 2021 Tailored Graphene Micropatterns by Wafer-Scale Direct Transfer for Flexible Chemical Sensor Platform *Adv. Mater.* **33** 2004827

[117] Chen X, Wu B and Liu Y 2016 Direct preparation of high quality graphene on dielectric substrates *Chem. Soc. Rev.* **45** 2057–74

[118] Mišeikis V and Coletti C 2021 Wafer-scale integration of graphene for waveguide-

integrated optoelectronics *Appl. Phys. Lett.* **119**

[119] Chen B, Huang L, Ma X, Dong L, Zhang Z and Peng L M 2015 Exploration of sensitivity limit for graphene magnetic sensors *Carbon N. Y.* **94** 585–9

[120] Chen J H, Jang C, Xiao S, Ishigami M and Fuhrer M S 2008 Intrinsic and extrinsic performance limits of graphene devices on SiO 2 *Nat. Nanotechnol.* **3** 206–9

[121] Chen J H, Jang C, Adam S, Fuhrer M S, Williams E D and Ishigami M 2008 Charged-impurity scattering in graphene *Nat. Phys.* **4** 377–81

[122] Suk J W, Lee W H, Lee J, Chou H, Piner R D, Hao Y, Akinwande D and Ruoff R S 2013 Enhancement of the electrical properties of graphene grown by chemical vapor deposition via controlling the effects of polymer residue *Nano Lett.* **13** 1462–7

[123] Son B H, Kim H S, Jeong H, Park J Y, Lee S and Ahn Y H 2017 Electron beam induced removal of PMMA layer used for graphene transfer *Sci. Rep.* **7** 18058

[124] Lin Y C, Lu C C, Yeh C H, Jin C, Suenaga K and Chiu P W 2012 Graphene annealing: How clean can it be? *Nano Lett.* **12** 414–9

[125] Pirkle A, Chan J, Venugopal A, Hinojos D, Magnuson C W, McDonnell S, Colombo L, Vogel E M, Ruoff R S and Wallace R M 2011 The effect of chemical residues on the physical and electrical properties of chemical vapor deposited graphene transferred to SiO2 *Appl. Phys. Lett.* **99** 122108

[126] Choi W, Shehzad M A, Park S and Seo Y 2017 Influence of removing PMMA residues on surface of CVD graphene using a contact-mode atomic force microscope *RSC Adv.* **7** 6943–9

[127] Goossens A M, Calado V E, Barreiro A, Watanabe K, Taniguchi T and Vandersypen L M K 2012 Mechanical cleaning of graphene *Appl. Phys. Lett.* **100** 073110

[128] Moser J, Barreiro A and Bachtold A 2007 Current-induced cleaning of graphene *Appl. Phys. Lett.* **91** 163513

[129] Cheng Z, Zhou Q, Wang C, Li Q, Wang C and Fang Y 2011 Toward intrinsic graphene surfaces: A systematic study on thermal annealing and wet-chemical treatment of SiO2-

supported graphene devices *Nano Lett.* **11** 767–71

[130] Kumar K, Kim Y S and Yang E H 2013 The influence of thermal annealing to remove polymeric residue on the electronic doping and morphological characteristics of graphene *Carbon N. Y.* **65** 35–45

[131] Her M, Beams R and Novotny L 2013 Graphene transfer with reduced residue *Phys. Lett. Sect. A Gen. At. Solid State Phys.* **377** 1455–8

[132] Ni Z H, Wang H M, Luo Z Q, Wang Y Y, Yu T, Wu Y H and Shen Z X 2010 The effect of vacuum annealing on graphene *J. Raman Spectrosc.* **41** 479–83

[133] Romagnoli M, Sorianello V, Midrio M, Koppens F H L, Huyghebaert C, Neumaier D, Galli P, Templ W, D'Errico A and Ferrari A C 2018 Graphene-based integrated photonics for next-generation datacom and telecom *Nat. Rev. Mater.* **3** 392–414

[134] Cunge G, Ferrah D, Petit-Etienne C, Davydova A, Okuno H, Kalita D, Bouchiat V and Renault O 2015 Dry efficient cleaning of poly-methyl-methacrylate residues from graphene with high-density H 2 and H 2 -N 2 plasmas *J. Appl. Phys.* **118** 123302

[135] Cançado L G, Jorio A, Ferreira E H M, Stavale F, Achete C A, Capaz R B, Moutinho M V O, Lombardo A, Kulmala T S and Ferrari A C 2011 Quantifying defects in graphene via Raman spectroscopy at different excitation energies *Nano Lett.* **11** 3190–6

[136] Yoon D, Son Y W and Cheong H 2011 Strain-dependent splitting of the double-resonance raman scattering band in graphene *Phys. Rev. Lett.* **106** 1–4

[137] Piscanec S, Lazzeri M, Mauri F, Ferrari A C and Robertson J 2004 Kohn anomalies and electron-phonon interactions in graphite *Phys. Rev. Lett.* **93** 1–4

[138] Neumann C, Reichardt S, Venezuela P, Drögeler M, Banszerus L, Schmitz M, Watanabe K, Taniguchi T, Mauri F, Beschoten B, Rotkin S V. and Stampfer C 2015 Raman spectroscopy as probe of nanometre-scale strain variations in graphene *Nat. Commun.* **6** 8429

[139] Chen B, Huang H, Ma X, Huang L, Zhang Z and Peng L M 2014 How good can CVD-grown monolayer graphene be? *Nanoscale* **6** 15255–61

[140] Sagade A A, Neumaier D, Schall D, Otto M, Pesquera A, Centeno A, Elorza A Z and Kurz H 2015 Highly air stable passivation of graphene based field effect devices *Nanoscale* **7** 3558–64

[141] Salimian S and Araghi M E A 2016 Effect of Residual Charge Carrier on the Performance of a Graphene Field Effect Transistor *Chinese Phys. Lett.* **33**

[142] Ryu S, Liu L, Berciaud S, Yu Y J, Liu H, Kim P, Flynn G W and Brus L E 2010 Atmospheric oxygen binding and hole doping in deformed graphene on a SiO2 substrate *Nano Lett.* **10** 4944–51

[143] Sojoudi H, Baltazar J, Henderson C and Graham S 2012 Impact of post-growth thermal annealing and environmental exposure on the unintentional doping of CVD graphene films *J. Vac. Sci. Technol. B, Nanotechnol. Microelectron. Mater. Process. Meas. Phenom.* **30** 041213

[144] Dankert A, Karpiak B and Dash S P 2017 Hall sensors batch-fabricated on all-CVD h-BN/graphene/h-BN heterostructures *Sci. Rep.* **7** 15231

[145] Bando M, Ohashi T, Dede M, Akram R, Oral A, Park S Y, Shibasaki I, Handa H and Sandhu A 2009 High sensitivity and multifunctional micro-Hall sensors fabricated using InAlSb/InAsSb/InAlSb heterostructures *J. Appl. Phys.* **105** 27E909

[146] Geim A K and Novoselov K S 2007 The rise of graphene PROGRESS *Nat. Mater.* **6** 183–91

[147] Das Sarma S, Adam S, Hwang E H and Rossi E 2011 Electronic transport in two-dimensional graphene *Rev. Mod. Phys.* **83** 407–70

[148] Dauber J, Sagade A A, Oellers M, Watanabe K, Taniguchi T, Neumaier D and Stampfer C 2015 Ultra-sensitive Hall sensors based on graphene encapsulated in hexagonal boron nitride *Appl. Phys. Lett.* **106** 193501

[149] Schaefer B T, Wang L, Jarjour A, Watanabe K, Taniguchi T, McEuen P L and Nowack K C 2020 Magnetic field detection limits for ultraclean graphene Hall sensors *Nat. Commun.* **11** 1–8

[150] Kretinin A V., Cao Y, Tu J S, Yu G L, Jalil R, Novoselov K S, Haigh S J, Gholinia A, Mishchenko A, Lozada M, Georgiou T, Woods C R, Withers F, Blake P, Eda G, Wirsig A, Hucho C, Watanabe K, Taniguchi T, Geim A K and Gorbachev R V. 2014 Electronic properties of graphene encapsulated with different two-dimensional atomic crystals *Nano Lett.* **14** 3270–6

[151] Yudistira D, Wu C, Brems S, Cott D, Milenin A, Vandersmissen K, Maestre Caro A, Centeno A, Zurutuza A, Van Campenhout J, Huyghebaert C, Asselberghs I, Van Thourhout D and Pantouvaki M 2023 Wafer-scale graphene electro-absorption modulators fabricated in a 300 mm CMOS platform 7

[152] Xu H, Zhang Z, Shi R, Liu H, Wang Z, Wang S and Peng L M 2013 Batch-fabricated high-performance graphene Hall elements *Sci. Rep.* **3**

[153] Collomb D, Li P and Bending S J 2019 Nanoscale graphene Hall sensors for high-resolution ambient magnetic imaging *Sci. Rep.* **9** 14424

[154] Joo M K, Kim J, Park J H, Nguyen V L, Kim K K, Lee Y H and Suh D 2016 Large-Scale Graphene on Hexagonal-BN Hall Elements: Prediction of Sensor Performance without Magnetic Field *ACS Nano* **10** 8803–11

[155] Tyagi A, Mišeikis V, Martini L, Forti S, Mishra N, Gebeyehu Z M, Giambra M A, Zribi J, Frégnaux M, Aureau D, Romagnoli M, Beltram F and Coletti C 2022 Ultra-clean high-mobility graphene on technologically relevant substrates *Nanoscale* **14** 2167–76

[156] Heremans J 1993 Solid state magnetic field sensors and applications *J. Phys. D. Appl. Phys.* **26** 1149–68

[157] Huang L, Zhang Z, Chen B, Ma X, Zhong H and Peng L M 2014 Ultra-sensitive graphene Hall elements *Appl. Phys. Lett.* **104**

[158] Kim Y, Herlinger P, Taniguchi T, Watanabe K and Smet J H 2019 Reliable Postprocessing Improvement of van der Waals Heterostructures *ACS Nano* **13** 14182–90

[159] Wang Z, Banszerus L, Otto M, Watanabe K, Taniguchi T, Stampfer C and Neumaier D 2016 Encapsulated graphene-based Hall sensors on foil with increased sensitivity *Phys. Status Solidi Basic Res.* **253** 2316–20

[160] Anon Antireflection Coating on Pmma; https://www.iof.fraunhofer.de/en/competences/coating-and-surface-functionalization/coating-on-plastic/antireflection-coating-pmma.html 3

[161] Koppens F H L, Mueller T, Avouris P, Ferrari A C, Vitiello M S and Polini M 2014 Photodetectors based on graphene, other two-dimensional materials and hybrid systems *Nat. Nanotechnol.* **9** 780–93

[162] Konstantatos G 2018 Current status and technological prospect of photodetectors based on two-dimensional materials *Nat. Commun.* **9** 5266

[163] Marconi S, Giambra M A, Montanaro A, Mišeikis V, Soresi S, Tirelli S, Galli P, Buchali F, Templ W, Coletti C, Sorianello V and Romagnoli M 2021 Photo thermal effect graphene detector featuring 105 Gbit s−1 NRZ and 120 Gbit s−1 PAM4 direct detection *Nat. Commun.* **12** 806

[164] An J, Wang B, Shu C, Wu W, Sun B, Zhang Z, Li D and Li S 2021 Research development of 2D materials based photodetectors towards mid-infrared regime *Nano Sel.* **2** 527–40

[165] Zhang B Y, Liu T, Meng B, Li X, Liang G, Hu X and Wang Q J 2013 Broadband high photoresponse from pure monolayer graphene photodetector *Nat. Commun.* **4** 1811

[166] Wang J, Han J, Chen X and Wang X 2019 Design strategies for two-dimensional material photodetectors to enhance device performance *InfoMat* **1** 33–53

[167] Wang F, Zhang Y, Tian C, Girit C, Zettl A, Crommie M and Shen Y R 2008 Gate-variable optical transitions in graphene *Science (80-.).* **320** 206–9

[168] Nair R R, Blake P, Grigorenko A N, Novoselov K S, Booth T J, Stauber T, Peres N M R and Geim A K 2008 Fine structure constant defines visual transparency of graphene *Science (80-.).* **320** 1308

[169] Ohl R S 1946 Light sensitive electric device *United states Pat. Off.* **2,402** 6621946

[170] Chapin D M, Fuller C S and Pearson G L 1954 A new silicon p-n junction photocell for converting solar radiation into electrical power *J. Appl. Phys.* **25** 676–7

[171] Monroy E, Omnès F and Calle F 2003 Wide-bandgap semiconductor ultraviolet photodetectors *Semicond. Sci. Technol.* **18** R33

[172] Rao G, Freitag M, Chiu H Y, Sundaram R S and Avouris P 2011 Raman and photocurrent imaging of electrical stress-induced p-n junctions in graphene *ACS Nano* **5**, **7** 5848–54

[173] Max C. Lemme, Frank H. L. Koppens, Abram L. Falk, Mark S. Rudner H P and Marcus L S L and C M 2011 Gate-Activated Photoresponse in a Graphene p-n Junction *Nano Lett.* **11** 4134–7

[174] Gréboval C, Dabard C, Konstantinov N, Cavallo M, Chee S S, Chu A, Dang T H, Khalili A, Izquierdo E, Prado Y, Majjad H, Xu X Z, Dayen J F and Lhuillier E 2021 Split-Gate Photodiode Based on Graphene/HgTe Heterostructures with a Few Nanosecond Photoresponse *ACS Appl. Electron. Mater.* **3** 4681–8

[175] Liu N, Tian H, Schwartz G, Tok J B H, Ren T L and Bao Z 2014 Large-area, transparent, and flexible infrared photodetector fabricated using P-N junctions formed by N-doping chemical vapor deposition grown graphene *Nano Lett.* **14** 3702–8

[176] Ding Y, Cheng Z, Zhu X, Yvind K, Dong J, Galili M, Hu H, Mortensen N A, Xiao S and Oxenløwe L K 2020 Ultra-compact integrated graphene plasmonic photodetector with bandwidth above 110 GHz *Nanophotonics* **9** 317–25

[177] Sundararaju U, Haniff M A S M, Ker P J and Menon P S 2021 Mos2/h-bn/graphene heterostructure and plasmonic effect for self-powering photodetector: A review *Materials (Basel).* **14** 1672

[178] Lin Y, Ma Q, Shen P C, Ilyas B, Bie Y, Liao A, Ergeçen E, Han B, Mao N, Zhang X, Ji X, Zhang Y, Yin J, Huang S, Dresselhaus M, Gedik N, Jarillo-Herrero P, Ling X, Kong J and Palacios T 2019 Asymmetric hot-carrier thermalization and broadband photoresponse in graphene-2D semiconductor lateral heterojunctions *Sci. Adv.* **5** eaav1493

[179] Sun Y L, Xie D, Sun M X, Teng C J, Qian L, Chen R S, Xiang L and Ren T L 2018 Hybrid graphene/cadmium-free ZnSe/ZnS quantum dots phototransistors for UV detection *Sci. Rep.* **8** 5107

[180] Ansell D, Radko I P, Han Z, Rodriguez F J, Bozhevolnyi S I and Grigorenko A N 2015

Hybrid graphene plasmonic waveguide modulators *Nat. Commun.* **6** 8846

[181] Mišeikis V, Marconi S, Giambra M A, Montanaro A, Martini L, Fabbri F, Pezzini S, Piccinini G, Forti S, Terrés B, Goykhman I, Hamidouche L, Legagneux P, Sorianello V, Ferrari A C, Koppens F H L, Romagnoli M and Coletti C 2020 Ultrafast, Zero-Bias, Graphene Photodetectors with Polymeric Gate Dielectric on Passive Photonic Waveguides *ACS Nano* **14** 11190–204

[182] Cakmakyapan S, Lu P K, Navabi A and Jarrahi M 2018 Gold-patched graphene nano-stripes for high-responsivity and ultrafast photodetection from the visible to infrared regime *Light Sci. Appl.* **7** 20

[183] Wang D and Madden S 2021 Designing absorbers for graphene based mid-infrared wide band waveguide photodetectors *Opt. Express* **29** 33850–63

[184] Teweldebrhan D and Balandin A A 2009 Modification of graphene properties due to electron-beam irradiation *Appl. Phys. Lett.* **94** 013101

[185] Childres I, Jauregui L A, Foxe M, Tian J, Jalilian R, Jovanovic I and Chen Y P 2010 Effect of electron-beam irradiation on graphene field effect devices *Appl. Phys. Lett.* **97** 173109

[186] Zhou Y, Jadwiszczak J, Keane D, Chen Y, Yu D and Zhang H 2017 Programmable graphene doping via electron beam irradiation *Nanoscale* **9** 8657–64

[187] Yu X, Shen Y, Liu T, Wu T and Jie Wang Q 2015 Photocurrent generation in lateral graphene p-n junction created by electron-beam irradiation *Sci. Rep.* **5** 12014

[188] Shi W, Kahn S, Jiang L, Wang S Y, Tsai H Z, Wong D, Taniguchi T, Watanabe K, Wang F, Crommie M F and Zettl A 2020 Reversible writing of high-mobility and high-carrier-density doping patterns in two-dimensional van der Waals heterostructures *Nat. Electron.* **3** 99–105

[189] Wang K L and Evwaraye A O 1976 Determination of interface and bulk-trap states of IGFET's using deep-level transient spectroscopy *J. Appl. Phys.* **47** 4574

[190] Pisana S, Lazzeri M, Casiraghi C, Novoselov K S, Geim A K, Ferrari A C and Mauri F

2007 Breakdown of the adiabatic Born-Oppenheimer approximation in graphene *Nat. Mater.* **6** 198–201

[191] Restrepo O D, Krymowski K E, Goldberger J and Windl W 2014 A first principles method to simulate electron mobilities in 2D materials *New J. Phys.* **16** 105009

[192] Jiang J, Zhang Y, Wang A, Duan J, Ji H, Pang J, Sang Y, Feng X, Liu H and Han L 2020 Construction of High Field-Effect Mobility Multilayer MoS2Field-Effect Transistors with Excellent Stability through Interface Engineering *ACS Appl. Electron. Mater.* **2**, **7** 2132–40

[193] Lee E J H, Balasubramanian K, Weitz R T, Burghard M and Kern K 2008 Contact and edge effects in graphene devices *Nat. Nanotechnol.* **3** 486–90

[194] Meng J, Wu H C, Chen J J, Lin F, Bie Y Q, Shvets I V., Yu D P and Liao Z M 2013 Ultraviolet irradiation-controlled memory effect in graphene field-effect transistors *Small* **9** 2240–4

[195] Park J, Ahn Y H and Ruiz-Vargas C 2009 Imaging of photocurrent generation and collection in single-layer graphene *Nano Lett.* **9**, **5** 1742–6

[196] Li H, Su S, Liang C, Zhang T, An X, Huang M, Tao H, Ma X, Ni Z, Tian H and Chen X 2019 UV Rewritable Hybrid Graphene/Phosphor p-n Junction Photodiode *ACS Appl. Mater. Interfaces* **11**, **46** 43351–8

[197] Wang G, Zhang M, Chen D, Guo Q, Feng X, Niu T, Liu X, Li A, Lai J, Sun D, Liao Z, Wang Y, Chu P K, Ding G, Xie X, Di Z and Wang X 2018 Seamless lateral graphene p–n junctions formed by selective in situ doping for high-performance photodetectors *Nat. Commun.* **9** 5168

[198] Meng J, Song H D, Li C Z, Jin Y, Tang L, Liu D, Liao Z M, Xiu F and Yu D P 2015 Lateral graphene p-n junctions formed by the graphene/MoS2 hybrid interface *Nanoscale* **7** 11611–9

[199] Wang D, Allcca A E L, Chung T F, Kildishev A V., Chen Y P, Boltasseva A and Shalaev V M 2020 Enhancing the graphene photocurrent using surface plasmons and a p-n junction *Light Sci. Appl.* **9** 126

[200] Kang C G, Lee S K, Choe S, Lee Y G, Lee C-L and Lee B H 2013 Intrinsic photocurrent characteristics of graphene photodetectors passivated with Al_2O_3 *Opt. Express* **21** 23391–400

[201] He H, Kim K H, Danilov A, Montemurro D, Yu L, Park Y W, Lombardi F, Bauch T, Moth-Poulsen K, Iakimov T, Yakimova R, Malmberg P, Müller C, Kubatkin S and Lara-Avila S 2018 Uniform doping of graphene close to the Dirac point by polymer-assisted assembly of molecular dopants *Nat. Commun.* **9** 3596

[202] Sundararajan A, Boland M J, Patrick Hunley D and Strachan D R 2013 Doping and hysteretic switching of polymer-encapsulated graphene field effect devices *Appl. Phys. Lett.* **103** 253505

[203] Leblanc J L 2002 Rubber-filler interactions and rheological properties in filled compounds *Prog. Polym. Sci.* **27** 627–87

[204] Li Y, Han B, Liu L, Zhang F, Zhang L, Wen S, Lu Y, Yang H and Shen J 2013 Surface modification of silica by two-step method and properties of solution styrene butadiene rubber (SSBR) nanocomposites filled with modified silica *Compos. Sci. Technol.* **88** 69–75

[205] Kim K, Lee J Y, Choi B J, Seo B, Kwag G H, Paik H J and Kim W 2014 Styrene-butadiene-glycidyl methacrylate terpolymer/silica composites: Dispersion of silica particles and dynamic mechanical properties *Compos. Interfaces* **21** 685–702

[206] Zacharia R, Ulbricht H and Hertel T 2004 Interlayer cohesive energy of graphite from thermal desorption of polyaromatic hydrocarbons *Phys. Rev. B - Condens. Matter Mater. Phys.* **69** 1–7

[207] Huang J, Tang Z, Yang Z and Guo B Bioinspired Interface Engineering in Elastomer / Graphene Composites by Constructing Sacrifi cial Metal – Ligand Bonds 1040–5

[208] Barbera V, Bernardi A, Palazzolo A, Rosengart A, Brambilla L and Galimberti M 2018 Facile and sustainable functionalization of graphene layers with pyrrole compounds *Pure Appl. Chem.* **90** 253–70

[209] Yao Y, Li Z, Lin Z, Moon K S, Agar J and Wong C 2011 Controlled growth of

multilayer, few-layer, and single-layer graphene on metal substrates *J. Phys. Chem. C* **115** 5232–8

[210] Cornell S W and Koenig J L 1969 The Raman Spectra of Polybutadiene Rubbers *Macromolecules* **2** 540–5

[211] Bong J H, Sul O, Yoon A, Choi S Y and Cho B J 2014 Facile graphene n-doping by wet chemical treatment for electronic applications *Nanoscale* **6** 8503–8

[212] Yan X, Kitahama Y, Sato H, Suzuki T, Han X, Itoh T, Bokobza L and Ozaki Y 2012 Laser heating effect on Raman spectra of styrene-butadiene rubber/multiwalled carbon nanotube nanocomposites *Chem. Phys. Lett.* **523** 87–91

[213] Saltzgaber G, Wojcik P, Sharf T, Leyden M R, Wardini J L, Heist C A, Adenuga A A, Remcho V T and Minot E D 2013 Scalable graphene field-effect sensors for specific protein detection *Nanotechnology* **24**

[214] Lupina G, Kitzmann J, Costina I, Lukosius M, Wenger C, Wolff A, Vaziri S, Östling M, Pasternak I, Krajewska A, Strupinski W, Kataria S, Gahoi A, Lemme M C, Ruhl G, Zoth G, Luxenhofer O and Mehr W 2015 Residual metallic contamination of transferred chemical vapor deposited graphene *ACS Nano* **9** 4776–85

[215] Zhang X X, He W, Chen S W, Lyu J Y, Guo Z, Gozin M and Yan Q L 2019 Tuning the crystal morphology and catalytic behavior of graphene-templated energetic bis-tetrazole copper coordination polymers *Adv. Compos. Hybrid Mater.* **2** 289–300

[216] Lin Y C, Lu C C, Yeh C H, Jin C, Suenaga K and Chiu P W 2012 Graphene annealing: How clean can it be? *Nano Lett.* **12** 414–9

[217] Kulkarni P A, Satpati A K, Thandavarayan M and Shendage S S 2021 An efficient Cu/functionalized graphene oxide catalyst for synthesis of 5-substituted 1H-tetrazoles *Chem. Pap.* **75** 2891–9

[218] Torrisi F, Hasan T, Wu W, Sun Z, Lombardo A, Kulmala T S, Hsieh G, Jung S, Bonaccorso F, Paul P J, Chu D and Ferrari A C 2012 Inkjet-Printed Graphene Electronics 2992–3006

[219] Bracamonte M V., Lacconi G I, Urreta S E and Foa Torres L E F 2014 On the nature of defects in liquid-phase exfoliated graphene *J. Phys. Chem. C* **118** 15455–9

[220] Kim N H, Kuila T and Lee J H 2013 Simultaneous reduction, functionalization and stitching of graphene oxide with ethylenediamine for composites application *J. Mater. Chem. A* **1** 1349–58